Visual Stimulus Tuning in Mouse Primary Visual Cortex in Freely Moving Immersive Virtual Reality

Matthew Kennedy McCann

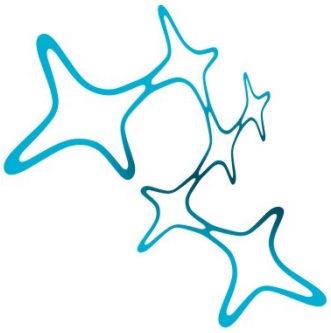

Graduate School of
Systemic Neurosciences

LMU Munich

Dissertation der
Graduate School of Systemic Neurosciences der
Ludwig-Maximilians-Universität München

19 July 2024

Supervisor
Prof. Dr. Mark Hübener
Max Planck Institute for Biological Intelligence (MPI-BI)

First Reviewer: Prof. Dr. Mark Hübener
Second Reviewer: Prof. Dr. Laura Busse
External Reviewer: Dr. Guy Bouvier

Date of Submission: 19 July 2024
Date of Defense: 5 December 2024

Table of Contents

List of Figures iv
List of Equations v
List of Abbreviations vi
Abstract ix
1 Introduction 1
1.1 Organization of the Mouse Early Visual System 3
1.1.1 The Retina 4
1.1.2 The Superior Colliculus 5
1.1.3 The Dorsal Lateral Geniculate Nucleus 5
1.1.4 The Primary Visual Cortex 6
1.2 Visual and Nonvisual Stimulus Coding in V1 7
1.2.1 Visual Stimulus Coding 8
1.2.2 Nonvisual Stimulus Coding 11
1.3 Optical Interrogation of Neural Activity *in vivo* During Free Behavior 15
1.3.1 General Principles of Calcium Imaging *in vivo* 15
1.3.2 Miniaturized *in vivo* Microscopy (Miniscopes) 18
1.4 Visual Stimulation During Free Behavior 19
1.4.1 Visual Stimulation in Head Restrained Animals 19
1.4.2 Virtual Reality Environments in Neuroscience 20
1.5 Study Aims 23
2 Materials and Methods 24
2.1 List of Materials 24
2.1.1 Plasmids 24
2.1.2 Viruses 24
2.1.3 Antibodies and Staining Solutions 24
2.1.4 Chemicals and Pharmaceuticals 24
2.1.5 Equipment, Instrumentation, and Hardware 25
2.1.6 Software 26
2.2 Methods 27
2.2.1 Ethics 27
2.2.2 Animals and Animal Housing 27
2.2.3 Freely Moving Virtual Reality (VR) System 27
2.2.4 Molecular Cloning, Virus Preparation, and Viral Strategy 32
2.2.5 *In-Vivo* Transduction of GECIs and GRIN Lens Implantation 33
2.2.6 Miniscope Baseplate Implantation 36

2.2.7 Animal Habituation 36
2.2.8 Miniscope Imaging 37
2.2.9 Perfusions and Immunohistochemistry 38
2.2.10 Data Analysis 39
3 Results 47
3.1 Establishment of a Freely Moving VR Visual Stimulation Paradigm 47
3.2 Responses to Visual Stimuli and Running Onset 51
3.3 Visual Responsivity, Orientation and Direction Tuning 54
3.3.1 Visual Responsivity is Similar Between Head Fixed and Freely Moving Sessions 54
3.3.2 V1 Neurons Exhibit Orientation and Direction Selectivity in Freely Moving VR 58
3.4 Comparison of Visual Tuning Curves and Properties Between Consecutive Sessions 59
3.4.1 Visual Tuning Properties are Consistent Between Repeated Head Fixed Sessions 60
3.4.2 Visual Tuning Properties are Variable Between Repeated Freely Moving Sessions 62
3.4.3 PO is Consistent, While OSI, DSI, and PD are Variable Between Consecutive Head Fixed and Freely Moving Sessions 64
3.5 Self-Motion Tuning in V1 Neurons 68
3.5.1 Self-Motion Tuning is Mostly Consistent During Experiments without Visual Stimuli 70
3.6 Multimodal Representation of Visual and Self-Motion Stimulus Information 72
3.6.1 Visual Stimulus Variables 72
3.6.2 Self-Motion Variables 73
3.6.3 Multimodal Representations in Re-Identified Cells 74
4 Discussion 76
4.1 Calcium Imaging of V1 Neurons During Visual Stimulation in Freely Moving VR 76
4.1.1 Technical Considerations, Limitations, and Suggested Improvements 78
4.2 Visual Tuning Properties are Measurable in Both Head Fixed and Freely Moving Configurations 80
4.3 Visual Tuning Properties are Less Consistent Between Consecutive Head Fixed and Freely Moving Sessions than in Repeated Head Fixed Sessions 82
4.4 Self-Motion and Postural Variables are Represented Across the V1 Population 84
4.5 Multimodal Representation of Visual Stimulus Features and Self-Motion in V1 87
4.6 Conclusions and Future Directions 89

References **91**
Appendix A: Supplementary Figures **105**
Appendix B: Statistics **110**
List of Publications **115**

List of Figures

Figure 1.1 Organization of the imaging forming pathway of the early rodent visual system 4

Figure 1.2 Visual receptive fields in the early visual system 8

Figure 1.3 Nonvisual projections to V1 and overlap in areas representing vision, navigation, and motion 11

Figure 1.4 Example systems for delivering visual stimulation to head fixed and freely behaving animals 21

Figure 3.1 Immersive VR system and wire free miniscope imaging in freely moving VR 48

Figure 3.2 Example head fixed experiment ethogram and FOV 49

Figure 3.3 Example freely moving experiment ethogram and FOV 50

Figure 3.4 Neurons display visually evoked responses to drifting grating Gabor stimuli in VR 52

Figure 3.5 V1 neurons do not exhibit responses consistently locked to locomotion onset 53

Figure 3.6 Example orientation and direction tuning curves during a head fixed experiment 55

Figure 3.7 Example orientation and direction tuning curves during a freely moving experiment 56

Figure 3.8 Orientation and direction tuned neurons are more prevalent in head fixed configurations 57

Figure 3.9 Example re-identified cells from repeated head fixed imaging sessions. ... 61

Figure 3.10 Example re-identified cells from repeated freely moving imaging sessions 63

Figure 3.11 Tuning curves from hand-selected example re-identified neurons between head fixation and free behavior 65

Figure 3.12 Orientation and direction selectivity indices are consistent in repeated head fixed sessions, but not in experiments with free behavior 66

Figure 3.13 Preferred orientation and direction are consistent in repeated head fixed sessions, but not in experiments with free behavior 67

Figure 3.14 Self-motion tuning schematic and example self-motion tuning curves 69

Figure 3.15 All self-motion and postural variables are represented across the V1 population 71

Figure 3.16 Groups of cells with strong visual selectivity do not overlap with strongly self-motion tuned groups 73

Figure 3.17 Re-identified cells exhibit separation between visual and self-motion, but larger overlap between orientation and direction selective cells 75

Supp. Figure 1 Examples of cells filtered by distribution-based visual responsivity metric. 105

Supp. Figure 2 Distributions of running wheel and locomotion speeds 106

Supp. Figure 3 Orientation and direction selectivity indices for visually responsive, automatically re-identified cells 107

Supp. Figure 4 Preferred orientation and direction for visually responsive, automatically re-identified cells 108

Supp. Figure 5 Tuning curves of example, hand-picked re-identified neurons change between head fixation and free behavior 109

List of Equations

(2.1) Constrained Non-Negative Matrix Factorization (CNMF) 40

(2.2) Direction Selectivity Index 43

(2.3) Orientation Selectivity Index 43

(2.4) Null Orientation Calculation 43

(2.5) Self-Motion Tuning Curve Responsivity 44

(2.6) Self-Motion Tuning Curve Quality 44

(2.7) Self-Motion Tuning Curve Consistency 44

(2.8) Circular Correlation 46

List of Abbreviations

AP	Action Potential	**OSS**	Open-Source Software
AUC	Area Under the Curve	**PD**	Preferred Direction
CaM	Calmodulin	**PO**	Preferred Orientation
CAVE	Cave Automatic Virtual Environment	**PV**	Parvalbumin
dLGN	Dorsal Lateral Geniculate Nucleus of the Thalamus	**RF**	Receptive Field
DSI	Direction Selectivity Index	**RGC**	Retinal Ganglion Cell
FOV	Field of View	**SC**	Superior Colliculus
FPS	Frames Per Second	**s.c.**	Subcutaneous
GECI	Genetically Encoded Calcium Indicator	**SEM**	Standard Error of the Mean
HOM	Head Orienting Movement	**SOM**	Somatostatin
IOS Imaging	Intrinsic Optical Signal Imaging	**std**	Standard Deviation
i.p.	Intraperitoneal	**UV**	Ultraviolet
IR	Infrared	**V1**	Primary Visual Cortex
LED	Light Emitting Diode	**VIP**	Vasoactive Intestinal Peptide
LP	Lateral Posterior Nucleus of the Thalamus	**VOR**	Vestibulo-Ocular Reflex
MLR	Mesencephalic Locomotor Region	**VR**	Virtual Reality
NIR	Near-Infrared	**2P**	Two Photon
OD	Ocular Dominance	**3D**	Three Dimensional
OKR	Optokinetic Reflex	**3P**	Three Photon
OSI	Orientation Selectivity Index		

Acknowledgements

None of the work described in this thesis would have been possible without the scientific, technical, and personal support of many people.

I am especially grateful to Drago Guggiana Nilo for being a first-class mentor, colleague, and friend. Your guidance and support made everything possible. From being neck-deep in troubleshooting code or equipment to checking in on how I was doing whenever we met, I could always rely on you for help. You've kept my morale up even through the most difficult and frustrating times of the PhD, and the fact that this thesis exists is in no small part thanks to you.

To Mark Hübener, thank you for your scientific guidance these past six years. Your mentorship has been invaluable for my development as an independent scientist. To Tobias Bonhoeffer, thank you for providing me with the freedom and resources to pursue this project down all its twists and turns, and particularly for support with my future career. Many thanks to my thesis advisory committee – Laura Busse, Ruben Portugues, Mark, and Drago – for engaging discussions, critical input, and guidance which made this project better at every step.

I am extremely grateful to Volker Staiger, Claudia Huber, Dominik Linder, Max Sperling, Frank Voß, and Miriam Linnenbrink for all the behind-the-scenes help with histology, setup troubleshooting, equipment repair, and innumerable other responsibilities that keep the lab running – you all are truly the foundation that this lab rests on.

To my current and former officemates Danielle, Adriana, and Martin, thank you for putting up with me for the past five years. Our discussions, commiserations, and celebrations kept my spirits up and helped move this project forward. To Joanna and David, thank you so much for your friendship and for being a key part of some very special moments in my life. A huge thank you to Joanna, Yue, Selina, and Adriana for all your help with cat-related matters. To all the other lab members during my time here - Hiranmay, Joel, Sandra, Isa, Annet, Pieter, Lena, Uwe, Annette, and Maxi, as well as Mike, Diana, and Valerija - thank you for creating a dynamic and encouraging working environment. Completing a PhD is difficult, and you all made the process much more fun.

I am extremely grateful to my family, who despite the time and distance, has been so supportive and encouraging through the ups and downs of doing a PhD and living abroad. My wholehearted appreciation and gratitude go to my partner Alja, who has been my support and sanctuary for the past six years. To write everything you've done to encourage, support, and love me would take a book of its own.

Finally, I want to express my deepest gratitude and respect to all the mice who made the ultimate sacrifice for this work. Your contributions will never be forgotten or taken for granted.

Abstract

Neurons in the mammalian primary visual cortex (V1) are classically described via their selectivity for fundamental visual stimulus features, like grating orientation or spatial frequency. These findings stem from classical experiments where anesthetized animals observed reductionistic visual stimuli, and contemporary studies of the visual system during awake but head restrained experiments corroborate these results. Very recent work probing unrestrained, ethologically relevant behaviors have shown that V1 is implicated in a broad range of task related events, and that V1 neurons exhibit selectivity for non-visual variables like self-motion. However, the relationship between a V1 neuron's classical and freely moving tuning properties is unclear. Recent work shows that rodent V1 responds to head orienting movements and exhibits similar receptive field structure between head restrained and free locomotion conditions, but no other visual tuning properties have been studied under freely moving conditions.

In this study, I examined the interaction of orientation and direction tuning and self-motion representation in binocular V1 of the mouse. I measured visual responses during behavior by employing a virtual reality (VR) arena to present drifting grating Gabor patches to freely moving mice while recording calcium activity with wireless 1-photon miniscopes. I fixed the visual stimulus in the mouse's visual field of view (FOV) while the animal moved unrestrained and imaged the same V1 FOV under consecutive freely moving and head fixed conditions to directly compare responses of the same neurons.

I found that self-motion is broadly represented across V1 neurons, and that they continue to exhibit direction and orientation tuning during free behavior. In a subpopulation of neurons re-identified between head fixed and freely moving sessions, I show that direction and orientation selectivity were stronger during head fixation than free behavior. The preferred orientation of these re-identified cells showed significant consistency between sessions and interestingly displayed a small counterclockwise bias during freely moving sessions. In contrast, their preferred direction was not consistent. Finally, I found that cells strongly tuned to visual stimulus features largely do not group together with cells strongly tuned to self-motion in low-dimensional space, but that many cells exhibit low tuning to both self-motion and visual features.

This study presents a method for measuring classical visual tuning properties in freely moving mice and is the first description of orientation and direction tuning during free behavior. The results support the view that the neocortex inherently encodes sensorimotor information, and that by mixing sensory inputs with self-motion related information, V1 may be able to build a representational space that can be used with predictive processing strategies to better process visual information during free behavior.

1 Introduction

For more than half a century, the mammalian visual cortex has served as the canonical model for information processing in the brain (Douglas and Martin, 2004; Hubel and Wiesel, 1962; Miller, 2016; Niell and Scanziani, 2021; Zeng et al., 2023). Descriptions of the fundamental response properties of visual cortical neurons to features of visual stimuli, such as selectivity for orientation, direction, spatial and temporal frequency, and contrast come from classical studies of carnivorans (e.g. cats and ferrets) or primates (Gilbert and Wiesel, 1990; Hubel and Wiesel, 1968, 1962, 1959; Movshon et al., 1978; Reid et al., 1991). Over the past decades, mice have become the model organism of choice for most vision research due to advances in genetic manipulation tools unavailable in other animals, and the general similarity of the mouse visual system to that of higher mammals (Hübener, 2003; Huberman and Niell, 2011).

Classical laboratory neuroscience has revealed much of the complexity of the structural and functional organization of the early mammalian visual system. Recently, a renewed interest in ethology and behavioral ecology, together with technical advancements for quantifying behavior and recording brain activity in awake, freely behaving animals, has revived the study of the visual system in more naturalistic contexts (Beetz, 2024; Busse et al., 2017; Hoffmann et al., 2023; Miller et al., 2022, 2019; Pereira et al., 2020). Despite their lack of visual acuity, mice use vision in a suite of behaviors critical to their survival, including catching prey (Hoy et al., 2019, 2016; Michaiel et al., 2020), foraging (Havenith et al., 2018), defense and predator avoidance (Blanchard et al., 1998; De Franceschi et al., 2016; Yilmaz and Meister, 2013; Zhao et al., 2014), spatial perception and navigation (Boone et al., 2021; Fox, 1965; Parker et al., 2022a; Saleem et al., 2018; Samonds et al., 2019), finding shelter (Shamash et al., 2021), and nesting (Clark et al., 2006).

The resurgence of the neuroethological approach has been a boon for vision research, yet the relationship between how visual cortex neurons represent fundamental visual stimulus features and their responses during naturalistic behaviors remains elusive. Many theories of mammalian visual processing assume invariance in the neural representations of stimuli based on the hierarchical organization and feed-forward computations observed in sensory cortex (for an overview, see DiCarlo et al. (2012)

and Miller (2016)), yet the study of sensory processing during naturalistic behaviors suggests that the brain processes information both in invariant and contextually-adjustable ways (Miller et al., 2022). Typically, animals in classical visual neuroscience experiments were anesthetized, awake but paralyzed, or awake but head-restrained, and presented with strong but generally abstract and reductionist visual stimuli like random dot stereograms or moving black and white bars. This was, and still is, a technical necessity, as measuring visual tuning properties requires knowing where exactly a stimulus falls in the animal's visual field due to the spatial locality of visual receptive fields (Hartline, 1938; Hubel and Wiesel, 1959). However, self-motion is represented ubiquitously across the neocortex during both head fixation and free behavior (Mimica et al., 2023; Musall et al., 2019; Salkoff et al., 2020; Stringer et al., 2019; West et al., 2022; Zagha et al., 2022), and locomotion and head and eye movements are also known to modulate and drive the activity of neurons in V1 (Bouvier et al., 2020; Guitchounts et al., 2020; Keller et al., 2012; Meyer et al., 2018; Miura and Scanziani, 2022; Niell and Stryker, 2010; Parker et al., 2023, 2022b; Rancz et al., 2015; Vélez-Fort et al., 2018). This immediately raises a question: if visual responses are so affected by self-motion and behavioral state, do visual tuning properties defined under head fixed conditions change during free behavior?

In a major step towards finding an answer, one recent study in mouse V1 found that spatiotemporal receptive fields (RFs) measured during free behavior are comparable to those measured during head fixation in the same cells (Parker et al., 2022b). This study utilized head mounted cameras to observe the movement of the mouse's eyes and surroundings as he moved about an arena surrounded with standard visual stimuli and leveraged computational methods to back-calculate the observed visual scene during free behavior. However, this approach does not ensure that the mouse will see a given visual stimulus for long enough or with enough repetitions to reliably measure response properties like orientation or direction selectivity.

To measure orientation and direction tuning in a freely behaving animal, one needs to know where in the visual field a visual stimulus is presented and guarantee a minimum number of repetitions of the stimulus to robustly characterize the responses, as neurons show variance in their responses to repeated presentations of the same stimulus (Butts et al., 2007; Liu et al., 2001; Reinagel and Reid, 2000; Shadlen and Newsome, 1998). Instead of back calculating the location of the image on the retina

from a head mounted camera, one could instead tightly control the visual environment of a freely moving animal. To achieve this, I leveraged advances in immersive virtual reality systems developed for rodents to create perspective-corrected visual environments that allowed presenting drifting grating Gabor stimuli to freely moving mice. Using miniaturized functional microscopy, I measured V1 neural responses to both visual stimuli and self-motion. To evaluate how free behavior modulates visual response properties, I compared the tuning properties of cells re-identified between consecutive head fixed and freely moving sessions.

Through the following sections, I provide a brief overview of the organization of the early visual system of the mouse and how visual tuning properties arise. I pay particular attention to recent results highlighting the plethora of nonvisual responses that have been observed in V1 and how they interact with visual ones. I then provide background on the two major methodologies used in the study, the one-photon miniature microscope (miniscope) and VR environments.

1.1 Organization of the Mouse Early Visual System

Mice, like all mammals, see the world with two eyes. The signals produced by the image projected on the retinas are then transmitted to over 40 structures throughout the brain (Morin and Studholme, 2014). Information reaches V1 from the retina via two pathways. In the image-forming pathway, information passes from the retina via the dorsal lateral geniculate nucleus of the thalamus (dLGN) to V1. In the non-image-forming pathway, visual information flows from the retina to the superior colliculus (SC), where it undergoes visuo-motor processing. In particular, outputs from the intermediate and deep layers of the SC are implicated in a range of visually-informed motor behaviors like motion arrest, turning, prey capture, and escape (Wheatcroft et al., 2022). Visual outputs from the SC project to the dLGN and the lateral posterior nucleus of the thalamus (LP) (Benavidez et al., 2021), which both project to V1 (and LP also to higher visual areas) (Seabrook et al., 2017a). From V1, visual information is passed on to a number of higher visual (or extrastriate) areas with distinct functional properties (**Figure 1.1**, (Priebe and McGee, 2014; Wang and Burkhalter, 2007)).

Despite their low visual acuity compared to other mammals (0.6 cycles/º in the mouse (Gianfranceschi et al., 1999; Sinex et al., 1979) vs. 60 cycles/º in humans (Campbell

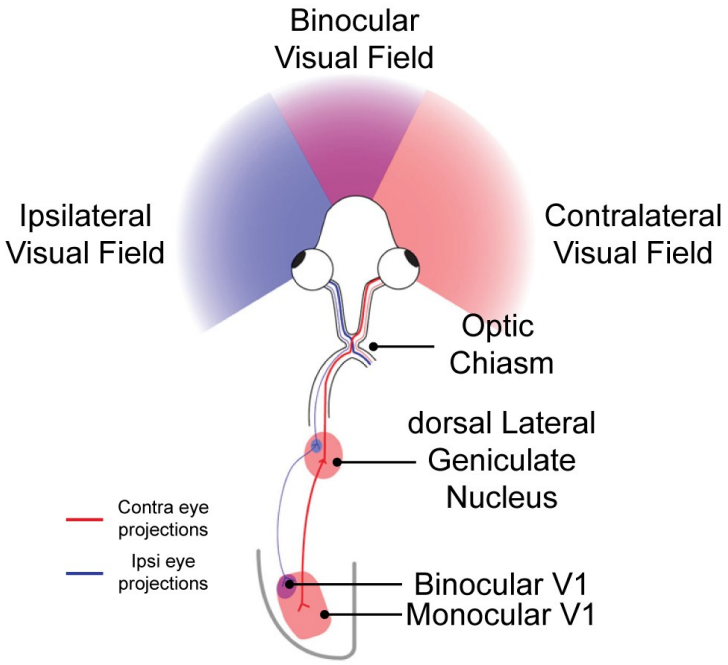

Figure 1.1 Organization of the imaging forming pathway of the early rodent visual system | Schematic of canonical eye-specific projections from the retina to the dLGN and V1. In rodents, laterally placed eyes sample the visual scene from two large monocular visual fields and a smaller binocular visual field. The vast majority of RGC axons cross to the contralateral hemisphere at the optic chiasm. Canonically, both ipsi- and contralateral projections terminate in the dLGN in eye-specific domains. V1 receives dLGN input exclusively from the contralateral eye in the monocular domain, and from both eyes in the binocular domain. Adapted with permission from Priebe and McGee (2014).

and Green, 1965)), reduced binocular visual field (30º - 40º, or approximately 30% of their visual field (Dräger, 1978; Dräger and Olsen, 1980; Gordon and Stryker, 1996)), and differences in functional architecture (namely the absence of iso-orientation columns like those in cats and macaques (Bonhoeffer and Grinvald, 1991; Dräger, 1975; Hubel et al., 1977)), mice exhibit all of the receptive field property types found in higher mammals (Dräger, 1975; Mangini and Pearlman, 1980; Métin et al., 1988).

1.1.1 The Retina

The retina samples the three-dimensional scene available to each eye by collapsing it into a two-dimensional image. Mice are non-foveate animals, and so do not have a fovea, a distinct region of exceptionally high photoreceptor density compared to the periphery. However, the mouse retina does exhibit modestly increased cone density in the central retina that falls off towards the periphery, resulting in regions of greater visual acuity (Bleckert et al., 2014; Dräger and Olsen, 1981; van Beest et al., 2021;

Volland et al., 2015). One class of rod and two classes of cone photoreceptor cells interact with incoming photons, converting incident light into neuronal signals. Outputs from the rods and cones are passed to retinal ganglion cells (RGCs) via a network of bipolar, amacrine, and horizontal cells (Masland, 2012).

RGCs are classically characterized by center-surround receptive fields, where increases or decreases in luminance in small, localized regions of visual space elicit responses, while the surrounding annular region is excited by stimuli with the opposite luminance (Hartline, 1969; Kuffler, 1953). Other RGCs have more specialized response properties, such as detecting edges or the direction of stimulus movement (Barlow et al., 1964; Sanes and Masland, 2015). RGC axons are bundled in the optic nerve, where the vast majority (95-97%) cross to the contralateral hemisphere at the optic chiasm (Johnson et al., 2021; Petros et al., 2008). The primary projections of the optic nerve are the SC and the dLGN.

1.1.2 The Superior Colliculus

In mice, the SC is the subcortical structure that receives the most input from the retina, innervated by approximately 85 - 90% of RCGs (Ellis et al., 2016). Neurons in the SC exhibit response properties like those in the retina, dLGN, and visual cortex, including orientation, direction, and speed selectivity, as well as center-surround suppression (Ahmadlou and Heimel, 2015; Feinberg and Meister, 2015; Gale and Murphy, 2014; Seabrook et al., 2017b; Shi et al., 2017) and are retinotopically organized, meaning adjacent cells preferentially respond to stimuli localized to restricted and partially overlapping areas of visual space, creating a tiled representation of the entire visual field (Dräger and Hubel, 1976, 1975a, 1975b). As the SC is directly involved in several visually mediated behaviors, including predator avoidance, prey capture and target selection (Campagner et al., 2023; Hoy et al., 2019; Zhen, 2017), many SC neurons respond to very different visual stimulus features, like looming stimuli or particular combinations of size and speed.

1.1.3 The Dorsal Lateral Geniculate Nucleus

The dLGN is the primary visual input source to the cortex, receiving input from 30-40% of all RGCs in the mouse (Ellis et al., 2016; Morin and Studholme, 2014). The dLGN

is classically described as a relay station between the retina and the visual cortex, exhibiting segregated regions receiving retinotopically organized input specific to either the contralateral or ipsilateral eye. In mice, most neurons respond exclusively to inputs from one eye, even when receiving binocular input (Bauer et al., 2021; Huh et al., 2020; Jaepel et al., 2017). Despite its reputation as a relay, recent work has highlighted the role of the dLGN in visual processing. The dLGN receives retinotopically organized feedback projections from V1, forming an early thalamo-cortical feedback circuit (Born et al., 2021), and the presence of orientation and direction selective neurons (Cheong et al., 2013; Grubb and Thompson, 2003; Marshel et al., 2012; Piscopo et al., 2013; Sun et al., 2016; Zhao et al., 2013) together with observations of visual response modulation by locomotion, speed, and other behavioral parameters (Aydın et al., 2018; Erisken et al., 2014; Orlowska-Feuer et al., 2022; Socha et al., 2024; Spacek et al., 2022) point towards the dLGN's active role in visual processing.

1.1.4 The Primary Visual Cortex

Much of the classical work describing the function and organization of the visual cortex comes from experiments done in carnivorans or primates. While there are some key differences between those animals and mice, the general functional organization of mouse V1 is the same. The primary visual cortex, like most of the neocortex, is organized into six layers. In mice, approximately 70-80% of neurons in V1 are excitatory, with the remaining 20-30% consisting of genetically defined classes of inhibitory interneurons, with the three most important being parvalbumin (PV), somatostatin (SOM) and vasoactive intestinal-peptide (VIP) expressing neurons. PV, SOM, and VIP neurons are present in roughly equal proportions (Harris and Shepherd, 2015; Jiang et al., 2015; Tremblay et al., 2016; Zeng and Sanes, 2017). Information flow through V1 follows the canonical circuit that is typically found across cortical areas in mammals (Douglas et al., 1989; Douglas and Martin, 1991; Miller, 2016; Niell and Scanziani, 2021). Visual input primarily enters V1 via layer 4 from the LGN, while lower layer 2/3, layer 6, and layer 1 also receive modest thalamic input (Antonini et al., 1999; Cruz-Martín et al., 2014; Harris and Shepherd, 2015; Hubel and Wiesel, 1972; Jiang et al., 2015). Layer 2/3 cells receive feedforward input from layer 4, where it is locally processed by cells that code for similar visual features (Glickfeld et al., 2013) before

being sent either to higher visual areas via long-range projections or locally propagated to layer 5. From layer 5, information is passed to layer 6, subcortical structures such as the SC and dLGN, and across the corpus callosum to the opposite hemisphere (Kasper et al., 1994; Swadlow, 1983). Layer 6 cells also target subcortical regions like the LGN and the callosum, as well as layer 4 cells, providing further feedback to the visual circuit (Olsen et al., 2012).

Like the SC and dLGN (and other visual thalamic areas like LP), V1 neurons are retinotopically organized (Dräger, 1975; Hubel and Wiesel, 1968, 1962). The representation of visual space is, however, non-uniform on the cortical surface, with the binocular visual field being overrepresented (van Beest et al., 2021). This is largely driven by inputs from both eyes converging in binocular V1 (Dräger, 1978; Gordon and Stryker, 1996). Consequently, the cortical magnification factor (Daniel and Whitteridge, 1961), or ratio between the distance of two points in visual space and the distance between the representations of those points on the cortical surface, increases in regions representing the central retina (Garrett et al., 2014). While the reason for the over-representation of the binocular visual field in mice is unknown, recent results from prey capture studies show that mice move their heads and eyes to keep prey in the central visual field (Han et al., 2017; Holmgren et al., 2021; Hoy et al., 2016; Michaiel et al., 2020; Park et al., 2018), perhaps indicating that the binocular visual field is preferentially used during survival-critical behaviors.

1.2 Visual and Nonvisual Stimulus Coding in V1

The primary visual cortex, as outlined above, processes feedforward visual information from the retina via the dLGN and SC. The properties of visual stimuli represented by V1 have been thoroughly investigated over the past 65 years, with research showing that neurons in V1 represent visual features such as luminance, contrast, orientation, direction, spatial and temporal frequency, and depth. However, recent work clearly demonstrates that V1 neurons encode and are modulated or driven by a diversity of non-visual factors, including arousal (Niell and Stryker, 2010; Reimer et al., 2014; Vinck et al., 2015), movement (Keller et al., 2012; Niell and Stryker, 2010; Reimer et al., 2014; Saleem et al., 2013; Vinck et al., 2015), allocentric location (Diamanti et al., 2021; Saleem et al., 2018), and decision making (Goard et al., 2016). In addition, task-

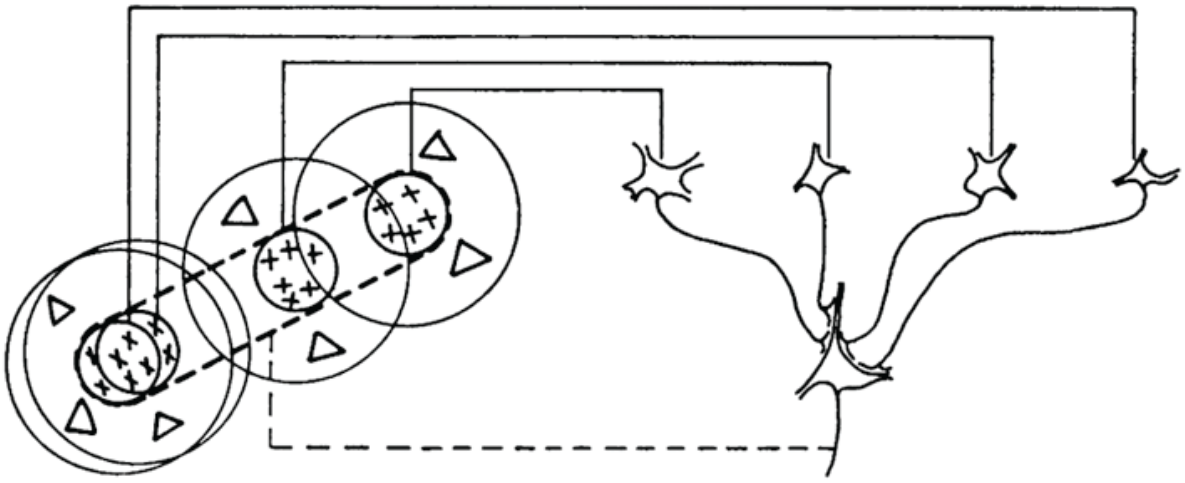

Figure 1.2 Visual receptive fields in the early visual system | Original model for the generation of orientation selectivity in cat V1 by selective feedforward convergence. In this example, dLGN cells (left) have circular receptive fields with a central ON domain and surrounding OFF domain. Cells with RFs aligned in visual space project to a single cortical simple cell where the RFs are linearly summed to create ON and OFF subdomains, rendering the V1 cell sensitive to oriented stimuli. Reprinted with permission from Hubel and Wiesel (1959).

related variables like stimulus relevance (Keller et al., 2017), visual categories (Goltstein et al., 2021) and reward (Fiser et al., 2016; Liu et al., 2015; Shuler and Bear, 2006) are represented, as well as auditory and somatosensory stimuli (Deneux et al., 2019; Ibrahim et al., 2016; Iurilli et al., 2012; Meijer et al., 2017; Sieben et al., 2013; Slezak et al., 2019). In this section, I briefly discuss the classical visual tuning properties which have been richly described since Hubel and Wiesel and expand the discussion of stimulus coding in V1 to nonvisual variables, with particular emphasis on the representation of self-motion in V1.

1.2.1 Visual Stimulus Coding

1.2.1.1 Binocularity and Ocular Dominance

As discussed previously, V1 is retinotopically organized based on the innervation pattern of dLGN projections into layer 4. While cells in the visual thalamus primarily respond to inputs from one eye over the other (so-called eye preference, although see Jaepel et al. (2017) and Bauer et al. (2021) for discussions of ocular dominance in dLGN), the neurons in the visual cortex integrate and weight inputs from both eyes.

The relative contribution of each eye to the processing of visual information in these cells is termed ocular dominance (OD).

1.2.1.2 Retinotopic Organization and Receptive Fields

In the early visual system, cells respond to visual input from a spatially restricted part of the visual field, called the receptive field. RFs in the retina and dLGN are classically described by a center-surround structure, where a visual stimulus that falls in the center of the receptive field tends to activate or suppress the cell, while stimuli that fall outside of this central region tend to act oppositely on the activity of the cell (Blakemore and Tobin, 1972; Hubel and Wiesel, 1959; Van den Bergh et al., 2010). Besides these classical RF properties, several extra-classical RF properties have been described. Stimuli located outside of classical RF may exert a suppressive effect on a neuron, known as surround suppression (Blakemore and Tobin, 1972; Hubel and Wiesel, 1968), and contrast and orientation of visual stimuli presented in the RF surround have also been shown to modulate neural responses (Glickfeld et al., 2013; Nienborg et al., 2013). In the retina and dLGN, RFs tend to be small and circular. Moving along the visual pathway, RFs increase in size and change shape, often becoming elongated or even more complex (**Figure 1.2**).

1.2.1.3 Orientation and Direction Tuning

Classical RFs in the cortex exhibit responses evoked by stimuli with a preferred orientation or direction and are suppressed by stimuli with orientations or directions orthogonal to the preference. Orientation tuning was first described in cat V1 in seminal papers from David Hubel and Torsten Wiesel in 1959 and 1962 (Hubel and Wiesel, 1962, 1959). They found that neurons strongly responded to bars or edges presented at specific orientations in visual space (the preferred orientation, or PO), with decreasing responsivity to orientations rotated away from the PO. Further, some cells were specifically responsive to oriented edges that moved in a direction perpendicular to their orientation (the preferred direction, PD). For example, a cell that preferentially responds to a vertical black bar moving exclusively to the right exhibits orientation selectivity, but also is considered direction selective, where a different cell that responds to the same vertical bar moving to either the left *or* the right is only orientation selective. The strength of orientation and direction tuning is assessed by

metrics known as the orientation or direction selectivity index (OSI and DSI, respectively). The OSI is calculated either using the circular variance of the tuning curve, or as the ratio of response between the PO and the orientation perpendicular to the PO, while DSI is calculated as the ratio of responses to the PD and the direction directly opposite (see **Methods 2.2.10.4.3**).

In higher mammals, neurons with similar orientation preference tend to cluster together, forming columns of orientation selectivity through all cortical layers (Bonhoeffer and Grinvald, 1991; Hubel and Wiesel, 1968, 1962). This organization is not observed in mice, however. While many mouse V1 neurons are both orientation and direction selective and have tuning curves similar to those observed in other species (Dräger, 1975; La Chioma et al., 2020; Métin et al., 1988; Niell and Stryker, 2010, 2008), there is instead a mostly random “salt and pepper” topographical organization of orientation and direction tuned cells (Kondo et al., 2016; Ohki et al., 2005), although some local spatial clustering has been reported (Ringach et al., 2016).

1.2.2 Nonvisual Stimulus Coding

1.2.2.1 Nonvisual Connectivity of V1

Neurons in V1 are responsive to features of visual stimuli, but their responses are not limited to just features of the visual scene. Such responses are not unexpected, as mouse V1 is highly interconnected, receiving afferent projections from more than 24 brain regions (**Figure 1.3 A**, Froudarakis et al., 2019). This includes the classical visual areas, including higher visual areas and thalamic nuclei like the dLGN, the lateral dorsal nucleus (LD) and LP (which itself receives afferent projections from the SC) (Benavidez et al., 2021; Seabrook et al., 2017a).

Non-visual areas are also connected to V1, including the motor and anterior cingulate cortices, retrosplenial cortex, orbitofrontal areas (including the olfactory and gustatory

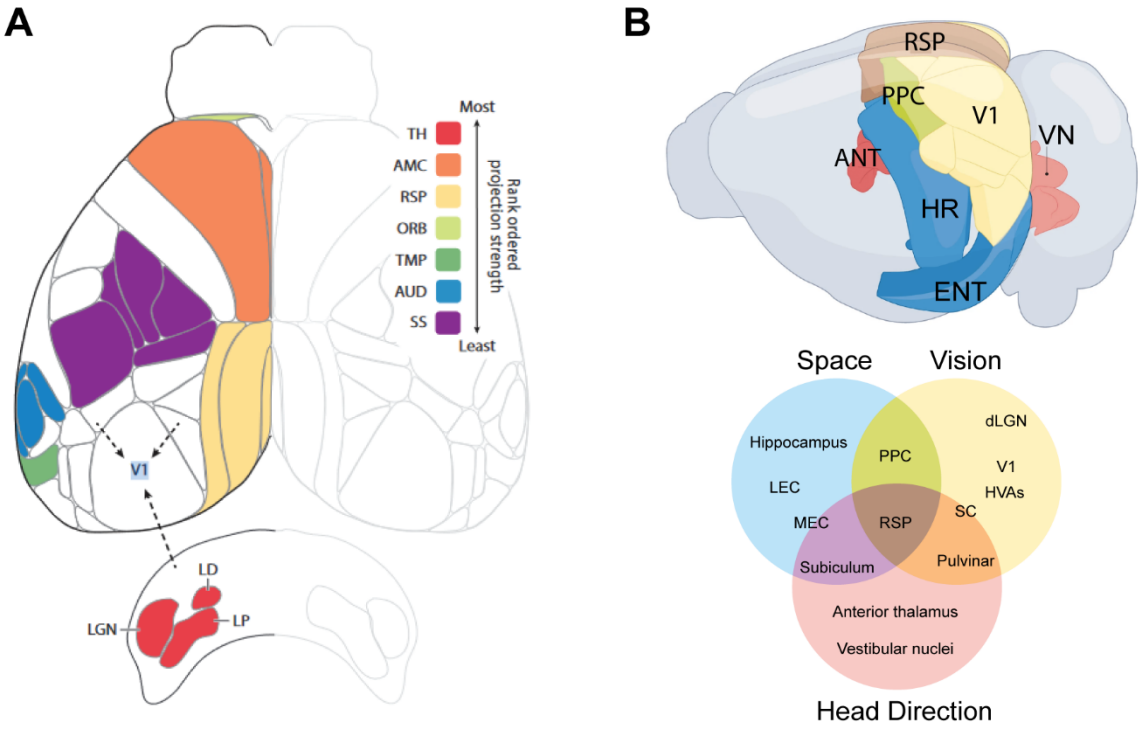

Figure 1.3 Nonvisual projections to V1 and overlap in areas representing vision, navigation, and motion | A. Map of afferent projections to V1. TH – thalamic nuclei; LD lateral dorsal nucleus of the thalamus; LP – lateral posterior nucleus of the thalamus; AMC – anterior cingulate and secondary motor areas; RSP – retrosplenial areas; ORB – orbital areas; TMP – temporal areas and entorhinal cortex; AUD – auditory cortex; SS – somatosensory cortex. Reprinted with permission from Froudarakis et al. (2019). **B.** *(Upper)* Schematic of brain regions involved in visual processing and navigation. *(Lower)* Overlap in brain areas part of the vision, space, and head direction systems. ANT – anterior group of the dorsal thalamus; HR – hippocampal region; ENT – entorhinal cortex; LEC – lateral entorhinal cortex; MEC – medial entorhinal cortex; HVAs – higher visual areas; VN - vestibular nuclei. Reprinted with permission from Saleem and Busse (2023).

cortices, which interact with the amygdala), temporal areas such as the entorhinal cortex (which have access to the hippocampus), and the auditory and somatosensory cortices (Morimoto et al., 2021; Oh et al., 2014; Weiler et al., 2024). For a comprehensive review of the connectivity of rodent V1, see Froudarakis et al. (2019).

Taken together, V1 has access to information from all sensory modalities, as well as motor, navigational and spatial information.

1.2.2.2 Interactions of Position and Self-Motion with Visual Responses

The integration of non-visual variables in V1 is thought to help flexibly represent the landscape that an organism navigates, allowing it to respond to constantly evolving situations. Indeed, a large body of work now shows that vestibular, self-motion, and posture signals are found ubiquitously the brain and have a modulatory effect on the thalamus (Erisken et al., 2014; Orlowska-Feuer et al., 2022) and neocortex (Keshavarzi et al., 2023; Mimica et al., 2023; Musall et al., 2019; Salkoff et al., 2020; Stringer et al., 2019; West et al., 2022; Zagha et al., 2022), although the types of encoded movements seem to vary in a region-specific manner (Wang et al., 2023).

1.2.2.2.1 Position

The integration of allocentric position and visual input was thought to occur later in the visual processing pathway, in higher visual areas (Glickfeld and Olsen, 2017; Saleem, 2020). As mentioned above, retinotopy – the representation of visual space from an ‘eye-centric’ view - is considered a fundamental coding property in the early visual system. Accordingly, responses recorded in V1 to the same visual stimulus in the same part of the visual field should be invariant to the location of the animal in space. However, recent work has shown that V1 differentially responds to the very same visual stimulus depending on the allocentric location of a mouse in a virtual reality arena (Diamanti et al., 2021; Fiser et al., 2016; Saleem et al., 2018) or the distance travelled in a virtual corridor (Fournier et al., 2020). This work builds on previous studies which suggested that responses in rodent visual cortex may be modulated by allocentric position (Haggerty and Ji, 2015; Ji and Wilson, 2007), challenging the classical view that the early visual system exclusively uses a retinotopic frame of reference.

1.2.2.2.2 Locomotion

Early studies of visual processing in awake mice quickly demonstrated that V1 responses are strongly modulated and even driven by locomotion (Andermann et al., 2011; Keller et al., 2012; Niell and Stryker, 2010; Reimer et al., 2014). V1 neurons are selective for locomotion speed and visual stimulus size, with size selectivity dependent on speed (Ayaz et al., 2013; Saleem et al., 2013). Locomotion speed and drift speed of the visual stimulus were shown to be linearly summed in V1 neurons, integrating visual and locomotion-related signals, presumably for visually-guided navigation (Ayaz et al., 2013; Keller et al., 2012; Saleem et al., 2013). The gain amplification observed in V1 neurons driven by locomotor initiation was later found to be linked to activity in the mesencephalic locomotor region (Lee et al., 2014).

Mismatch signals, where motor activity and visual input are decoupled, were shown to elicit strong responses, consistent with ideas of predictive processing (Keller et al., 2012; Keller and Mrsic-Flogel, 2018; Vasilevskaya et al., 2023) (although see Muzzu and Saleem (2021) for arguments against the predictive processing model). The predictive processing model posits that the brain distinguishes between external and self-generated sensory input by passing a copy of a motor command (called an efference copy) through an internal generative model to predict the sensory input resulting from the movement. This requires transforming the efference copy from motor space into sensory space, where the transformed efference copy is then called corollary discharge. Mismatches between the expected self-generated sensory input and the experienced input are then used to update the internal model to minimize future prediction errors.

1.2.2.2.3 Head and Eye Movements in Mice

During active behavior, eye movements have been found to be mostly compensatory for head movements, working to stabilize the visual gaze to the horizontal plane, maintain the binocular FOV, and keep tracked objects in the part of the visual field with the least optic flow (Holmgren et al., 2021; Meyer et al., 2020, 2018; Parker et al., 2022b; Wallace et al., 2013). Active eye movements generated by an animal to change the visual scene on the retina (like saccades or gaze shifts), reflexive eye movements used to stabilize the visual scene on the retina (like the optokinetic and vestibulo-

ocular reflexes) and head movements are robustly represented in rodent V1 both in the light and the dark (Bouvier et al., 2020; Guitchounts et al., 2020; Meyer et al., 2018; Miura and Scanziani, 2022; Parker et al., 2023, 2022b; Rancz et al., 2015; Vélez-Fort et al., 2018), consistent with earlier work done in primates (Felleman and Van Essen, 1991; Herrington et al., 2009; Martinez-Conde et al., 2000).

Head movements were shown to have luminance dependent modulatory effect on V1 responses, with head rotations suppressing V1 activity in darkness (Bouvier et al., 2020; Guitchounts et al., 2020). In the light, head orienting movements (HOMs) enhance V1 activity during both passive, restrained rotations and free behavior (Bouvier et al., 2020; Guitchounts et al., 2020; Vélez-Fort et al., 2018). Guitchounts et al. (2020) also report that populations of cells that encode HOMs are largely independent between illumination conditions. Interestingly, these effects seem to be layer dependent, with layer 6 cells showing consistent response enhancement to HOMs in both the light and the dark (Bouvier et al., 2020; Vélez-Fort et al., 2018) while layer 2/3 cells that were suppressed by HOMs in the dark were later enhanced by HOMs in the light (Bouvier et al., 2020; Guitchounts et al., 2020; Vélez-Fort et al., 2018).

Recent work by Parker et al. (2023), where V1 was recorded simultaneously with head and eye movements in freely moving mice, is particularly relevant. In this study, mouse V1 neurons were shown to respond to gaze-shifting eye movements, where both the head and eyes moved in the same direction to change the visual scene, but not to gaze-stabilizing head movements. These responses followed a temporal sequence, with early and late positive responses followed by biphasic and then negative responses, that were only present when mice moved through an illuminated arena. The temporal sequence showed preference for increasing spatial frequency, perhaps indicating a mechanism for course-to-fine visual processing in mouse V1.

Taken together, the connectivity and observed modulation and drive of V1 neurons by nonvisual inputs points towards sensorimotor integration as an essential property of V1.

1.3 Optical Interrogation of Neural Activity *in vivo* During Free Behavior

From the above, it is clear that achieving a full understanding of information processing in the brain requires mapping cortical circuits with fine spatial and temporal resolution *in vivo*. While electrophysiological recordings offer precise temporal measurement of neural activity of individual cells, the number of cells that can be simultaneously recorded is generally low. Multi-electrode extracellular recordings, such as those from Neuropixels probes (Jun et al., 2017; Steinmetz et al., 2021), overcome the problems of small populations by sampling hundreds of cells simultaneously. However, these methods are limited in their ability to localize recorded cells, have increased uncertainty of recording from the same cell as experimental durations extend to days or weeks, and cannot distinguish individual cell types without more advanced biological methods. Over the past two decades, developments in optical methods, like single- and multi-photon microscopy, together with advances in fluorescent reporters of neural activity such as calcium, glutamate, serotonin, or voltage sensors (Dimitrov et al., 2007; Dinarvand et al., 2019; Hires et al., 2008; Nakai et al., 2001; St-Pierre et al., 2014), have delivered powerful new tools for visualizing the activity of large numbers of neurons with high temporal fidelity over extended periods of time.

1.3.1 General Principles of Calcium Imaging *in vivo*

Ideally, imaging approaches would directly record changes in membrane potential with voltage indicators. However, limitations in currently available voltage indicators, including phototoxicity, small fluorescence changes, and short response durations, have limited their adoption (Lin and Schnitzer, 2016). Instead, calcium imaging has found widespread popularity for visualizing neuronal activity.

1.3.1.1 Calcium Indicators

Calcium imaging relies on the use of calcium indicators, which are molecules that modify their fluorescence properties upon binding calcium. Calcium is a secondary messenger involved in membrane depolarization and neurotransmitter release. Calcium ions (Ca^{2+}) enter neurons via several routes during the depolarization phase

of an action potential (AP) or with synaptic input to dendrites, generally with fast rise and slow decay kinetics (Grienberger and Konnerth, 2012). Intracellular Ca^{2+} concentrations increase with synaptic input or depolarization (i.e. APs), and the inflowing calcium binds to the calcium indicator, causing a modulation in fluorescence (Paredes et al., 2008; Tian et al., 2012). As the concentration of intracellular calcium returns to baseline, the fluorescence of the indicator molecules also returns to baseline. The binding of Ca^{2+} to some calcium indicators is relatively slow compared to fluctuations in the electrical activity of neurons, and so detectable changes in fluorescence may comprise multiple APs. Further, the fluorescence change of most calcium indicators is nonlinearly linked to changes in intracellular Ca^{2+} concentration, and may saturate when intracellular Ca^{2+} remains consistently high, such as during a sustained spike train (Akerboom et al., 2012; Paredes et al., 2008). Therefore, it is important to note that changes in the fluorescence of calcium indicators serve as a proxy for neural activity as opposed to a direct readout.

For more than a decade, the most widely used calcium indicators have been genetically encoded calcium indicators (GECIs), particularly those from the GCaMP family (Lin and Schnitzer, 2016; Tian et al., 2012). GCaMP is a fusion protein consisting of a modified green fluorescent protein (GFP) and the calcium-binding protein calmodulin (CaM) (Nakai et al., 2001). Upon binding calcium, the conformation of GCaMP molecules changes such that the emission intensity of the GFP domain increases (Akerboom et al., 2009). GCaMP proteins are encoded by DNA and can be directly expressed in neurons through electroporation of single cells, gene transfer via viral transduction, or via transgenic animal lines (Nevian and Helmchen, 2007; Tian et al., 2009). When combined with cell-type-specific or activity-dependent promoters, GECIs can be expressed in specific cell populations *in vivo*. A variety of GCaMPs exist, with faster or slower temporal dynamics, and with modifications that allow the molecule to be targeted to parts of the cell, such as the cell membrane, nucleus, soma, or even ribosomes (Chen et al., 2020; Erofeev et al., 2023; Kim et al., 2014; Shemesh et al., 2020). The most recent versions of GCaMP have optimized for speed and signal to noise ratio, with rise times on the order of 10 ms, and are capable of reliably detecting single APs in spike train frequencies up to 50 Hz (Yan Zhang et al., 2023).

1.3.1.2 Single and Multi-Photon Fluorescence Microscopy

In fluorescence microscopy, contrast is created when a fluorophore is excited by the absorption of one or more photons, typically in the ultraviolet (UV) to blue spectrum. Excitation photons carry enough energy to force electrons in the fluorophore to jump from a ground state to an excited state, which then upon return to ground sate emits a photon of lower energy and thus a longer wavelength (typically within the green to infrared (IR) spectrum) and lower energy.

Single photon imaging approaches excite the fluorophore of interest with one photon of sufficiently high energy (shorter wavelengths, typically in the blue spectrum), which can come from light sources ranging from simple light emitting diodes (LEDs) to pulsed lasers. One photon imaging excites fluorophores in a “column” of light passing through the sample, which leads to the collection of fluorescence signals that lie outside the focal plane of the imaging system. As the brain is both a highly non-transparent medium and scatters light, one photon imaging is limited to relatively shallow depths below the imaging surface without the addition of more advanced optical approaches (e.g. confocal microscopy).

Multiphoton approaches, such as two- or three-photon imaging, leverage a property of some fluorophores by which the near-simultaneous absorption of lower energy (longer wavelength) photons will deliver the requisite energy to excite the fluorophore (Göppert-Mayer, 1931). For two photon imaging, the wavelength of light used to excite a fluorophore is approximately double the wavelength of that used in one photon approaches; three photon imaging works analogously. The probability of the coincident absorption of two or more photons to excite the fluorophore is extremely low (Denk et al., 1990; Hell et al., 1996). As the intensity of a focused light beam is highest at its focus and decays at a rate of $1/z^2$ (where z is the axial distance from the focus), multiphoton excitation is confined to a small volume around the focal point and out-of-focus fluorescence is drastically reduced. To achieve a photon density sufficient for multi-photon effects, light must be produced by a focused laser beam from a pulsed (femtoseconds) laser to maintain high intensity with low average power. Multiphoton imaging allows for imaging deeper into brain tissue, as longer excitation wavelengths are less affected by scattering and are less likely to be absorbed by endogenous chromophores in the brain.

1.3.2 Miniaturized *in vivo* Microscopy (Miniscopes)

The study of the visual system with optical methods is traditionally limited to experiments where the subject is (at least partially) restrained. Most functional microscopy techniques require a large tabletop apparatus and demand the subject to remain still to prevent excessive motion of the brain and subsequent recording artifacts. This can be overcome by with anesthesia or paralytics, but anesthesia has severe effects on neural activity, such as reduction in overall activity levels, changes in stimulus-specific tuning properties, or the synchronous activity at the population level (Durand et al., 2016; Niell and Stryker, 2010; Ruiz-Mejias et al., 2011). Further, neither anesthesia nor paralytics remove motion artifacts resulting from heartbeat or (in the case of paralytic usage) ventilation, and such techniques are obviously inappropriate for studies in awake, moving animals.

Since it is somewhat futile to ask a monkey or mouse to sit still for an experiment, head restraint is widely practiced in visual neuroscience. Contemporary tabletop imaging approaches allow for mice to walk or run on air-suspended balls, platforms, or treadmills, and even pseudo-burrow (Fink et al., 2019) during a head-restrained experiment. Such methods allow the examination of more complex and somewhat naturalistic behaviors, yet still suffer the problem of being potentially stressful to the animal (Juczewski et al., 2020) (although voluntary head fixation strategies mitigate much of the stress caused by head restraint, see Aoki et al., (2017) and Rich et al., (2023)). However, as described above, self-motion signals, especially signals related to head motion, are ubiquitous in sensory cortex, and any head fixation preparation will be unable to fully capture their contributions to neural activity.

The idea of miniaturizing microscopes for *in vivo* functional microscopy in freely moving animals originated over twenty years ago (Helmchen et al., 2001). There has been a recent flurry of development of miniaturized one photon miniscopes from both commercial sources and the open-source community (de Groot et al., 2020; Ghosh et al., 2011). Many of these miniscopes carry on-board LED excitation sources and complementary metal-oxide-semiconductor (CMOS) imaging sensors to record the emitted florescence and have FOVs on the order of hundreds of microns, allowing animals equipped with miniscopes to roam while minimally encumbered by fiber optic and data cables. The miniscope used in this study was the UCLA version 3 miniscope

with a wireless recording attachment (Ghosh et al., 2011), which introduces a battery to power the LED and CMOS sensor and SD card for on-device data saving. The wirefree UCLA V3 miniscope was chosen specifically such that no cables were present to distort the visual stimulus and to remove weight and torquing forces caused by cable slack that would cause excessive load on the mouse. Despite the additional weight introduced by the battery, the wirefree miniscope allows an acclimated animal to behave freely without any tethers.

Very recent technological developments have also delivered upon the dream of commercially available miniature two photon (mini-2P) (Zong et al., 2022) and even early-stage miniaturized three photon (mini-3P) microscopes (Klioutchnikov et al., 2023; Zhao et al., 2023). While the mini-2P and mini-3P microscopes exhibit the imaging benefits of their tabletop counterparts, they are complex to build, have relatively limited FOVs, and still require expensive tabletop lasers to generate the multi-photon effect. The reliance on tabletop lasers means he mini-2P and mini-3P microscopes will always be cabled, barring the invention of miniaturized femtosecond lasers.

1.4 Visual Stimulation During Free Behavior

1.4.1 Visual Stimulation in Head Restrained Animals

Knowing exactly where a stimulus falls in visual space is crucial for understanding visual processing. Visual stimuli, such as drifting gratings, sparse noise, or random dot stereograms, are typically presented to animals on liquid crystal display (LCD) computer screens positioned at a known distance and position from the animal's eyes (**Figure 1.4 A**). To mimic the spherical nature of the natural visual field, such stimuli are often corrected to reproduce the experience of viewing the stimulus of interest on the inside surface of a sphere. This preserves the size and spatial frequency of the visual stimulus on the retina regardless of where it is presented in the visual field. A different but analogous approach is to project visual stimuli onto a toroidal screen with a projector and hemispherical mirror (**Figure 1.4 B**, (Dombeck et al., 2010; Harvey et al., 2009; Hölscher et al., 2005)). Such toroidal projection setups cover a larger portion

of the animal's FOV, yet potentially suffer from lower contrast than stimuli rendered on LCD screens.

1.4.2 Virtual Reality Environments in Neuroscience

The rise of advanced three-dimensional (3D) computer graphics in the late 1980's and early 1990's revolutionized experimental psychology, particularly in the fields of spatial cognition, sensory perception, and social interaction (Loomis et al., 1999). In these VR environments, subjects can interact with objects or other individuals in a simulated environment that could be manipulated in ways that are not restrained by the limits of physical reality. Virtual environments are presented to subjects either by wearing a headset equipped with small computer screens, or by employing small empty room where each surface serves as a projection screen (so-called Cave Automatic Virtual Environments – CAVE, Cruz-Neira et al., 1992). In the latter, subjects are tracked as they move through an experimental space, and their position in the virtual space adjusted accordingly.

In nonhuman behavioral neuroscience, simple VR environments were quickly added to the experimental toolkit. While coupling animal motion and sensory stimuli is not a new concept (Hassenstein and Reichardt, 1956), VR systems occupy a middle ground between classically laboratory experiments and field studies (Thurley, 2022). In awake, head fixed experimental protocols, animals typically are allowed to run on a running wheel, an air-suspended Styrofoam ball, or treadmill to decrease the level of stress experienced (**Figure 1.4 A**). With minimal modification, these apparatuses can be modified as inputs to a VR environment, creating closed-loop systems. For example, coupling the direction and speed of restrained running to the movement or size of a visual stimulus was used to examine optic flow, while the development of simple virtual T-mazes was used to explore spatial coding in the hippocampus (**Figure 1.4 B**, (Dombeck et al., 2010; Harvey et al., 2009; Hölscher et al., 2005)).

Freely moving VR environments for non-human subjects posed challenges that, until recently, were not addressable with existing VR technology. Namely, VR headsets are large, heavy, and designed for subjects with two forward-facing eyes. While some progress has been made towards developing VR headsets for rodents (Isaacson et al., 2023; Pinke et al., 2023), such technology still requires head fixation. The zebrafish neuroscience community has also developed simplified VR paradigms by which

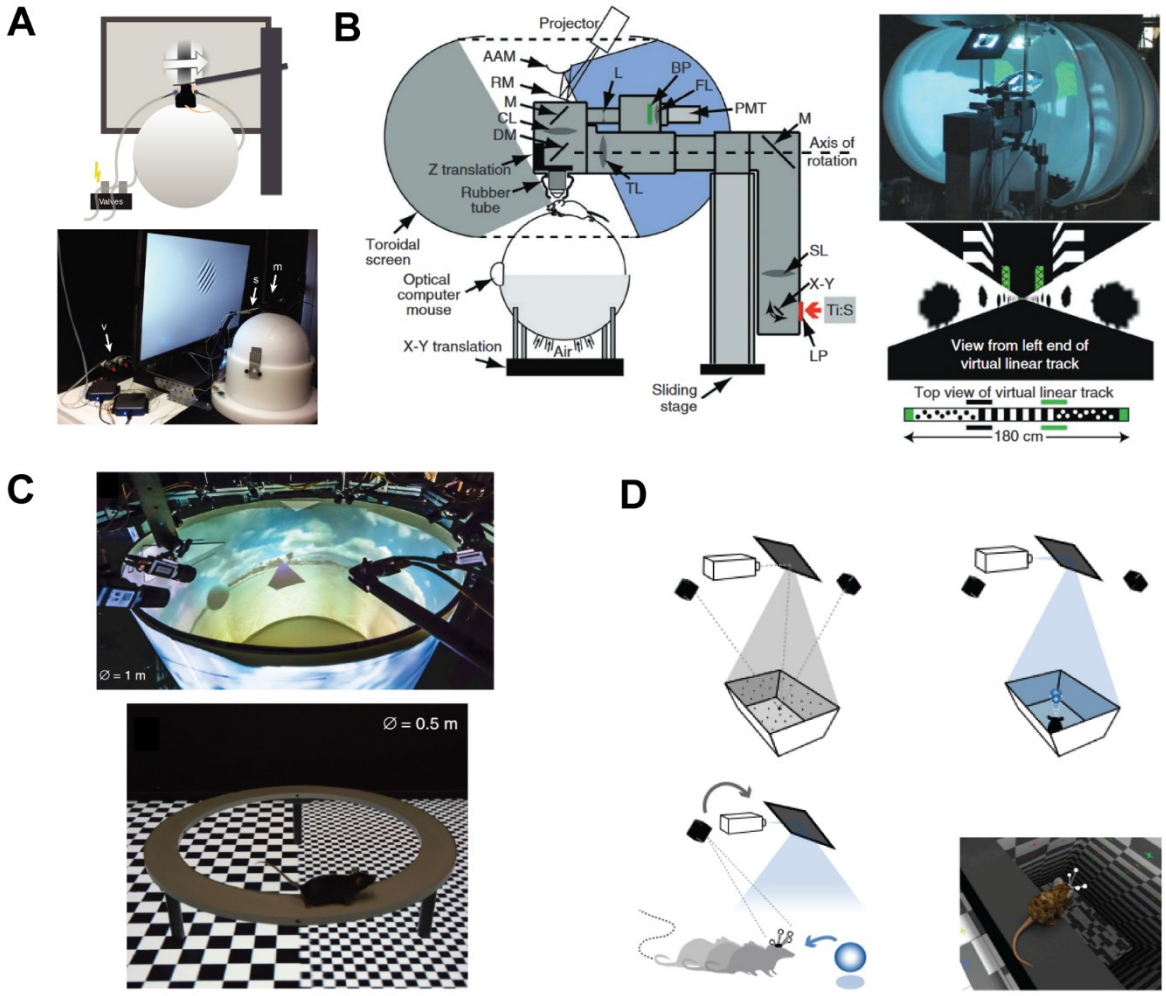

Figure 1.4 Example systems for delivering visual stimulation to head fixed and freely behaving animals | A. Visual stimuli are presented to a head fixed mouse on an LCD screen as the animal walks on an air-suspended Styrofoam ball. Reprinted with permission from Goltstein et al. (2018). **B.** *(Left)* Schematic of the head fixed VR and 2P imaging system described in Harvey et al. (2009) and Dombeck et al. (2010). A head fixed mouse runs on an air-suspended Styrofoam ball. Locomotion is measured by an optical computer mouse. Visual stimuli are rendered in a computer graphics engine and presented via a projector to an angular amplification mirror, which reflects onto a toroidal screen. *(Right)* Photograph of the system and schematic of the virtual corridor. Reproduced with permission from Dombeck et al. (2010). **C.** Images of the VR system presented in Stowers, et al. (2017). Freely moving animals are tracked by an array of cameras, and their position is fed to a computer graphics engine to produce perspective-correct visual stimuli. Reproduced with permission. **D.** Schematic of the ratCAVE system, reproduced with permission from Del Grosso et al. (2017)**.** An array of motion-tracking cameras tracks the position and rotation of a marker fixed to the animal's head. These coordinates are fed to a custom graphics engine that renders perspective-correct visual stimuli. A modified version of the ratCAVE system is used in this study.

zebrafish interact with virtual avatars or virtual prey (Huang et al., 2020; Larsch and Baier, 2018; Štih et al., 2019), however these are either limited to interactions in a two-dimensional space or require immobilizing the animal.

Modified CAVE environments have provided the most fruitful avenue forward for freely moving VR experiments for several species, including zebrafish, fruit flies, and rodents. Two recent projects (Del Grosso et al., 2017; Del Grosso and Sirota, 2019; Stowers et al., 2017) developed immersive 3D virtual environments in which animals can interact with virtual objects, scenes, or avatars. These systems utilize either computer vision or motion capture techniques to track the position of one or more animals with low latency, feeding the position and rotations of the animal(s) to a computer graphics and physics engine to render the visual VR environment from the animal's perspective as they move about the virtual environment (**Figure 1.4 C & D**).

The studies from Del Grosso et al. and Stowers et al. have demonstrated that immersive virtual environments elicit naturalistic behaviors in animals interacting with VR, such as avoiding larger drops in a virtual elevated zero maze or wall avoidance. While these systems represent a major advancement in the tools available for visual stimulation during free behavior, they are not without limitations. While either system can track multiple animals simultaneously, both naturally lack the ability to render perspective-correct visual stimulation for more than one animal at a time. Further, they are at present not optimized for visual stimuli outside the light spectrum visible to humans, and cannot recreate specific properties of natural visual scenes, such as light polarization. Arguably the largest limitation is the inability to render visual stimuli directly above the animal, leaving a portion of the animal's FOV open to the visual scene present in the experimental room. For a commentary on how "real" VR systems are, see Minderer et al. (2016).

In this study, I used a modified version of the ratCAVE environment developed by del Grosso, et al., equipped with the commercial video game development platform Unity3D as a physics and graphics backend (Guggiana Nilo et al., in preparation). This choice was made both from technical consideration, since the ratCAVE system operates with the lowest detection-to-image latency of any published immersive VR system, and out of practicality, as del Grosso and colleagues were close by in the LMU Department of Neurobiology and available for discussion and consultation.

1.5 Study Aims

This thesis addresses two main questions: (1) does tuning to visual orientation and direction remain stable in V1 neurons as a mouse freely behaves, and (2) how do representations of self-motion interact with the representation of visual stimuli in V1 neurons in the mouse? To answer these questions, I first built upon the ratCAVE VR visual stimulation system, making it suitable for use with simultaneous optical recordings in freely moving mice. By recording the activity of V1 neurons to the same visual stimulus set during consecutive freely moving or head fixed sessions on the same experimental day, I examined how representations of visual stimulus features and self-motion interact within single cells and across the neural population.

2 Materials and Methods

2.1 List of Materials

2.1.1 Plasmids

Plasmid	Resistance	Supplier	Reference
pAAV-Syn-SomaGCaMP7	ampicillin	Addgene, 158759	Shemesh et al. (2020)
pAAV-hSyn-FLEX-SomaGCaMP7-WPRE	ampicillin	In house	
pENN.AAV.CamKII 0.4.Cre.SV40	ampicillin	Addgene, 105558	

2.1.2 Viruses

Virus	Titer (GC/ml)	Supplier	Reference
AAVdJ.Syn-SomaGCaMP7	10×10^{12}	VectorBuilder GmbH, (Neu-Isenburg, Germany)	Custom
AAVdJ-hSyn1-FLEX-SomaGCaMP7-WPRE	7.2×10^{12}	VectorBuilder GmbH, (Neu-Isenburg, Germany)	Custom
AAV2/1.CamKII0.4.Cre.SV40	1.15×10^{10}	Uni. Pennsylvania Vector Core (Philadelphia, PA, USA)	James M. Wilson

2.1.3 Antibodies and Staining Solutions

Antibody	Dilution	Supplier
DAPI	1:1000	D3571, Thermo Fisher Scientific
Mouse anti-GFP	1:500	20R-GR011, Fitzgerald Industries
Rabbit anti-somatostatin	1:500	T-4103, BMA Biomedicals
Guinea Pig anti-parvalbumin	1:2000	GP72, Swant
Alexa 488 anti-mouse	1:200	A28175, Thermo Fisher Scientific
Alexa 594 anti-rabbit	1:200	A11012, Thermo Fisher Scientific
Alexa 647 anti-guinea pig	1:200	A21450, Thermo Fisher Scientific

2.1.4 Chemicals and Pharmaceuticals

Name/Description	Supplier
Isopto-Max (eye cream)	Alcon Pharma GmbH (Freiburg, Germany)
70% Ethanol	
Braunol® 7.5 (iodine solution)	B. Braun Melsungen AG (Melsungen, Germany)
Mikrozid® AF (disinfectant)	Schülke & Mayr GmbH (Norderstedt, Germany)
Ultrasound gel	P.S. Dahlhausen & Co. GmbH (Köln, Germany)
Histoacryl (cyanoacrylate glue)	B. Braun Melsungen AG (Melsungen, Germany)
Cyanoacrylate glue	
Paladur (dental cement)	Kulzer GmbH (Hanau, Germany)
Kwik-Sil (silicone adhesive)	World Precision Instruments Germany GmbH (Friedberg, Germany)

Fentanyl	HEXAL AG (Holzkirchen, Germany)
Midazolam	Ratiopharm (Ulm, Germany)
Medetomidine	Vetpharma
Atipamezole	Veyx-Pharma GmbH
Flumazenil	HEXAL AG (Holzkirchen, Germany)
Naloxon	Ratiopharm (Ulm, Germany)
Xylocain® Pumpspray (lidocaine)	AstraZeneca GmbH (Wedel, Germany)
Rimadyl® (carprofen)	Zoetis Deutschland GmbH
D-Mannitol	Sigma-Aldrich Chemie GmbH (Taufkirchen, Germany)
Silk Fibroin	Sigma-Aldrich Chemie GmbH (Taufkirchen, Germany)

2.1.5 Equipment, Instrumentation, and Hardware

Name/Description	Part Number & Supplier
Surgical Equipment	
Hardened Fine Scissors	14090-09, Fine Science Tools GmbH (Heidelberg, Germany)
Scalpel Handle	10007-12, Fine Science Tools GmbH (Heidelberg, Germany)
Scalpel Blades #11	10011-00, Fine Science Tools GmbH (Heidelberg, Germany)
Dumont #5/45 Cover Slip Forceps	11251-33, Fine Science Tools GmbH (Heidelberg, Germany)
Dumont #7 Curved Forceps	11271-30, Fine Science Tools GmbH (Heidelberg, Germany)
Dumont #5 Straight Forceps	11255-20, Fine Science Tools GmbH (Heidelberg, Germany)
Vannas Spring Scissors – 2 mm	15000-04, Fine Science Tools GmbH (Heidelberg, Germany)
Sugi® Sponge Points, triangular	Kettenbach Medical/Questalpha GmbH & Co. KG (Eschenburg, Germany)
Cotton tips, 15 cm	Medical care & serve® (Wurmlingen, Germany)
Homeothermic blanket with rectal probe	Harvard Apparatus (Holliston, MA, USA)
Dry Bead Sterilizer	STERI 350, Simon Keller AG (Burgdorf, Switzerland)
500 µl syringes	Omnican® 50, B. Braun Melsungen AG (Melsungen, Germany)
3 ml syringes	Omnifix®-F, B. Braun Melsungen AG (Melsungen, Germany)
Headbar (46 x 14 mm, aluminum)	MPI-BI machine shop (Martinsried, Germany)
Headbar Holder	MPI-BI machine shop (Martinsried, Germany)
Disposable Biopsy Punch, 2 mm	Kai Europe GmbH (Solingen Germany)/pfm medical AG (Köln, Germany)
Stypro® Haemostypticum	Curasan AG (Kleinostheim, Germany)
GRIN Lens Holder	Custom made
Vacuum Pump	P 7010, ATMOS MedizinTechnik GmbH (Lenzkirch, Germany)
Flaming/Brown Micropipette Puller	P-97, Sutter Instruments Co. (Novato, CA, USA)
Picospritzer® III	INTRACEL (Shepreth, UK)/Parker Hannifin (Hollis, NH, USA)
Hydraulic Micromanipulator	M0102R, NARISHIGE International Ltd. (London, UK)
Borosilicate Glass Capillaries	3.3, Hilgenberg GmbH (Malsfeld, Germany)
Infra-red lamp	Glamox Luxo GmbH (Bremen, Germany)
Heat Plate	Hot Plate A3, Labotect (Göttingen, Germany)
Intrinsic Optical Imaging	
sCMOS camera	Pco.edge 4.2 LT, Excelitas Technologies (Göttingen, Germany)
Fiber-Coupled LED, 530 nm	M530F3, Thorlabs (Dachau, Germany)
Fiber-Coupled LED, 740 nm	M740F2, Thorlabs (Dachau, Germany)

4x/0.28 NA objective	Olympus (Tokyo, Japan)
Miniscope Imaging	
UCLA version 3 Miniscope (Ghosh et al., 2011)	v3.2, LabMaker GmbH (Berlin, Germany)
Wire-free miniscope kit	Open-Ephys (Lisbon, Portugal)
NA 0.52 GRIN lens	64-519, Edmond Optics GmbH (Mainz, Germany)
NA 0.52 GRIN lens	GT-IFRL-180-inf-50-NC, Inscopix (Mountain View, CA, USA)
Virtual Reality Arena	
Wooden Arena	MPI-BI carpentry (Martinsried, Germany)
ORACAL® 631 PVC Film	ORAFOL Europe GmbH (Oranienburg, Germany)
Retroreflective Tape	3M Deutschland GmbH (Seefeld, Germany)
High Speed Color Projector	PROPixx, VPixx Technologies (Saint-Bruno, Quebec, Canada)
Optitrack Prime 17W Cameras	NaturalPoint, Inc. (Corvallies, OR, USA)
USB 3 CMOS Cameras	DCC3240C, Thorlabs (Dachau, Germany)
800 nm Long Pass Filter	FEL0800, Thorlabs (Dachau, Germany)
Lenses	18R0011984/CG603NC51, Navitar (Rochester, NY, USA)
200-1100 nm Photodetector/Amplifier	DCC3240C, Thorlabs (Dachau, Germany)
780 nm Infrared Torch	PDA10A2, Thorlabs (Dachau, Germany)
Rotary Encoder	MA3-A10-125-N, US Digital (Vancouver, WA, USA)
DAQ	BNC-2110, National Instruments (Austin, TX, USA)
Head Tracker	Custom made in-house
Miscellaneous	
3D Printer	Ultimaker 3 Extended, Ultimaker (Utrecht, Netherlands)
Rat Cages and running wheel	GR900, Techniplast (Buguggiate, Italy)
Mouse Treats	1811442, TestDiet (Richmond, IN, USA)

2.1.6 Software

Name	Version(s)	Developer/Reference
Python	3.8, 3.9	https://www.python.org/
Unity3D	2018.2.17f1, 2020.3.11f1	Unity Technologies (San Francisco, CA, USA)
Motive	2.0.0	NaturalPoint, Inc. (Corvallis, OR, USA)
Unity Projection Mapping	N/A	https://github.com/andrewmacquarrie/UnityProjectionMapping
ratCave	1.0	(Del Grosso and Sirota, 2019)
Miniscope SD Card Reader	1.0	https://github.com/daharoni/wire-free-miniscope
MiniAn	1.2.1	(Dong et al., 2022)
CaImAn	1.10.0	(Giovannucci et al., 2019)
DeepLabCut	2.2.3	(Lauer et al., 2022; Mathis et al., 2021, 2018; Nath et al., 2019)
MATLAB	R2016a	The Mathworks (Natick, MA, USA)
MATLAB Psychophysics Toolbox	3	(Brainard, 1997; Kleiner et al., 2007; Pelli, 1997)
IOS Acquisition Software	1.0	(Goltstein et al., 2021)

2.2 Methods

2.2.1 Ethics

All experimental procedures were conducted in compliance with the institutional guidelines of the Max Planck Society (Max-Planck-Gesellschaft) and the Bavarian government (Regierung von Oberbayern).

2.2.2 Animals and Animal Housing

All experiments were conducted with male wildtype C57/Bl6J mice. Mice were kept on a 12-hour reversed light-dark cycle (10:00 - 22:00) with *ad libitum* access to food and water. Animals were co-housed with littermates in standard rat cages (Techniplast, GR900) with maximal four animals per cage and provided with environmental enrichment (running wheels, wooden and plastic blocks and tubes). A total of eight animals were used in this study.

2.2.3 Freely Moving Virtual Reality (VR) System

The VR system used in this study was a modified version of the ratCAVE system presented in (Del Grosso et al., 2017; Del Grosso and Sirota, 2019). The major modification was the replacement of the Python-based 3D graphics engine (Del Grosso and Sirota, 2019) with commercial video game software (Unity 3D, Unity Technologies). See **Methods 2.2.3.4** and (Guggiana Nilo et al., in preparation) for a comprehensive overview.

2.2.3.1 Computing Hardware

A Windows 10 PC equipped with an Intel® Xeon® E5-1650 CPU, 64 GB RAM, and Nvidia® GeForce® GTX 1080Ti graphics card with 11 GB VRAM was used for all VR experiments. Instrumentation triggers were recorded or sent via a National Instruments DAQ (BNC-2110) and processed with custom Python software.

2.2.3.2 VR Arena

The 50 cm x 100 cm VR arena with angled walls (60º, 50 cm tall) was constructed from wood, painted white, and the inner surfaces coated with a matte white PVC lining (ORACAL® 631, Orafol) to reduce reflections from the overhead projector. A high-speed LED color projector (ProPixx, VPixx Technologies) was mounted 2 m above the arena, facing downwards. Projector frame triggers were captured by recording the bit value of the blue channel from the first pixel in the projection. Six wooden spheres covered in retroreflective tape were glued to the top edge of the arena (two on each long edge, one on each short edge) for tracking by the motion capture system.

2.2.3.3 Motion Capture System

The position and rotation of the mouse's head and the VR arena were captured by an array of 12 motion capture cameras (Optitrack Prime 17W, NaturalPoint, Inc.) at 360 frames per second and processed by the commercial motion capture software Motive (version 2.0.0, NaturalPoint, Inc.). The cameras were equipped with an array of 20 NIR LEDs each for illumination and an IR filter for marker detection. To achieve high tracking speeds, the Optitrack system detects IR light reflected by retroreflective markers and uses on-camera image processing to localize the bright points in the captured field of view before transmitting object location, size, and roundness to Motive, where the objects are triangulated to find the 3D position and orientation of a given set of markers. The tracking system was regularly calibrated to achieve a 3D spatial tracking resolution of approximately 100 µm. Two tracking cameras were mounted directly above the arena flanking the projector for top-down image capture, while the remaining 10 cameras were mounted 1 m above the floor of the arena and rotated so their combined FOVs covered the entire arena. In six cameras, the IR filter was removed for 3D modelling of the arena.

To track the head of the mouse during freely moving experiments, a custom head tracker was 3D printed (Ultimaker 3 Extended) and retroreflective tape applied to the ends of each of the four prongs. After calibrating Motive, the tracker was placed into the arena and "rigid bodies" (collection of tracked points with fixed spatial arrangement) were created to represent both the head tracker and the top edge of the arena, respectively. The rigid body representing the head tracker was modified so that

the forward vector in Motive aligned with the forward direction of mouse locomotion. To guarantee the accurate representation of rotations of the mouse head, the pivot point of the head tracker was translated such that it fell approximately between the eyes of the mouse. During head fixed experiments, tracking the mouse head was unnecessary, but to properly orient displayed visual stimuli, wooden spheres covered with retroreflective tape were glued to a custom-made head bar holder mounted above a running wheel. As with the head tracker, a rigid body was created in Motive and modified to match the desired forward vector and pivot point.

2.2.3.4 VR Visual Stimuli

All visual stimuli were created with the commercial video game engine software Unity3D (v2020.3.11f1, Unity Technologies), and experiments and peripheral hardware were controlled by custom Python software. Unity3D was chosen for its compatibility with the Optitrack system, rich development community, and ease of extensibility with peripheral equipment. Unity3D scenes can be modified with C# scripts to control virtual objects within the scene and to interface with peripheral hardware and software. Further, it offers low-level access to customize GPU shaders to render arbitrary visual stimuli. The Unity scene used to render visual stimuli is available at https://gitlab.mpcdf.mpg.de/mpibi/bonhoefferlab/rigs/vr-rig/vr-platform.

2.2.3.4.1 3D Model of the VR Arena

To create an immersive visual environment, it was necessary to accurately model the VR arena within the Unity3D scene. The 3D model was created using a utility function in the ratCAVE package. Briefly, a grid of white circles was projected onto the VR arena surface and was moved around while the projected points were captured by the motion tracking cameras without the IR filter. The captured volume was then saved as a 3D object file representing the internal surface of the VR arena.

The arena model was imported into Unity and all faces of the model aligned using the ProBuilder extension. To correctly orient the arena model with the tracked VR arena, the pivot point of the arena model was modified using ProBuilder to match the pivot point of the VR arena rigid body tracked by Motive.

2.2.3.4.2 Projection Mapping

While scenes developed in Unity3D are three dimensional, the image rendered by the projector is strictly two dimensional. To achieve an immersive 3D effect from a 2D image, it was necessary to map the projection onto the 3D arena and modify it depending on the head motions of the animal. Mapping a 2D projection onto a 3D surface is possible if one has a sufficiently high-quality 3D model of the object on which to project the image, as the vertices of the physical object can be mapped onto the vertices of the 3D model.

Projection mapping was accomplished using the open-source Unity Projection Mapping package (https://github.com/andrewmacquarrie/UnityProjectionMapping) with Unity3D v2018.2.17f1. The previously acquired 3D arena model was imported and modified as before, then seven points on the virtual arena (the four bottom corners and three top corners) were mapped to their corresponding vertices on the physical arena. A projection matrix containing the point mapping was then saved, and later imported at runtime during experiments to warp the projection to match the dimensions of the physical arena.

2.2.3.4.3 Rendering Stimuli from the Mouse Point of View (Cube Mapping)

Cube mapping (Greene, 1986; Nvidia Corporation, 1999) is a computer graphics method for representing the textures and reflections in a 3D scene on the faces of an imaginary cube surrounding an object. To render the visual stimuli from the point of view of the tracked mouse, a custom script was employed to map all objects in the scene to a cube centered on the head tracker position. The cube map was generated dynamically on a frame-by-frame basis and rendered on the inner surface of the virtual arena. When viewed from the perspective of the head tracker, the visual scene appeared as if rendered on a screen directly in front of the tracker, despite the angled walls of the arena.

2.2.3.4.4 3D Drifting Gabor Patches

A sphere model with a radius of 30 cm was centered on the head tracker position and a custom shader was written to generate spherically corrected, drifting sinusoidal stripes with user-adjustable color, spatial frequency (sf), temporal frequency (tf), and

direction. A secondary custom shader was applied to the sphere to create a Gaussian alpha mask with user-defined mask color and width (by default middle gray; subtended visual angle: 60°) centered at 0° azimuth and 0° elevation. The entire sphere was then rotated to 30° elevation from the tracker's horizontal plane to place the center of the Gabor patch within the putative binocular visual field of the mouse (Samonds et al., 2019; Scholl et al., 2013). The position of the Gabor sphere moved with the position of the animal's head, but the rotation was consistently locked to the tracked horizontal plane of the head to maintain a constant position in visual space and drift direction relative to the head.

For all experiments, 10 repetitions of 12 grating directions (evenly spaced between ±180°; black and white; tf: 2 cycles/s, sf: 0.04 cycles/º) were presented for 5 seconds with a 6 second inter-trial interval.

2.2.3.4.5 Latency Tests

Closed-loop system latency (from marker position detection to stimulus rendering) was tested by affixing a head tracker to a running PC cooling fan and projecting a black dot on the arena floor next to the tracked position. The position of both the head tracker and the projected dot were captured with a single tracking camera. The difference in distance between the marker and projected dot on each frame was measured to determine system latency, as this difference translates directly into time knowing the frame rate of the camera.

2.2.3.4.6 Peripheral Equipment

To capture overhead video for pose estimation during freely moving experiments, a CMOS camera (DCC3240C, Thorlabs) with an 800 nm long pass filter (FEL0800, Thorlabs) was mounted 2 m above the arena, and recorded video at 30 frames per second. During head fixed experiments, an identical camera setup was used to record eye movements from the right eye. The eye was illuminated by a 780 nm IR torch (M780L3, Thorlabs). To track the running activity of the head fixed mouse, a plastic running wheel was mounted on a rotary encoder (MA3-A10-125-N, US Digital), and the output voltage signal converted to rotational distance and running speed in software post-hoc.

2.2.4 Molecular Cloning, Virus Preparation, and Viral Strategy

The GECI SomaGCaMP7 (Shemesh et al., 2020) was delivered *in-vivo* either by injection with glass capillary needles or via silk fibroin film mixtures deposited onto the surface of the implanted gradient refractive index (GRIN) lens (Jackman et al., 2018). SomaGCaMP7f acted as a functional reporter of neural activity. The localization of GCaMP7f to the soma was desired to avoid excessive diffuse background fluorescence from dendrites and axons in the imaging volume.

The following plasmid was designed by Drago Guggiana Nilo and Claudia Huber and then cloned in-house by Claudia Huber using standard molecular biology protocols:

pAAV-hSyn-FLEX-SomaGCaMP7-WPRE

Backbone: pAAV-hSyn1-FLEX-mRuby2-GSG-P2A-GC6s-WPRE

Insert: pAAV-Syn-SomaGCaMP7 (Addgene #158759)

This plasmid as well as pAAV-Syn-SomaGCaMP7 were packed into AAVs by VectorBuilder, Inc. with the following serotypes, pseudotypes, and titers:

1. AAVdJ-hSyn1-FLEX-SomaGCaMP7-WPRE; titer 5.85 x 10^{13} gc/ml
2. AAVdJ.Syn-SomaGCaMP7; titer 6.26 x 10^{13} gc/ml

Two viral strategies were used to transduce V1 cells with SomaGCaMP7 – one to localize somaGCaMP expression to excitatory neurons, and a second to target all neuronal subtypes. To induce sparse expression of SomaGCaMP7 in excitatory neurons, a mixture of AAV2/1.CamKII0.4.Cre.SV40 (University of Pennsylvania, Lot CS1128) and AAVdJ-hSyn1-FLEX-SomaGCaMP7-WPRE was used. AAV2/1.CamKII0.4.Cre.SV40 was diluted with PBS to a final concentration of 1.15 x 10^{10} gc/ml, and AAVdJ-hSyn1-FLEX-SomaGCaMP7-WPRE was diluted to a final concentration of 7.2 x 10^{12} gc/ml. Here, AAV2/1.CamKII0.4.Cre.SV40 transfected excitatory cells under the CamKII promotor to express Cre, while AAVdJ-hSyn1-FLEX-SomaGCaMP7-WPRE transfected all neural subtypes. To express SomaGCaMP7f across all neuronal subtypes, AAVdJ.Syn-SomaGCaMP7 was diluted with PBS to a final concentration of 10 x 10^{12} gc/ml.

2.2.4.1 Preparation of Capillary Needles

Prior to surgery, borosilicate glass capillaries were pulled on a pipette puller to form a sharp tip. Tips were clipped using forceps under a stereoscopic microscope to achieve an outer diameter of approximately 30 µm and beveled to 60º under positive internal pressure on a custom beveling device made from a diamond-dust coated hard disk. Tip sharpness, diameter, and beveling quality were assessed under a standard transmission light microscope. Needles were front filled under negative internal pressure with the AAV2/1.CamKII0.4.Cre.SV40 and pAAV-hSyn-FLEX-SomaGCaMP7-WPRE mixture, and stored at 4 ºC until use.

2.2.4.2 Preparation of Silk-Fibroin Film Coated GRIN Lenses

Lenses were prepared following a previously described protocol (Jackman et al., 2018). The day prior to surgery, 1.8 mm diameter x 4.31 mm long GRIN lenses were sterilized in 70% EtOH and cleaned with lens tissue, then mounted in a petri dish using modelling clay. Silk fibroin (Sigma Aldrich, 5154) was mixed 1:1 with the final dilution of AAVdJ.Syn-SomaGCaMP7. A total of 1.5 ml of the silk fibroin-virus mixture was pipetted onto the surface of each GRIN lens in 300-500 µl drops, taking care to restrict the spread of the mixture to the center of the lens and avoid the formation of bubbles. Lenses were air dried at room temperature for 1 hour, then transferred to a vacuum chamber and vacuum desiccated at 4 ºC overnight. Coated lenses were stored at 4 ºC until use.

2.2.5 *In-Vivo* Transduction of GECIs and GRIN Lens Implantation

GRIN lenses were implanted over the right hemisphere of binocular visual cortex in mature C57/Bl6J mice (age 8-10 weeks at time of surgery). Mice were anesthetized by intraperitoneal (i.p) injection of a mixture of 0.05 mg/kg Fentanyl, 5 mg/kg Midazolam, and 0.5 mg/kg Medetomidine (henceforth FMM). Analgesia was supported by a subcutaneous (s.c.) injection of carprofen (Rimadyl, 4 mg/kg) immediately before the start of surgery. Body temperature was maintained at 38 ºC using a heating pad, and eye cream (Isopto-Max) applied to the corneas to protect the eyes. Hair on the scalp was removed with an electric hair trimmer, and the scalp disinfected with alternating applications of 70% EtOH and iodine solution (Braunol® 7.5).

Mice were mounted in a stereotactic apparatus, a 10% lidocaine solution (Xylocain®) applied to the scalp, and a rostro-caudal incision was made with scissors from between the ears to the height of the eyes. Skin was removed to the right of the midline, and the skull cleared of hairs and connective tissue with cotton tips. The skin margins were secured with Histoacryl, and the surface of the skull was roughened with a scalpel blade around the area of the craniotomy. A rectangular aluminum head bar (chamber type, 46 x 14 mm, custom made) was secured to the skull with cyanoacrylate glue and fixed with dental cement, with care taken not to cover the target craniotomy site.

To determine the location of binocular V1, mice were removed from the stereotaxic device and transferred to an intrinsic optical signal (IOS) imaging setup, and the acquired response profile and vascular pattern were used to functionally determine the target craniotomy location (see **Methods 2.2.5.1**). After IOS imaging, the animal was returned to the stereotaxic apparatus in the surgery room. A subcutaneous injection of a 15% D-mannitol solution (10 µl/g body weight) was given just before the craniotomy to minimize brain swelling. A circular craniotomy was made over binocular V1 with a 2 mm biopsy punch, and the dura carefully removed with a syringe and iris scissors.

If delivering virus with capillary needles, virus was injected at four sites spaced approximately 200 µm apart with a volume of 120 nl per injection. Following virus injection, a GRIN lens was fixed in a custom micromanipulator apparatus, centered above the craniotomy, and lowered until the lens sat flush to the cortical surface. The lens was then slowly lowered another 200-300 µm and secured with cyanoacrylate glue. If using a silk-fibroin film coated GRIN lens instead of injections, the same procedure was used to implant the lens. Dental cement was applied to further fix the GRIN lens and head bar, and to cover any exposed areas of the skull. A silicone polymer (Kwik-Sil) was applied to encapsulate the GRIN lens, and a thin layer of dental cement was then applied over the silicone to prevent ingestion or damage by cage-mates. Anesthesia was reversed by intraperitoneal injection of a mixture of 2.5 mg/kg Atipamezole (Veyx-Pharma GmbH), 0.5 mg/kg Flumazenil (B. Braun Melsungen AG), and 1.2 mg/kg Naloxone (Ratiopharm) (henceforth AFN).

Immediately after surgery, mice were kept under a heating lamp and under observation. Mice recovered overnight in the home cage (separated from non-surgerized cage mates by an acrylic barrier), where floor temperature was maintained at 37 ºC with a heat plate. Carprofen was administered subcutaneously for at least three days after the procedure for analgesia.

2.2.5.1 Intrinsic Optical Signal Imaging

IOS imaging (Bonhoeffer and Grinvald, 1991; Bonhoeffer and Hübener, 2016) was used to localize binocular V1 in all experiments. Mice were fixed under the microscope and the optical axis aligned with the chamber of the head bar. An image of the blood vessel pattern was first acquired by illuminating the exposed section of the skull with a 530 nm LED and used as a landmark reference for the subsequent craniotomy. For IOS imaging, the exposed skull was evenly illuminated from both sides with two 740 nm LEDs, and the imaging plane set to 400-450 um below skull surface. Intrinsic signals were identified as a decrease in reflected light caused by cortical activation following visual stimulation. Images were collected with a 4x air objective (NA 0.28, Nikon) using a sCMOS camera. Images were collected at 15 Hz with 3 x 3 px spatial binning and 3 frame temporal averaging. Acquired signals were bandpass filtered from 400-700 nm. Custom MATLAB scripts were used for image acquisition and signal analysis.

2.2.5.1.1 Visual Stimulation During IOS Imaging

Visual stimuli (spherically corrected drifting square wave gratings, eight directions, sf: 0.04 cycles/°, tf: 2 cycles/°) (Jaepel et al., 2017; Rose et al., 2016) were generated using the MATLAB Psychophysics toolbox (Brainard, 1997; Kleiner et al., 2007; Pelli, 1997) and presented on a gamma-corrected LCD computer monitor centered on the visual field of the mouse. The monitor was rotated to match the head tilt of the mouse and positioned 16 cm in front of the mouse.

2.2.6 Miniscope Baseplate Implantation

Miniscope baseplates were implanted three to four weeks following GRIN lens and head plate implantation. Mice were anesthetized by i.p. injection of FMM and body temperature maintained at 37 ºC using a heating pad. Mice were placed into a custom-made fixation apparatus, and eye cream applied to the eyes to prevent injury from dental cement debris. The dental cement and silicone cap covering the GRIN lens were carefully removed, and the surface of the GRIN lens cleaned with 70% EtOH and lens tissue. Excess dental cement surrounding the base of the GRIN lens was carefully removed with a dental drill. The head bar was then cleaned of any debris with 70% EtOH and cotton tips.

The aluminum miniscope baseplate was affixed to a UCLA V3 miniscope (Ghosh et al., 2011), and the miniscope was then attached to a micromanipulator with a custom 3D-printed miniscope holder. A suitable region of interest displaying somaGCaMP7-expressing neurons was located after lowering the miniscope above the GRIN lens. Once satisfied with the region of interest, the baseplate was secured to the head bar with cyanoacrylate glue, the miniscope removed, and the baseplate further secured with dental cement. The final imaging plane was determined by placing a wire-free miniscope into the micromanipulator and finding a focal plane displaying the most in-focus neurons by adjusting the miniscope focus tube. Once satisfied with the imaging plane, the focus set screw was tightened, and the final position of the focus tube recorded. A lens cap was placed to protect the GRIN lens from damage in the home cage. Mice were awakened by an intraperitoneal injection of AFN and allowed to recover in a separate cage for one hour before returning to the home cage.

2.2.7 Animal Habituation

Two weeks after head bar and GRIN lens implantation, or upon reaching a body weight of 28 grams, mice were habituated to the experimenter, the experimental room and setup, and the miniscope for one week. For the first three days, mice were only habituated to the experimenter and the setup in two sessions. On the first day, mice were carefully held in the experimenter’s hands and allowed to walk from hand to hand for one minute, repeated twice. On the second day, handling occurred the same as the previous day, and acclimation to head fixation was introduced by briefly grabbing

the edges of the head bar while the mouse was allowed to walk on a flat running wheel. On the third day, acclimation remained the same, but the duration of the head fixation period was increased to 30 seconds. During the second session on days 1-3, mice explored the virtual reality arena with a small number of treats (TestDiet, 1811442) for 10 minutes.

On days 4-7, mice were further habituated to head restraint by being fixed in a custom head bar holder and running on a flat running wheel. Fixation times increased from 1 minute to 10 minutes in three-minute steps on each day.

Days 4-6 also introduced acclimation to the miniscope and tracker. Since the wirefree miniscope, head tracker, and head bar combined weigh 6.45 g, gradual acclimation was necessary. Mice were acclimated to the weight by affixing custom 3D printed weights to each side of the head bar (total mass: 3 g, 4.8 g, 9.7 g) and allowing the mice to run around the VR arena for two sessions lasting up to 15 minutes. Mice were kept under constant observation during the acclimation period. Acclimation was ended early if mice displayed signs of distress or if body weight reduced. The second session on day 6 introduced the wirefree miniscope without a battery (5.30 g), on the final day, the wirefree miniscope with battery was used. If mice struggled with the weight of the miniscope on day 7, acclimation was continued until the mouse could carry the miniscope for 15 minutes.

2.2.8 Miniscope Imaging

A 5.8 g miniaturized fluorescence microscope (UCLA version 3 miniscope) equipped with a wirefree modification system and 3.7 V, 45 mAh battery was used (Ghosh et al., 2011). An integrated 470 nm LED light source excited neurons transfected with somaGCaMP7f. Emitted green light passed through a 535/50 nm bandpass filter and was focused onto an integrated CMOS image sensor (838 x 640 px, cropped and down sampled to 320 x 320 px). A 1.8 mm diameter GRIN lens with NA 0.52 (Edmond Optics 64-519) was used as the objective lens and acquired fields of view of approximately 450 x 450 µm. Images were acquired at 20 frames per second and saved to an on-board SD card. Miniscope imaging was synchronized with visual stimuli and head tracking information by detecting the initial LED emission with an amplified photodetector (Thorlabs, PDA10A2) and then aligning frame timestamps extracted

from the acquired frames with a custom Python script. Imaging parameter modification and data saving were done through the Miniscope SD Card Reader package (https://github.com/daharoni/wire-free-miniscope).

Mice underwent two imaging sessions every day for at least 10 experimental days. During one session, mice were head fixed on a running wheel while receiving visual stimulation. During the second session, mice were allowed to freely move about the arena while presented with visual stimuli. During freely moving sessions, the mice were provided with water and a small number of treats. The order of head fixed and freely moving sessions was reversed on each experimental day. Sessions lasted approximately 23 minutes each, although variability in battery capacity shortened some sessions.

To further explore the effect of visual stimuli and luminance in V1 neurons, mice underwent experiments where the VR arena was illuminated but no visual stimulus was shown, or the arena was fully darkened with no visual stimulus. To control for state-dependent effects on neural activity, a subset of mice underwent experiments where they received visual stimulation during consecutive head fixed and consecutive freely moving sessions.

2.2.9 Perfusions and Immunohistochemistry

At the end of the experimental protocol, all animals were sacrificed by transcardial perfusion. Mice were anesthetized with an intraperitoneal injection of 1.5x the normal dose of FMM. After approximately 20 minutes, the toe pinch pain reflex was tested on all paws to ensure deep anesthesia had been reached. Mice were then fixed to a perfusion stage and transcardially perfused first with 15 ml of a PBS solution containing lidocaine (0.1%) and heparin (0.1%) followed by 20 ml of a 4% paraformaldehyde (PFA) solution. Brains were removed from the skull and stored in a 4% PFA solution at 4°C until slicing.

Brains were sliced into 300 µm thick coronal sections with a microtome (Thermo Fischer Scientific) and washed three times for twenty minutes in PBS. Slices were permeabilized (PBS with 2% Triton X-100) at 4°C on a shaker. The next morning, slices were transferred to room temperature blocking buffer (PBS containing 10% goat

serum, 2% Triton X-100, 0.2% sodium azide) for eight hours. After removal from blocking buffer, slices were incubated overnight in antibody buffer (PBS containing 1% goat serum, 0.2% triton X-100, 0.2% sodium azide) with primary antibodies (1:1000 DAPI, 1:500 mouse anti-GFP, Fitzgerald, 1:500 rabbit anti-somatostatin, BMA, 1:2000 guinea pig anti-parvalbumin, Swant) at room temperature, then transferred to a shaker where incubation continued at 4°C for two days. Slices were then washed on a shaker at 4°C overnight in washing buffer (PBS with 3% NaCl, 0.2% Triton X-100), transferred to the secondary antibody solution (antibody buffer with 1:200 Alexa 488 anti-mouse, 1:200 Alexa 594 anti-rabbit, and 1:200 Alexa 647 anti-guinea pig) and incubated on a shaker for two days at 4 °C. Slices were again washed on a shaker overnight in 4°C washing buffer. The following morning, slices were washed three times for twenty minutes in PBS. Finally, the slices were cleared by incubation in 350 µl RapiClear 1.47, then mounted on spacer slides for fluorescence and confocal microscopy.

2.2.10 Data Analysis

All data were analyzed with custom Python scripts. Code is available at https://gitlab.mpcdf.mpg.de/mpibi/bonhoefferlab/analysis_code/prey_capture.

2.2.10.1 Miniscope Source Extraction

Miniscope data were registered and source extracted using the MiniAn pipeline (Dong et al., 2022). The MiniAn pipeline is composed of five steps: (1) preprocessing, (2) motion correction, (3) initializing seeds for potential neurons, and (4-5) iterative spatial footprint identification and temporal signal extraction.

During the preprocessing step, vignetting (bright center and dark edges) is reduced and an estimate of the background (out of focus fluorescence and tissue autofluorescence) is created. The background estimate is created via a process of morphological erosion, whereby bright features smaller than a particular window (15px, or roughly the size of a neural soma in the FOV) are removed to estimate the background. This is followed by a morphological dilation, where the maximum value of the 15 px window is used to fill the window (Lu et al., 2018). Together, these steps remove any bright features in the image smaller than the window size, leaving only putative cell bodies.

In the motion correction step, the stack is registered through an iterative cycle of template matching on subsets of frames within the imaging stack. The subsets exponentially increase in size until the whole stack is registered at once.

In the final steps, MiniAn uses the constrained nonnegative matrix factorization (CNMF) algorithm for source extraction (Giovannucci et al., 2019; Pnevmatikakis et al., 2016). The CNMF algorithm modeled cellular activity in the input video as the product of spatial and temporal matrices with additional contributions from background and random noise, defined as:

$$\boldsymbol{Y = AC + B + E} \quad \textbf{(2.1)}$$

where Y is the input image stack, A is the cellular spatial footprint matrix, C is the cellular temporal activity matrix, B is the spatiotemporal fluctuation of the background fluorescence, and E is a noise term. This is carried out in iterative spatial and temporal update steps as explained below.

The CNMF algorithm requires initial estimates of the locations of potential neurons and their activity. MiniAn generates these estimates, or seeds, by iteratively finding the local maxima of maximum intensity projections computed on subsets of frames in the imaging stack. This produces an over-complete set of seeds, which are then refined by keeping seeds that have a significantly high peak-to-noise ratio in their temporal trace and pass a Kolmogorov–Smirnov test. Seeds are merged if they are sufficiently close together and their temporal traces are sufficiently correlated, resulting in a single seed per putative cell. Initial spatial and temporal matrices are estimated from these seeds, which represent initial spatial footprints of putative cells and their temporal traces. The spatial footprint and temporal trace of the background are also calculated, as they are needed in the next steps.

During the spatial update, the absolute difference between the input stack at a given pixel, the spatial matrix (across all putative cells) and the background contribution are calculated per pixel and minimized. A sparseness term offsets contribution from noise. The spatial footprint matrix and the background footprint matrix are then updated. In the temporal update step, the temporal activity of each spatial footprint is calculated, and contributions from neighboring overlapping footprints subtracted. Spiking “activity” is then inferred from the calcium traces using an autoregressive process, and the

temporal matrix is updated. The spatial and temporal updates are then repeated. Finally, putative cells that are spatially close together and have temporal traces that are correlated above a certain threshold (e.g. 0.85) are merged. The final output contains terms for the spatial footprints of identified cells, their inferred spiking activity, and their fluorescence activity.

2.2.10.2 Cell Matching

Single neurons were matched between consecutive imaging sessions on the same day within animals using the cell matching function `register_multisession` from the open-source toolbox CaImAn (Giovannucci et al., 2019). Cell spatial footprints extracted from each recording were first filtered based on size and circularity to eliminate putative non-neuronal footprints extracted by MiniAn. The remaining footprints and maximum fluorescence projections from each imaging stack were given as inputs to `register_multisession`. The function aligns the maximum projections to estimate an affine transform, which is applied to each footprint before matching. Then an intersection over union metric and the Hungarian algorithm for optimal matching are used to find putative footprint matches. Footprints were considered matched if the centroids of putative matches were separated by less than 8 pixels (roughly the radius of a cell in the imaging setup used).

2.2.10.3 Pose Estimation and Eye Tracking

During freely moving experiments, nine points were tracked offline on each mouse using DeepLabCut (version 2.2.3) (Lauer et al., 2022; Mathis et al., 2021, 2018; Nath et al., 2019). The snout, left and right sides of the head bar, top and base of the miniscope, three points along the spine, and the tail base were labeled, as well as the corners of the VR arena. During head fixed experiments, a separate DeepLabCut network was trained to label eight points along the edge of the pupil, the reflection of the IR LED illumination source, the corners of the eye, and a single point on the upper and lower margins of the eyelid.

For each network, 10 frames taken from 10 videos were labelled, with 95% of the frames used for training. An EfficientNet-b0 based neural network was used, with an imgaug augmenter for two training iterations validated with three shuffles. For the

freely moving network, the test error was: 2.12 pixels, train: 0.98 px (image size 1280 px x 1024 px), with a p-cutoff of 0.85. For the eye tracking network, the test error was: 2.39 px, train: 0.83 pixels for 1280 px x 1024 px images, with a p-cutoff of 0.6.

2.2.10.4 Analysis of Visual Stimulus Responses

Unless otherwise stated, neural activity was defined as the area under the curve (AUC) of the deconvolved fluorescence trace for the stated time window.

2.2.10.4.1 Visual Stimulus Responsivity

Neurons were considered responsive to visual stimuli if their activity during visual stimulus trials was greater than the activity during the preceding 5 seconds of the inter-trial interval period as determined using a 1-sided Mann-Whitney U test ($p < 0.25$). This p-value was determined by manual inspection of deconvolved fluorescence traces (**Supp. Figure 1**).

2.2.10.4.2 Preferred Direction and Orientation and Tuning Curve Fits

Direction tuning curves were calculated as the mean activity across trials for each presented direction stimulus. For direction tuning curves, a double von Mises function (circular double Gaussian) was least-squares fitted to the mean direction response tuning curve. The preferred direction (PD) was defined as the peak of the fitted tuning curve. Orientation tuning curves were calculated by wrapping the responses in direction space [0°, 360°) onto the [0°, 180°] domain, and taking the mean activity for each orientation shown. Preferred orientation (PO) was calculated by least-squares fitting a von Mises function to the mean orientation response tuning curve and finding the corresponding peak.

2.2.10.4.3 Direction and Orientation Selectivity

Preferred direction was calculated by finding the presented direction corresponding to the peak of the double von Mises fit. Single neurons were considered direction selective if they were determined to be visually responsive (see **Methods 2.2.10.4.1**) and had a direction selectivity index (DSI) ≥ 0.5, defined as:

$$DSI = 1 - \frac{R(\theta_{null})}{R(\theta_{pref})} \quad \textbf{(2.2)}$$

where θ_{pref} was the preferred direction, $\theta_{null} = \theta_{pref} + 180°$, and $R(\theta)$ was the mean response to stimulus θ (Lien and Scanziani, 2018).

Single neurons were counted as orientation selective if they were determined to be visually responsive and had an orientation selectivity index (OSI) ≥ 0.5, defined as:

$$OSI = \frac{R(\theta_{pref}) - R(\theta_{null})}{R(\theta_{pref}) + R(\theta_{null})} \quad \textbf{(2.3)}$$

where θ_{pref} was the preferred orientation, θ_{null} was the mean of the responses to orientations orthogonal to θ_{pref}:

$$\theta_{null} = \text{mean}(\theta_{pref} \pm 90°) \quad \textbf{(2.4)}$$

and $R(\theta)$ was the mean response to stimulus θ (Zhao et al., 2013).

2.2.10.5 Locomotion Modulation

The effect of locomotion on neural activity was determined by calculating the difference in mean neural activity per cell during running and still periods within experiments. Running periods were identified by fitting a Gaussian mixture model with two components to the running wheel speed or locomotion speed trace of each experiment. Cells were considered modulated by running activity if the difference in running-dependent activity fell outside of the 95% confidence interval of the distribution of all running-dependent activity differences across all cells.

2.2.10.6 Self-Motion Tuning Curve Calculation

To determine if a given cell carried information related to one of the measured self-motion variables, a method to create a tuning curve analogous to classical visual tuning curves was desired. However, since the measured self-motion variables occurred continuously, computing trial-average tuning for a given stimulus was not possible. The following approach approximated the responses of cells with the magnitude of the measured self-motion variable. The inferred spike activity for each cell below the 8th percentile was set to zero. Then the range of each self-motion

variable was split into 20 bins. The self-motion tuning curve was calculated by finding the mean inferred spike activity within each of the range bins.

Responsivity, quality, and consistency scores were calculated for each tuning curve. The responsivity of the cell to the variable of interest was calculated as the mutual information score of the tuning curve (Stefanini et al., 2020), defined as:

$$SI = \sum_{i=1}^{N} p_i \frac{r_i}{r} \log_2 \frac{r_i}{r} \quad \textbf{(2.5)}$$

where i indexes the range bins, p_i is the probability of occupancy (number of occurrences) for a given bin, r_i is the mean inferred spike rate (the tuning curve) for bin i, and r is the overall mean inferred spike rate for the cell.

Tuning curve quality was calculated as the Spearman's R between the real inferred spike activity and reconstructed neural activity predicted by the tuning curve. A consecutive temporal 70-30 train-test split was applied to the activity of each cell (r_{train} and r_{test}) and the self-mot ion trace of interest (a_{train} and a_{test}). A tuning curve was calculated as above for the training set. A predicted neural activity trace (r_{pred}) was created by first binning a_{test} according to the range bins calculated for a_{train}, and assigning the training set tuning curve value corresponding to the assigned range bin for each timepoint in a_{test}.

$$\rho_{\mathrm{R}(r_{test}),\mathrm{R}(r_{pred})} = \frac{\mathrm{cov}\left(\mathrm{R}(r_{test}), \mathrm{R}(r_{pred})\right)}{\sigma_{\mathrm{R}(r_{test})}\sigma_{\mathrm{R}(r_{pred})}} \quad \textbf{(2.6)}$$

Tuning curve consistency was calculated by first splitting the self-motion trace into two temporal halves, calculating the self-motion tuning curve as above for each half, then finding the correlation coefficient matrix R between the two:

$$R_{1,2} = \frac{C_{1,2}}{\sqrt{C_{2,2}C_{2,2}}} \quad \textbf{(2.7)}$$

where C is the covariance matrix. The consistency score was defined as the value of the correlation matrix at the initial time lag.

Cells were considered responsive or to have sufficient quality if their respective responsivity and quality values exceeded the 95th percentile of a bootstrapped distribution and were considered consistent if their consistency score was nonzero and

exceeded the 70th percentile of a bootstrapped distribution. Cells were considered tuned to a particular self-motion variable if they met criteria for both responsivity and quality.

2.2.10.6.1 Bootstrapping

To preserve short time-scale correlations in the bootstrapped distributions of responsivity, quality, and consistency, self-motion traces were temporally binned, and the bins shuffled 100 times. Bin size was determined by splitting the self-motion traces across all experiments into 10 s windows and finding their autocorrelation. The initial zero crossing of the mean window autocorrelation was taken as the bin length for bootstrap shuffling.

2.2.10.7 UMAP Embedding

To visualize the tuning index vector for each cell, the UMAP (Uniform Manifold Approximation and Projection) method (McInnes et al., 2020) was used to embed the high-dimensional tuning index vector into 2-dimensional space. For cells re-identified between consecutive sessions, the tuning vector comprised the quality index of each self-motion variable recorded for both sessions, and the DSI and OSI values recorded from both sessions. For cells not re-identified between consecutive sessions, the tuning vector comprised the quality index to each self-motion variable from the relevant experiment, and the DSI and OSI values. The tuning vectors were then formed into a matrix and processed with UMAP to produce the plots in the thesis.

2.2.10.8 Statistics

Results are reported as mean ± standard deviation (std). All statistics on circular data were conducted with the PyCircStat toolbox (Berens, 2009). The consistency in OSI or DSI between repeated or consecutive sessions (**Figure 3.12** and **Supp. Figure 3**) was reported at the Pearson's correlation, and differences in means were evaluated with a Kruskal-Wallis test. For assessing changes in PO or PD (**Figure 3.13** and **Supp. Figure 4**), consistency values are reported as the circular correlation using the, which is equivalent to the Pearson's R for circular data:

$$R = \frac{\sin(x - \bar{x})\sin(y - \bar{y})}{\sqrt{\sum \sin(x - \bar{x})^2 \sum \sin(y - \bar{y})^2}} \quad \textbf{(2.8)}$$

where *x* and *y* are the POs or PDs in the two sessions, and $\bar{x}$ and $\bar{y}$ are the mean POs or PDs. For testing differences in the means of PO or PD, the Watson-Williams test (the circular equivalent to a T-test or one-way ANOVA) was used.

To test for significance in fractions of cells per experiment tuned to visual or self-motion variables across animals and days, Kruskal-Wallis tests followed by Dunn post-hoc tests with Bonferroni correction for multiple comparisons were used. When comparing distributions with uneven sample sizes (as in **Figure 3.8** and **Figure 3.15**), distributions were bootstrapped 1000 times. P-values of the bootstrapped distributions are reported as the upper bound of the 95% confidence interval of the post-hoc corrected, bootstrapped p-values.

3 Results

3.1 Establishment of a Freely Moving VR Visual Stimulation Paradigm

To study the interplay between the representations of visual stimuli and self-motion in V1 cells, it was necessary to develop a visual stimulation paradigm that delivered tight control over the spatial and temporal dynamics of a visual scene delivered to a freely moving mouse. To consistently present the visual stimulus within the mouse's visual field, this paradigm required the ability to track the position of the mouse at high spatial and temporal resolutions and to generate the visual stimulus with minimal latency. To fulfill these criteria, I used a modified version the ratCAVE immersive virtual reality paradigm (Del Grosso and Sirota, 2019) in which the position of the mouse's head was tracked by an array of motion capture cameras and visual stimuli were created in a physics engine (Guggiana Nilo et al., in preparation). The visual stimulus was centered on the tracked position of the mouse's head, and cube-mapped onto the walls of a virtual arena object, which matched the dimensions of the real arena. The cube-mapping step allowed for the visual scene, designed in the physics engine as a 3D space, to be "perspective correct" from the mouse's point of view when projected onto the VR arena with angled walls (**Figure 3.1 A** and **Methods**). For position tracking, mice were equipped with a custom 3D printed, four-pronged head tracker and tracked with commercial motion capture software (**Figure 3.1 B**). A spatial resolution of 10 µm at a temporal resolution of 360 frames per second (FPS) was achieved, and the closed-loop latency from position detection to stimulus projection was measured at 18 ms **(Methods 2.2.3.4.5**), allowing for stimulus presentation at frame rates of up to 55 FPS (Guggiana Nilo et al., in preparation).

To probe the effect of self-motion on the representation of direction and orientation in V1, I created a VR analog to the classical two-dimensional Gabor stimulus (Granlund, 1978). I rendered drifting sinusoidal black and white stripes (spatial frequency 0.04 cycles/ º, temporal frequency 2 Hz) on a virtual sphere (30 cm radius) centered on the tracked position of the mouse's head. A Gaussian alpha mask was overlaid on the stripes to limit the grating stimulus to a circle subtending 60º of visual angle. The entire "Gabor sphere" was then rotated and fixed at 30º elevation and 0º azimuth from the

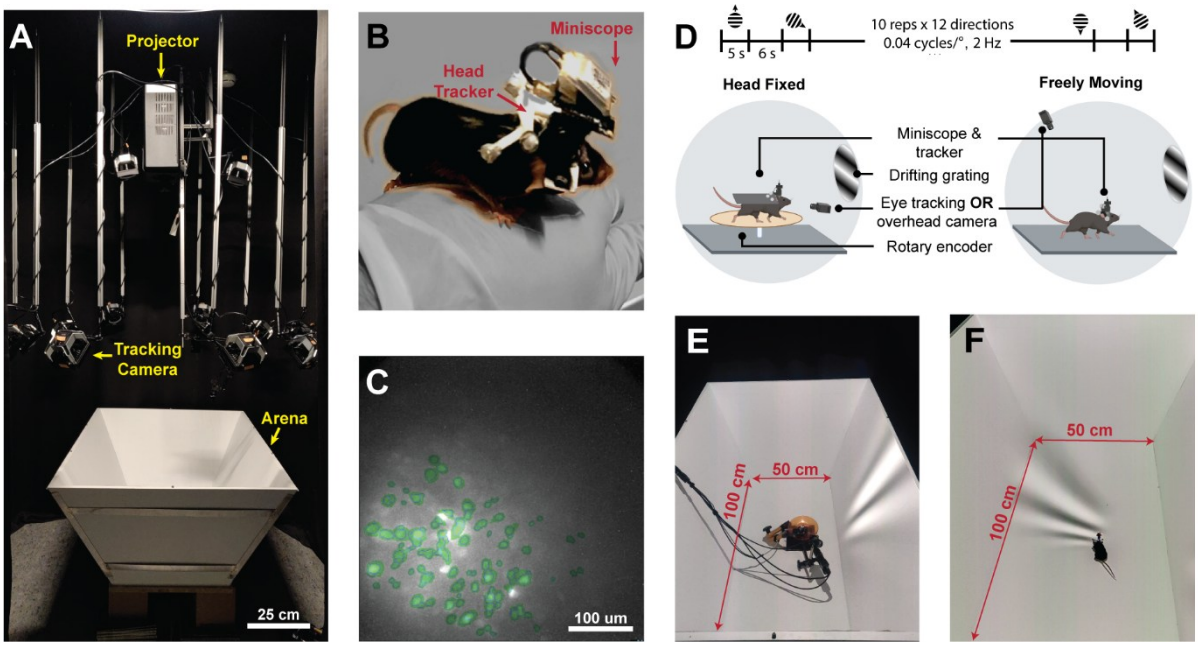

Figure 3.1 Immersive VR system and wire free miniscope imaging in freely moving VR | A. The virtual reality arena, tracking cameras and projector. **B.** A mouse equipped for a freely moving experiment with the UCLA V3 wire free miniscope and custom head tracker. **C.** Maximum projection image from an example FOV. Green shading: probability map of neuronal ROI spatial footprints found by CNMF. **D.** Schematic of experimental trial structure and visual stimulus parameters. **E.** Image from a head fixed experiment. The mouse is head fixed on a running wheel while the right eye is recorded by a CMOS camera. Red lines: internal arena dimensions. Note that the distortion of the grating is due to the photo position and angle differing from the head tracker. **F.** Same as **E**, but from a freely moving experiment.

horizontal plane of the tracked mouse head to align the center of the visual stimulus with the binocular visual field. As the mouse moved about the arena, the position and rotation of the Gabor sphere were locked with the position and rotation of the mouse's head, maintaining the presentation of the stimulus at the same position in the visual field regardless of animal motion. For visual stimulation, twelve evenly spaced directions in the range [-180º, 180º] were presented in 5 s trials for 10 repetitions with a 6 s inter-trial interval (**Figure 3.1 D**). The trial number was limited to 120 trials by the 45 mAh miniscope battery, which could deliver adequate current to the excitation LED for approximately 25 minutes.

The activity of V1 neurons was recorded from the right hemisphere of eight adult male C57Bl6/J mice using the UCLA V3 miniscope (Ghosh et al., 2011) with the wireless attachment. Using a 0.52 NA GRIN lens, I gained optical access to a 450 x 450 µm FOV in superficial layer 2/3 of V1. To limit out-of-focus fluorescence from passing axons and dendrites, I employed the GECI somaGCaMP7 to restrict the virally

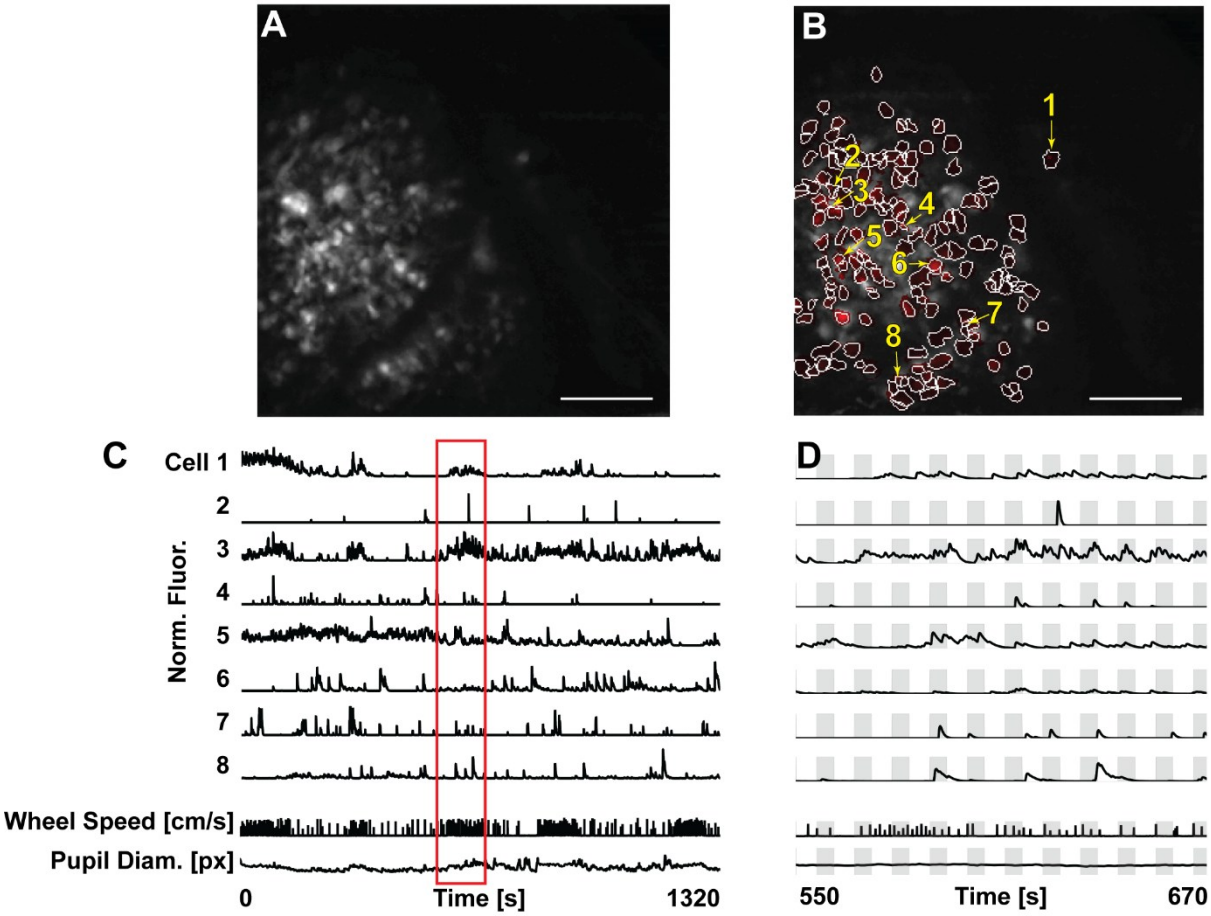

Figure 3.2 Example head fixed experiment ethogram and FOV | A. Maximum projection of the recorded FOV from an example head fixed experiment. Scale bar = 100 µm. **B.** Same FOV as **A.** Red shaded areas are regions of interest corresponding to ROIs detected by MiniAn. **C.** Normalized deconvolved fluorescence traces from 8 cells and all recorded self-motion or postural variables. **D.** Enlarged view of the fluorescence traces and ethogram highlighted by the red box in **C.** Gray boxes are visual stimulus trials.

mediated expression of GCaMP to cell bodies. To limit the expression of GCaMP to the area immediately below the GRIN lens imaging surface and to optimize for recording in-focus cellular activity, I mixed the GCaMP virus dilution with silk fibroin to form a biocompatible film (Jackman et al., 2018). This film was applied to the surface of the GRIN lens touching the brain, and transduced cells primarily in layer 2/3, but in some cases labelling extended to layer 5 (see **Methods 2.2.4.2**). On each experimental day, mice were imaged in one head fixed and one freely moving session. The order of head fixed and freely moving experiments was reversed on subsequent days to minimize systematic effects of the experimental order. During head fixed

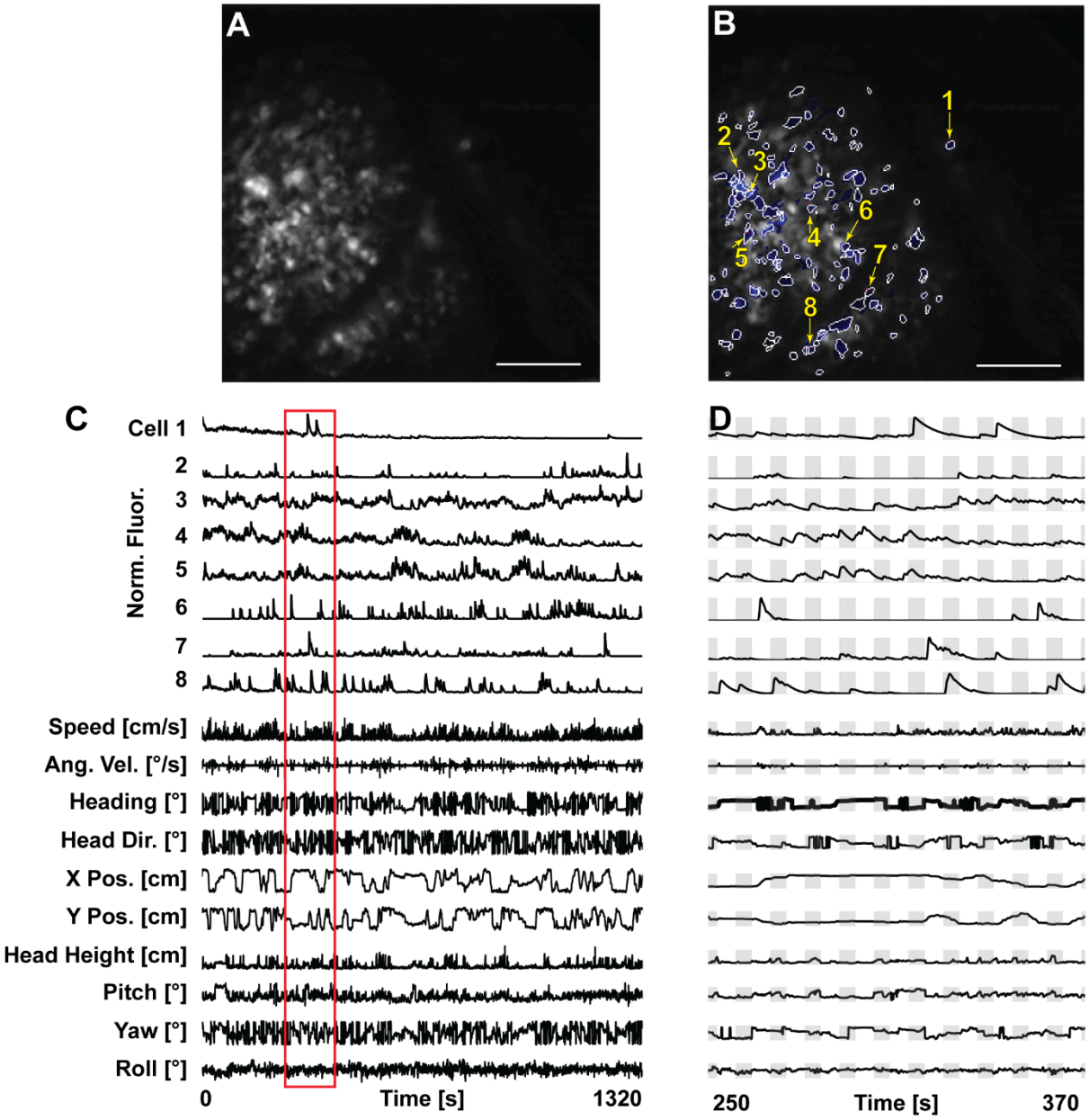

Figure 3.3 Example freely moving experiment ethogram and FOV | A. Maximum projection of the recorded FOV from an example freely moving experiment. Scale bar = 100 µm. **B.** Same FOV as **A.** Blue shaded areas are regions of interest corresponding to ROIs detected by MiniAn. **C.** Normalized deconvolved fluorescence traces from 8 cells and all recorded self-motion or postural variables. **D.** Enlarged view of the fluorescence traces and ethogram highlighted by the red box in **C.** Gray boxes are visual stimulus trials.

experiments, I recorded neuronal activity with the miniscope, as well as the velocity of the running wheel via a rotary encoder and the ipsilateral eye with an IR camera (**Figure 3.1 D, E** and **Figure 3.2**). I post-hoc calculated the position and diameter of the pupil using DeepLabCut. During freely moving experiments, I similarly recorded neuronal responses with the miniscope. I additionally measured twelve self-motion or postural variables by aligning head position and rotation data collected from the head

tracker with estimated pose measurements derived from DeepLabCut tracking of the mouse with an overhead camera. These included the position and rotations of the head about all three axes, the head direction relative to the body, heading direction, and linear and angular velocity (**Figure 3.1 D, F** and **Figure 3.3 A**). Overall, cells responded to both visual stimuli (**Figure 3.3 B**, upper) and postural and self-motion variables (**Figure 3.3 B**, lower).

3.2 Responses to Visual Stimuli and Running Onset

In both head fixed and freely moving experiments, I observed neural responses during the presentation of visual stimuli (**Figure 3.4 A**, cells 6, 8 and **Figure 3.4 B**, cells 2, 8), during the offset of visual stimuli (**Figure 3.4 A**, cells 2, 4) and cells that exhibited responses that were not clearly locked to the visual stimulus. Several factors could explain the observed stimulus offset responses. Some offset responses may be caused by the release of inhibition due to the presentation of a non-preferred stimulus in the neuron's RF. Since receptive field mapping was not conducted, the visual stimulus presentation location may have fallen outside the classical RFs of these neurons and suppressed their activity. Alternatively, the release of contrast-dependent suppression from the surround may have driven the offset responses.

Running and quiescent periods were detected by fitting a Gaussian Mixture Model with two components to either the running wheel speed trace or mouse locomotion speed trace for each experiment (**Figure 3.5 A, B**, upper). While single running bouts occasionally evoked responses, cells did not show consistent responses to running onset.

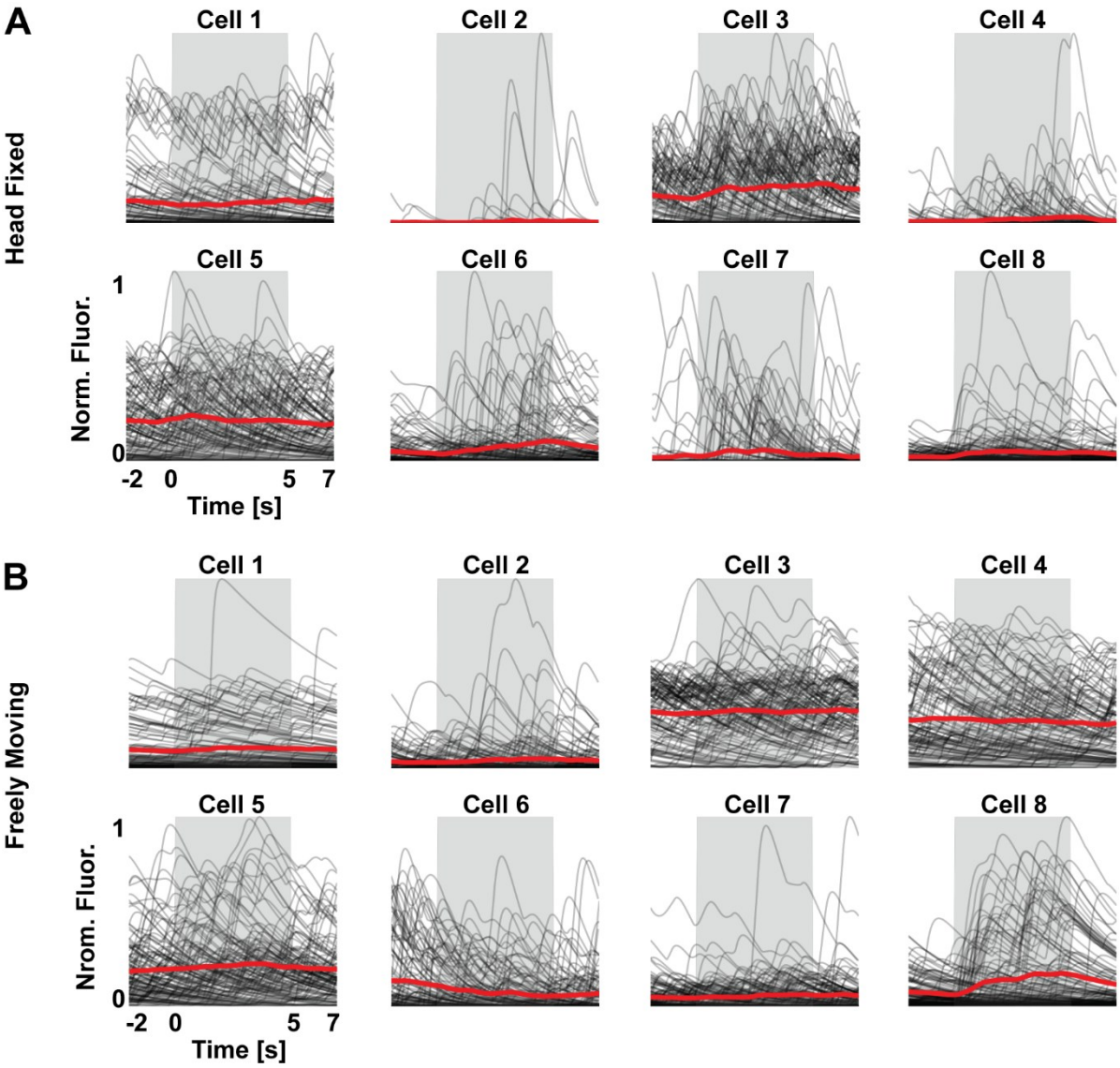

Figure 3.4 Neurons display visually evoked responses to drifting grating Gabor stimuli in VR | A. Visually evoked deconvolved fluorescence responses to all visual stimuli from eight cells from an example head fixed experiment. Black lines – single trial responses, red line – trial average response, gray shaded area – visual stimulus trial. Cells are the same as in **Figure 3.2**. **B.** Responses of the same cells in **A** in a subsequent freely moving experiment. Cells are the same as in **Figure 3.3**. Note that cells shown here were re-identified between head fixed and freely moving sessions (see **Supp. Figure 5**). 120 visual stimulus trials were presented, with 10 trials for each of 12 directions.

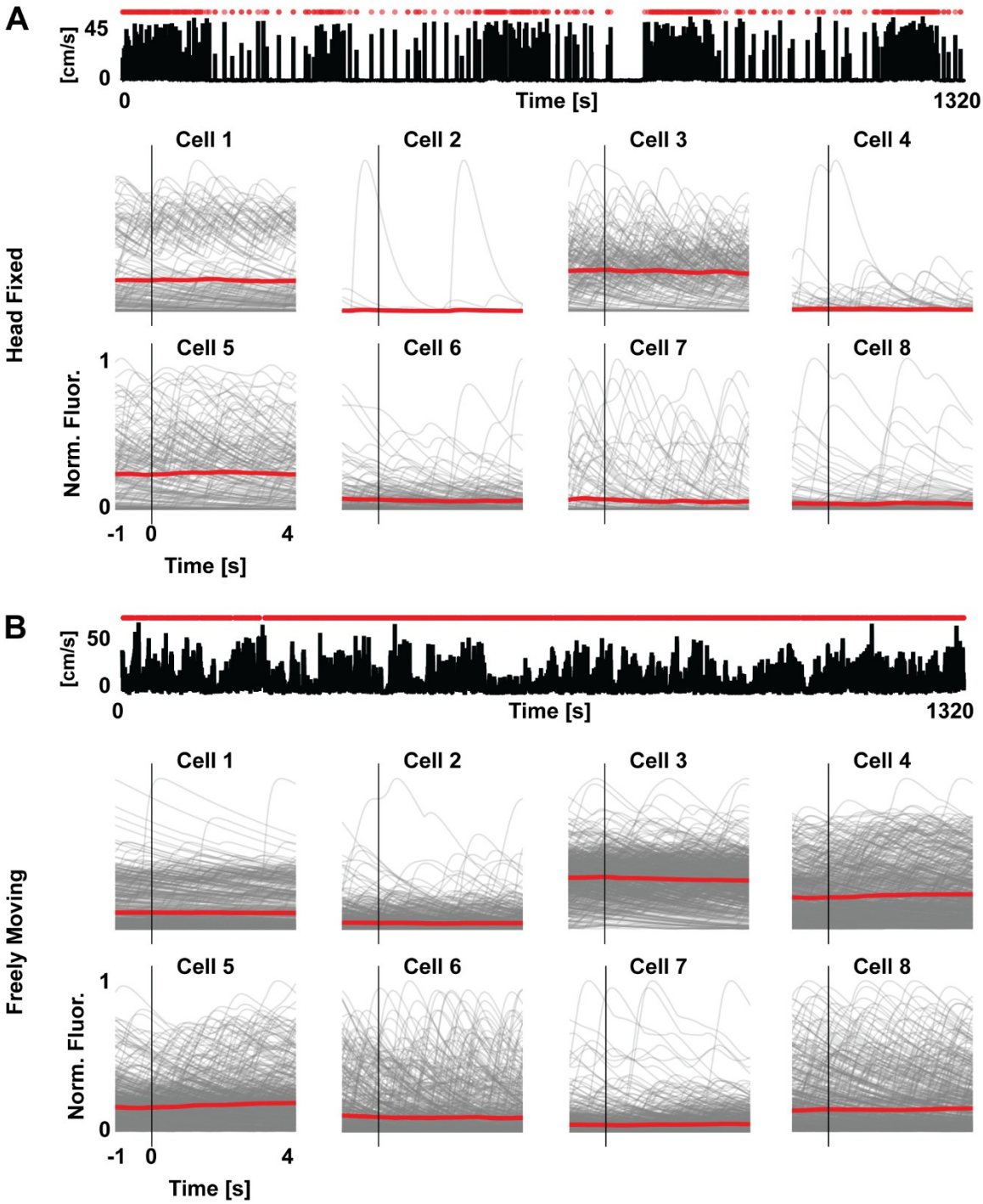

Figure 3.5 V1 neurons do not exhibit responses consistently locked to locomotion onset | A. (Upper) Running wheel speed during an example experiment. Red dots are running bouts as fit by a Gaussian Mixture Model with two components. (Lower) Running evoked fluorescence responses from eight cells from an example head fixed experiment. Vertical black line – running onset, gray lines – single trial responses, red line – trial average response. Cells are the same as in **Figure 3.2. B.** Responses of the same cells as in **A** in a subsequent freely moving experiment. Cells are the same as in **Figure 3.3.**

3.3 Visual Responsivity, Orientation and Direction Tuning

I next evaluated the direction and orientation tuning of recorded cells with methods commonly used in the visual neuroscience literature – namely the responsivity of cells and their orientation and direction selectivity indices (Lien and Scanziani, 2018; Wörgötter and Eysel, 1987; Zhao et al., 2013). Cells were considered visually responsive if their activity during visual stimulus trials was greater than that during the inter-trial intervals (see **Methods 2.2.10.4.1**). Cells were considered significantly orientation or direction tuned if they were classified as visually responsive and their orientation or direction selectivity indices (OSI, DSI, ranging between 0 and 1) were greater than 0.5.

3.3.1 Visual Responsivity is Similar Between Head Fixed and Freely Moving Sessions

As expected, V1 cells exhibited a variety of tunings to the VR Gabor sphere stimulus presented during head fixed experiments (**Figure 3.6**). Some cells exhibited clear orientation (**Figure 3.6 B**, cells 3-5) or direction preference (cells 1 and 2), while others exhibited broad responsivity to visual stimuli (cells 6-8).

As with head fixed experiments, I also observed a variety of responses to the orientation and direction of grating stimuli during freely moving sessions, including strong orientation or direction tuning, as well as cells with poor visual responsivity (**Figure 3.7**, cells re-identified from **Figure 3.6**).

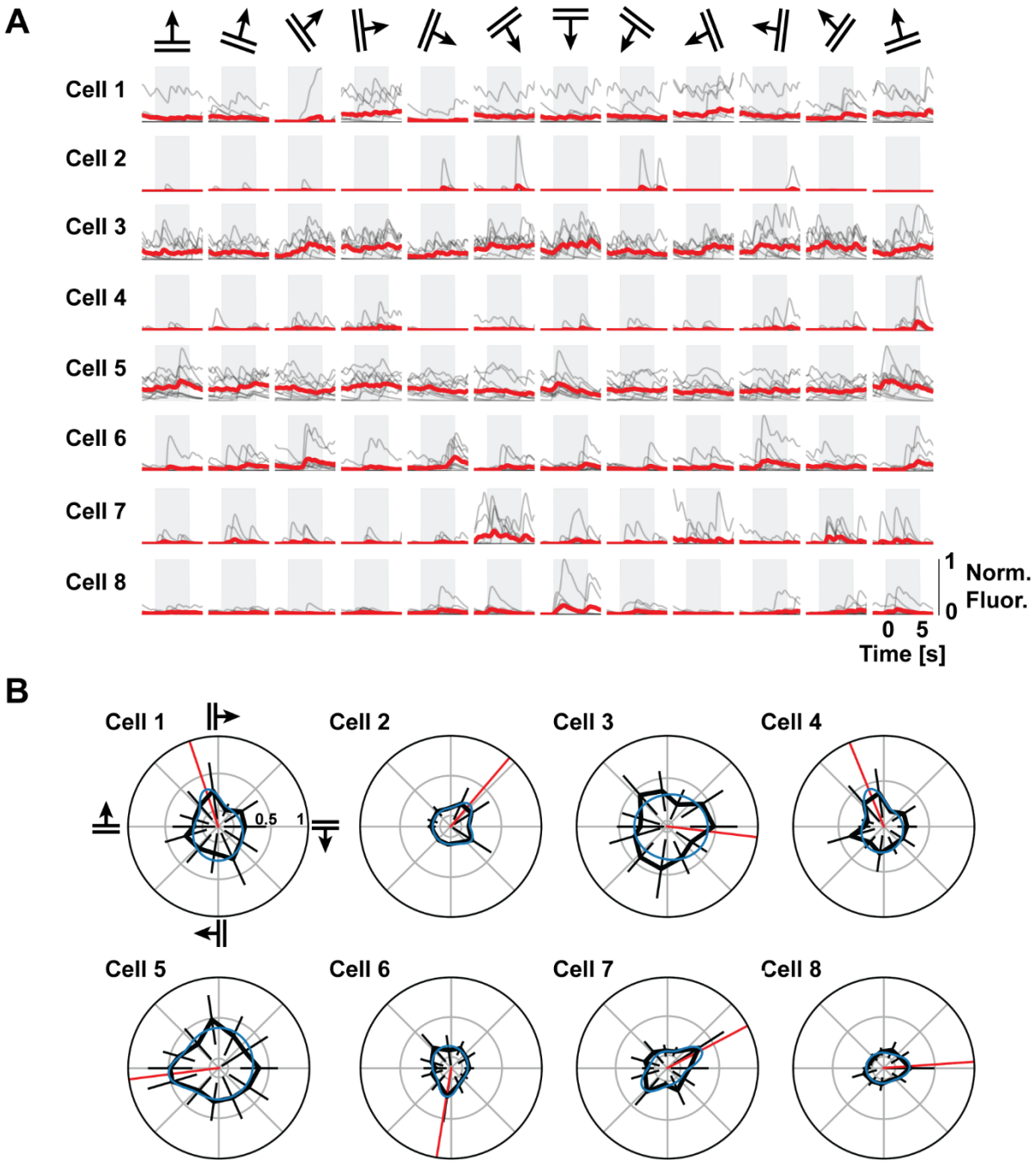

Figure 3.6 Example orientation and direction tuning curves during a head fixed experiment | A. (Upper) Deconvolved fluorescence traces from eight example cells by grating direction. Black lines – single trial responses, red line – trial average response, gray box – visual stimulus trial. Cells are the same as in **Figure 3.2**. **B.** Polar direction tuning plots for the cells in **A**. Black line – mean area under the curve (AUC) across trials ± std, blue line – double Von Mises function fit to the mean, red line – preferred direction.

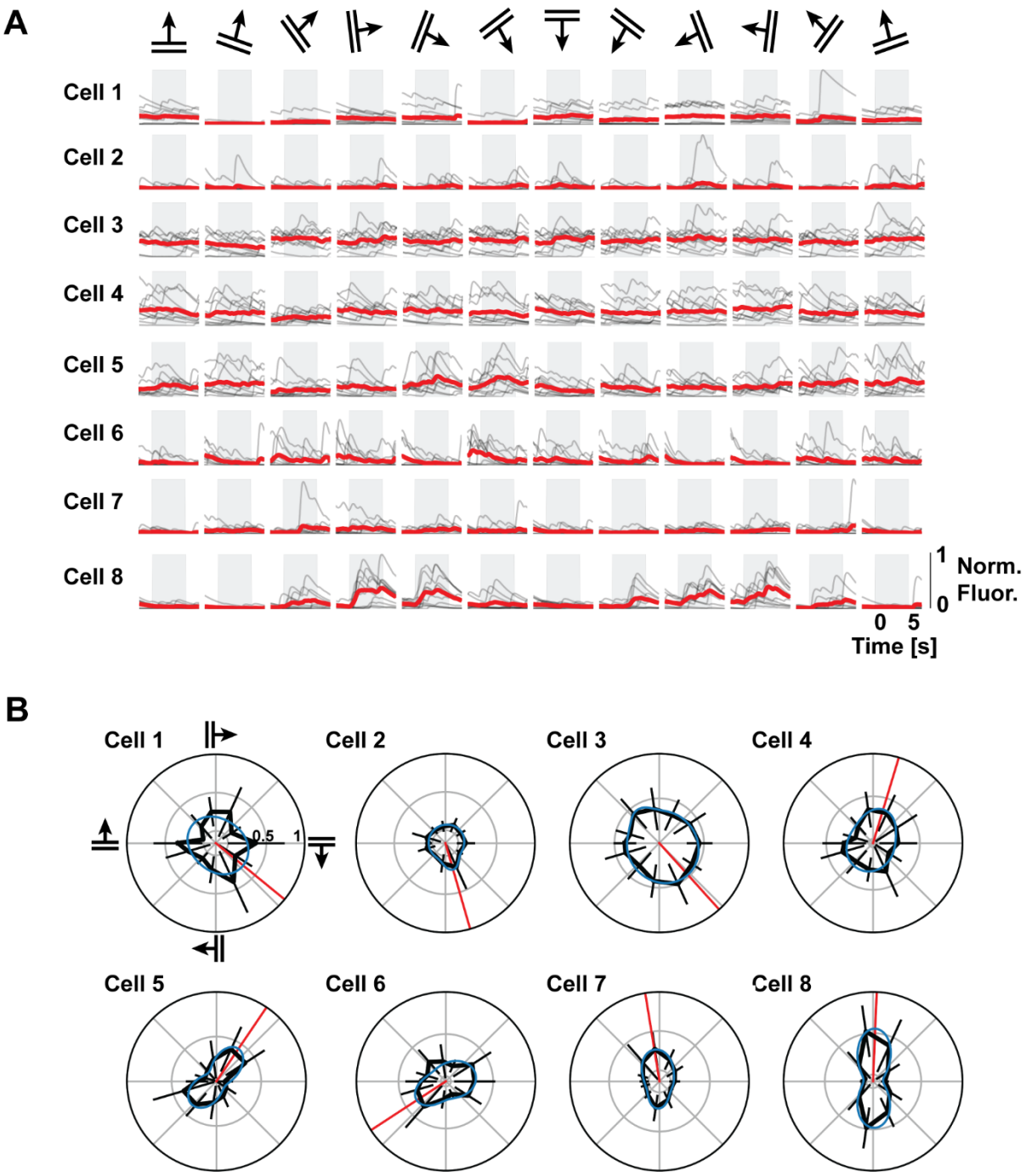

Figure 3.7 Example orientation and direction tuning curves during a freely moving experiment | A. (Upper) Deconvolved fluorescence traces from eight example cells by grating direction. Black lines – single trial responses, red line – trial average response, gray box – visual stimulus trial. Cells are the same as in **Figure 3.3**. **B.** Polar direction tuning plots for the cells in **A**. Black line – mean AUC across trials ± std, blue line – double Von Mises function fit to the mean, red line – preferred direction.

The fraction of visually responsive cells per experiment was similar between head fixed and freely moving sessions (mean = 27.8 ± 20.1% and 27.3 ± 23.1%, respectively; **Figure 3.8** and **Table 1**); however, the fraction of cells tuned to visual stimulus orientation or direction was significantly greater in head fixed experiments (**Table 1**), with around 10% of cells classified as orientation selective (mean = 9.4 ± 9.1%). In comparison, less than 5% were orientation selective during freely moving experiments (mean = 4.4 ± 11.2%, statistics: **Table 1**). The fraction of cells that were direction tuned was also significantly different between sessions, at 9% and 6%

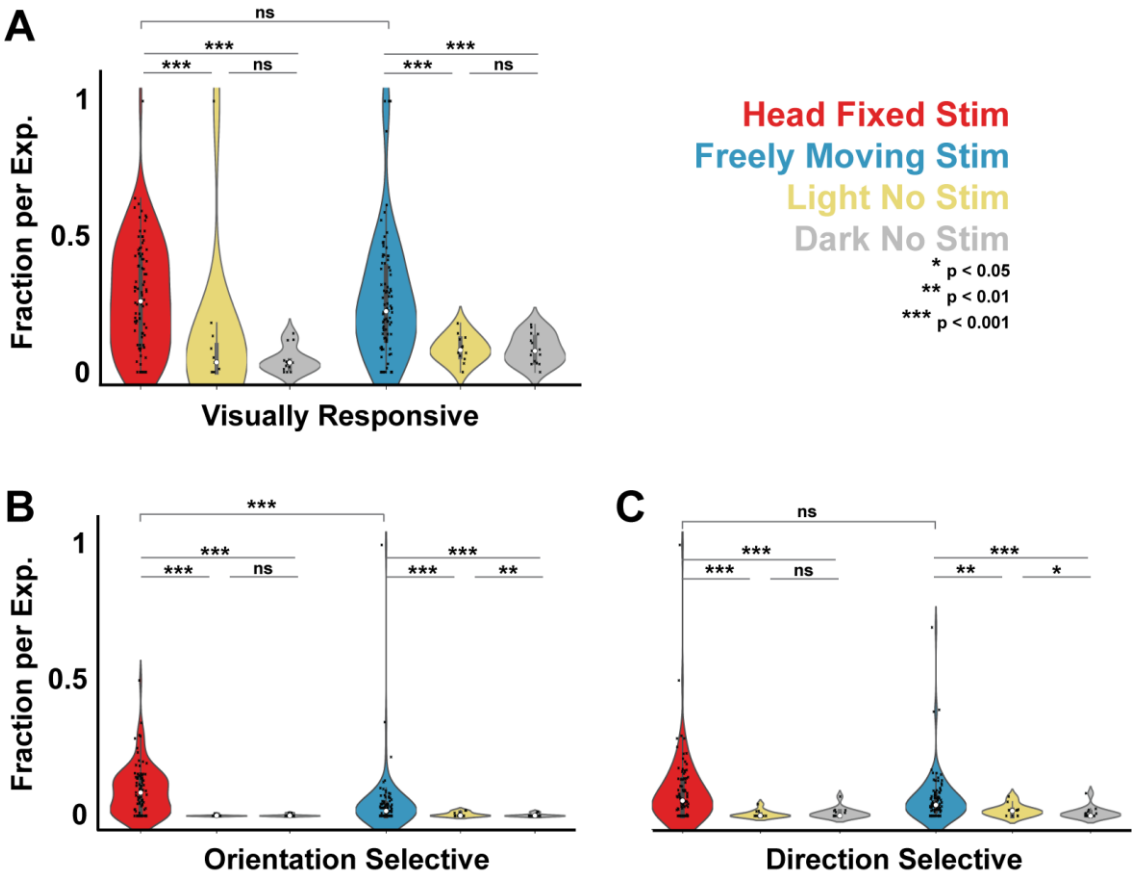

Figure 3.8 Orientation and direction tuned neurons are more prevalent in head fixed configurations | A. Distributions of fraction of cells per experiment that were visually responsive, White circles – median, black dots – single experiments. Yellow - distributions from head fixed or freely moving control experiments where the VR arena was illuminated but without visual stimuli. Gray – control experiments conducted in the dark. Cells were considered visually responsive if the AUC of the deconvolved fluorescence trace during visual trials was statistically greater than the preceding 5 seconds of inter-trial interval (Mann-Whitney U test, $p < 0.25$). Control experiments without the visual stimuli were conducted to evaluate the likelihood of a cell being considered visually responsive, orientation selective, or direction selective in the presence of the trial structure but absence of visual input. **B** and **C.** Distributions of fraction of cells per experiment that were considered orientation or direction selective, respectively. Statistics: Kruskal-Wallis tests and Dunn post-hoc test with Bonferroni correction for multiple comparisons. As the number of experiments differed between the main experiment and control experiments, all statistics were bootstrapped ***continued…***

1000-fold. Reported statistics are the upper bound of the 95% CI of the bootstrapped, post-hoc corrected p-value distributions. n = 92, 12, and 15 experiments across 8 mice for main experiment, illuminated control, and dark control, respectively.

respectively (head fixed mean = 9.1% ± 13.0%, freely moving mean = 6.4 ± 9.4%, statistics: **Table 1**). The fraction of orientation or direction tuned cells reported here is lower than expected from previous literature and will be discussed later (see **Discussion 4.2**). It is important to note that these data are reported as fraction of cells per experiment. As longitudinal cell matching within mice was not done, all cells were treated independently, and many are likely repeatedly represented in the dataset.

3.3.2 V1 Neurons Exhibit Orientation and Direction Selectivity in Freely Moving VR

To test if the V1 neuronal activity I observed during visual stimulus experiments was indeed being driven by the visual stimulus, I ran a series of control experiments. These experiments were identical to the primary experiment, except that there was no visual stimulus (VR Gabor) present. These control experiments were conducted either in the VR arena under illumination conditions identical to the main experiments or in complete darkness. To assess the likelihood of my metric for considering a cell to be visually responsive due to spontaneous or self-motion-related activity and then assigning orientation or direction tuning, these experiments maintained a trial structure identical to the main experiment, as orientation and direction tuning curves and indices rely on trial-averaged activity. I observed significantly fewer visually responsive cells during all control sessions, with less than half the fraction of cells identified as visually responsive, and less than 1% of cells classified as orientation or direction selective (**Figure 3.8** and **Table 1**). No significant difference was observed in the fraction of visually responsive cells between illumination conditions in control experiments under head restraint (illuminated mean = 12.8 ± 28.1%, dark mean = 4.4 ± 4.6%, statistics: **Table 1**) or during free behavior (illuminated mean = 8.7 ± 5.0%, dark mean = 8.5 ± 5.4%, statistics: **Table 1**). During control experiments in the head fixed configuration, there was no significant difference between the fraction of cells identified as orientation or direction tuned between illumination conditions (illuminated vs. dark: orientation selective means: 0.1 ± 0.3% vs. 0.1 ± 04%, direction selective means: 0.6 ± 1.3% vs. 1.1 ± 1.9%), indicating that the VR Gabor stimulus was needed to elicit strong

responses to stimulus orientation or direction. Interestingly, there was a slight but significantly greater fraction of cells that were classified as orientation or direction tuned during illuminated, freely moving control experiments compared to those conducted in darkness (orientation selective means: 0.6 ± 0.8% vs. 0.3 ± 0.5%, direction selective means: 2.0 ± 2.2% vs. 1.2 ± 2.2%). This may indicate that V1 activity may by chance be classified as orientation or direction selective even without a visual stimulus in the presence of a trial structure due in part to the structure of the visual scene above the VR arena.

3.4 Comparison of Visual Tuning Curves and Properties Between Consecutive Sessions

Having established that the VR Gabor sphere stimulus indeed drives responses in V1 during head fixation and free behavior, I sought to compare the orientation and direction tuning of cells re-identified between imaging sessions conducted on the same day. One would expect that the visual tuning properties of neurons imaged in consecutive sessions of the same type (either head fixed or freely moving) would be similar. To test this, I further conducted a series of control experiments in which animals underwent either repeated head fixed or repeated freely moving imaging sessions and then manually re-identified a subset of neurons between consecutive imaging sessions on the same day. These experiments were conducted back-to-back, with approximately 10 minutes between sessions, identical to experiments with consecutive freely moving and head fixed experiments. Neuronal footprints were matched between sessions using CaImAn (Giovannucci et al., 2019) and then a subset manually evaluated to minimize false matches. Considering only cells that were classified as visually responsive during both experimental sessions on the same day, I evaluated the consistency of the OSI and DSI, as well as the preferred orientation (PO) and preferred direction (PD) of these cells. Comparing the PO and PD of cells considered orientation or direction tuned during only one of the two sessions may seem counterproductive, as the PO or PD of an untuned cell is random. It is important to note, however, that the OSI or DSI cutoffs for considering a cell to be orientation or direction tuned are somewhat arbitrary. I use a cutoff value of 0.5, while others have used lower values (e.g. OSI > 0.25 in Schumacher et al. (2022) and Weiler et al. (2023)

and > 0.3 in La Chioma et al. (2019)). Thus, for the sake of comparison to studies using different tuning cutoffs, all visually responsive cells were included in the PO and PD comparisons. Consistency in OSI and DSI was evaluated as the Pearson's R between sessions, and consistency in PO and PD was calculated as the circular correlation between sessions.

3.4.1 Visual Tuning Properties are Consistent Between Repeated Head Fixed Sessions

During repeated head fixed sessions, re-identified cells exhibited similar tuning curves (**Figure 3.9**). In the deconvolved fluorescence traces, I occasionally observed early and late peak responses during the visual stimulation period (**Figure 3.9 A**, cell 2, **Figure 3.9 B**, cells 1 and 2). As the phase of the grating stimulus was reset to zero before each stimulus trial, it is unlikely that these observed peaks are the result of systematically different positions of the grating relative to the RFs of these cells. Rather, they could potentially be caused by eye movements or differences in attention levels during individual trials.

OSI and DSI measurements in cells re-identified between repeated head fixed sessions were significantly positively correlated (**Figure 3.12 A** and **B**, left; OSI: R = 0.510, p = 0.0017; DSI: R = 0.494, p = 0.0026), indicating that cells generally maintained their selectivity. Regarding stimulus preference, PO was consistent between repeated head fixed sessions and exhibited an average change of only 3.4° ± 32.9° (**Figure 3.13 A**, left, R = 0.683, p = 4.9 x 10^{-4}). PD was either consistent (falling along the unity line) or changed by approximately ±180° (**Figure 3.13 B**, left, R = 0.414, p = 0.049). Such cases appeared mostly amongst cells that were direction tuned during only one session, likely due to response variability between sessions.

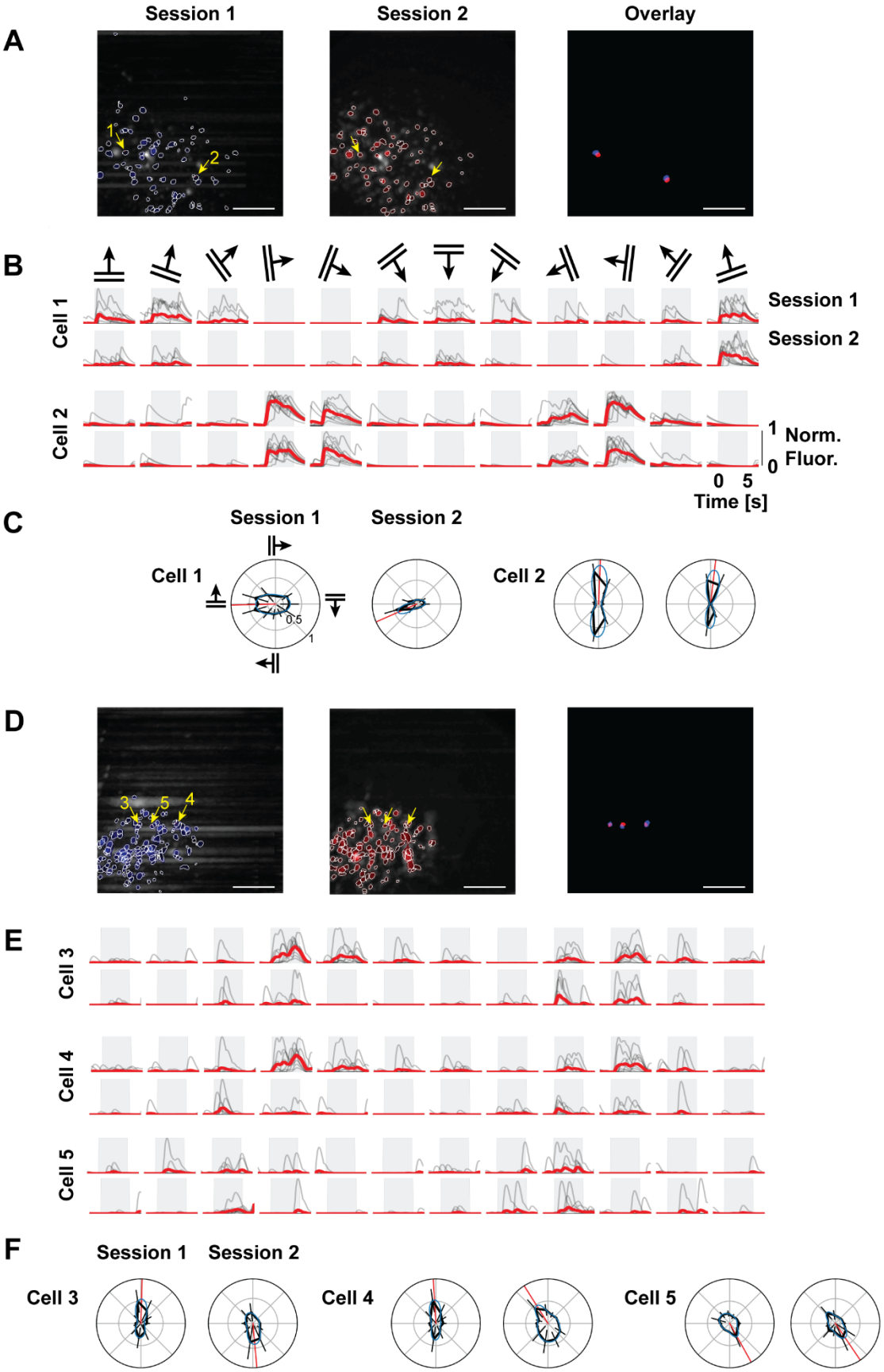

Figure 3.9 Example re-identified cells from repeated head fixed imaging sessions | A. Max projection FOVs of both sessions with re-identified ROIs. Example re-identified ROIs were initially matched using CaImAn and manually curated. Scale bar = 100 µm. **B.** Deconvolved fluorescence traces from the re-identified cells in **A**. **C.** Polar direction tuning curves for the cells re-identified in **A**. **D-F.** Same as **A-C** from a different mouse.

3.4.2 Visual Tuning Properties are Variable Between Repeated Freely Moving Sessions

During repeated freely moving sessions, the consistency seen in repeated head fixed sessions was generally not observed. Re-identified cell responses were very different between sessions (**Figure 3.10**). Early and late responses to visual stimuli were also observed in the consecutive freely moving experiments (**Figure 3.10**, all cells). As the visual stimulus grating phase was reset after every trial, as in repeated head fixed sessions, grating phase-dependent RF reactivation was unlikely. It is possible that late RF stimulation occurred if a mouse looked above the edge of the VR arena at the beginning of a trial and then moved his head down, causing the grating to appear only later in the trial, since such trials were not excluded from this analysis.

The selectivity indices were broadly scattered and showed no significant relationship (**Figure 3.12 A** and **B**, middle, OSI: R = -0.021, p = 0.960; DSI: R = -0.145, p = 0.731). Similarly, neither PO nor PD was significantly correlated between consecutive sessions (**Figure 3.13 A**, middle; R = -0.029, p = 0.939), although the ±180° change in PD observed during repeated head fixed sessions was again present (**Figure 3.13 B**, middle; R = 0.023, p = 0.950). The fact that visual tuning seemed much more variable in repeated freely moving sessions while it appeared rather consistent under head fixed conditions indicates that neuronal activity in V1 of the freely moving mouse is heavily influenced by factors other than visual stimuli. This will be addressed further below.

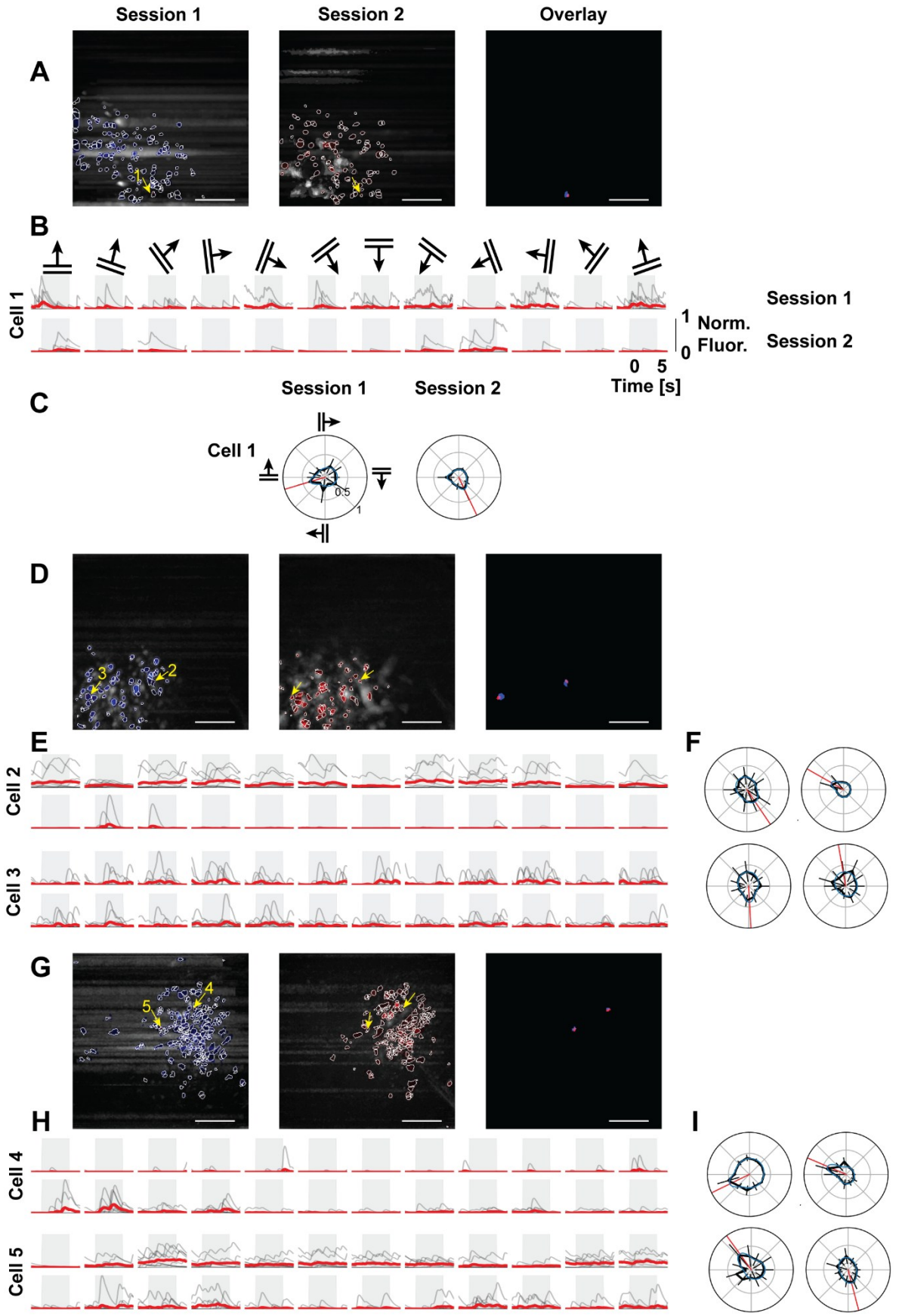

Figure 3.10 Example re-identified cells from repeated freely moving imaging sessions | Same as **Figure 3.9** for repeated freely moving experiments. **A-C**, **D-F**, and **G-I** are experiments from different mice.

3.4.3 PO is Consistent, While OSI, DSI, and PD are Variable Between Consecutive Head Fixed and Freely Moving Sessions

It was possible to re-identify cells between head fixed and freely moving sessions, and tuning curves for several hand-selected example cells are presented in **Figure 3.11**. The example cells from the experiments described in **Figures 3.1 – 3.6** are shown in **Supp. Figure 5**. While ideally one would start by comparing response properties only during periods of quiescence between head fixed and freely moving configurations, this was precluded by the distribution of locomotion during freely moving sessions. Mice tended to move consistently throughout freely moving sessions, while during head fixed sessions, longer periods of stillness were observed (**Supp. Figure 2 A**).

In general, cells exhibited large changes in their tuning properties between sessions. Cells gained or lost orientation and direction selectivity (**Figure 3.11**, cells 1-7; **Supp. Figure 5**, cells 2, 7, 8) or shifted their preferred orientation or direction (**Figure 3.11**, cells 1, 4, 6, 8; **Supp. Figure 5**, cells 3 and 4). Some cells maintained their selectivity indices between sessions (OSI: **Figure 3.11**, cell 8; DSI: **Figure 3.11**, cells 3 and 8). OSI values were significantly greater during the head fixed sessions (**Figure 3.12 A**, right, $p = 6.9 \times 10^{-8}$, Kruskal-Wallis), but values were not significantly correlated between sessions ($R = 0.105$, $p = 0.399$). DSI values did not exhibit clear changes between head fixed and freely moving sessions ($R = 0.183$, $p = 0.139$).

While selectivity varied across sessions, stimulus preference displayed a somewhat different pattern. The PO in re-identified cells was significantly correlated between head fixed and freely moving experiments (**Figure 3.13 A**, right, $R = 0.317$, $p = 0.019$). Interestingly, these cells seemed to show a small but consistent counterclockwise rotation in their PO during freely moving sessions (see **Figure 3.11 B** and **Figure 3.13 A**, right, dashed line; mean: 16.0° ± 60.5°). Although this PO change was not significant ($p = 0.317$, Watson-Williams), it differs from the naïve expectation that PO changes would be evenly distributed. Potential origins of this rotation will be discussed later. Changes in PD were variable, exhibiting broad scattering (**Figure 3.13** right, $R = -0.093$, $p = 0.421$).

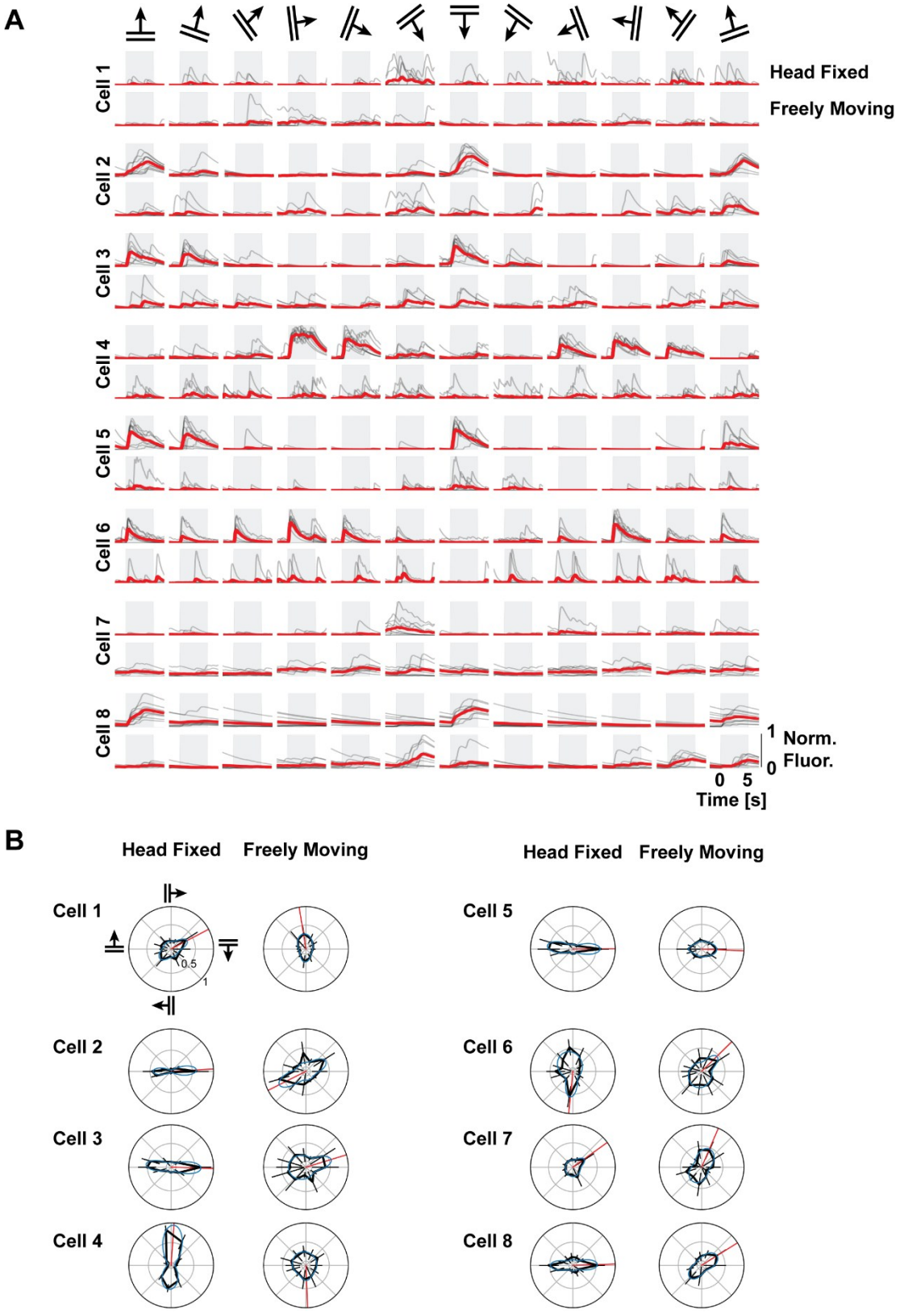

Figure 3.11 Tuning curves from hand-selected example re-identified neurons between head fixation and free behavior | A. Deconvolved fluorescence traces from eight cells re-identified between consecutive head fixed and freely moving sessions. **B.** Polar direction tuning curves for the cells in **A**. Black line – mean trial AUC ± std, blue line – double Von Mises function fit to the mean. Red line – preferred direction. N = 4 mice.

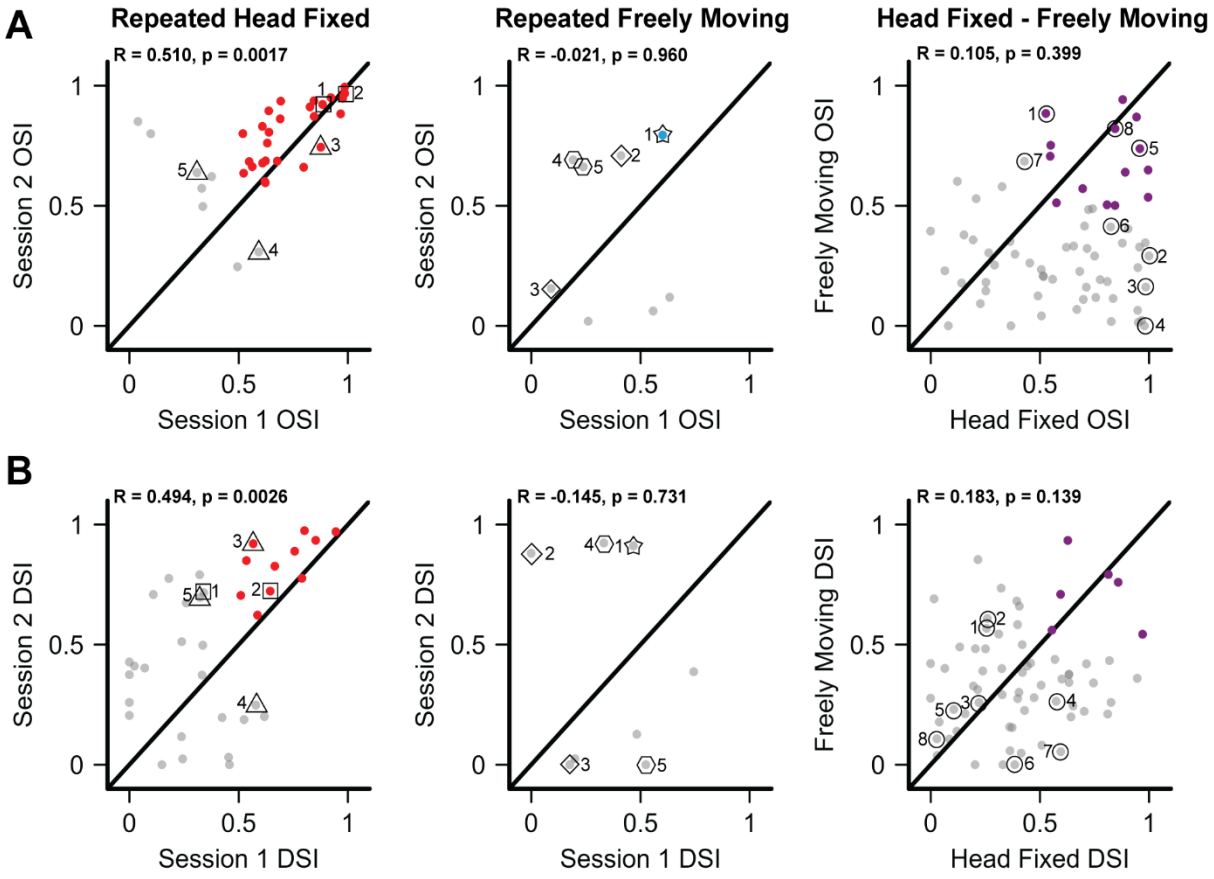

Figure 3.12 Orientation and direction selectivity indices are consistent in repeated head fixed sessions, but not in experiments with free behavior | A. OSI consistency in re-identified cells between repeated head fixed, repeated freely moving, or consecutive head fixed and freely moving experiments. Colored dots are cells with OSI ≥ 0.5 during consecutive experimental sessions (orientation tuned in both sessions). Labelled dots correspond to the cells shown in **Figure 3.9**, **Figure 3.10**, and **Figure 3.11** for repeated head fixed, repeated freely moving, and head fixed – freely moving experiments. **B.** Same as **A** for DSI. Repeated head fixed sessions: n = 35 cells from 3 mice. Repeated freely moving sessions: n = 8 cells from 4 mice. Consecutive head fixed – freely moving sessions: n = 67 cells from 6 mice.

As the number of manually re-identified cells that was visually responsive in both sessions was low, I repeated this analysis for automatically re-identified cells. For changes in OSI and DSI, the results were similar (**Supp. Figure 3**). Changes in PO and PD were more scattered across all experimental configurations (**Supp. Figure 4**), although repeated head fixed sessions still showed greater consistency than sessions with free behavior. The decrease in consistency across all experiment types potentially arises from incorrect re-identifications using the automatic cell matching algorithm.

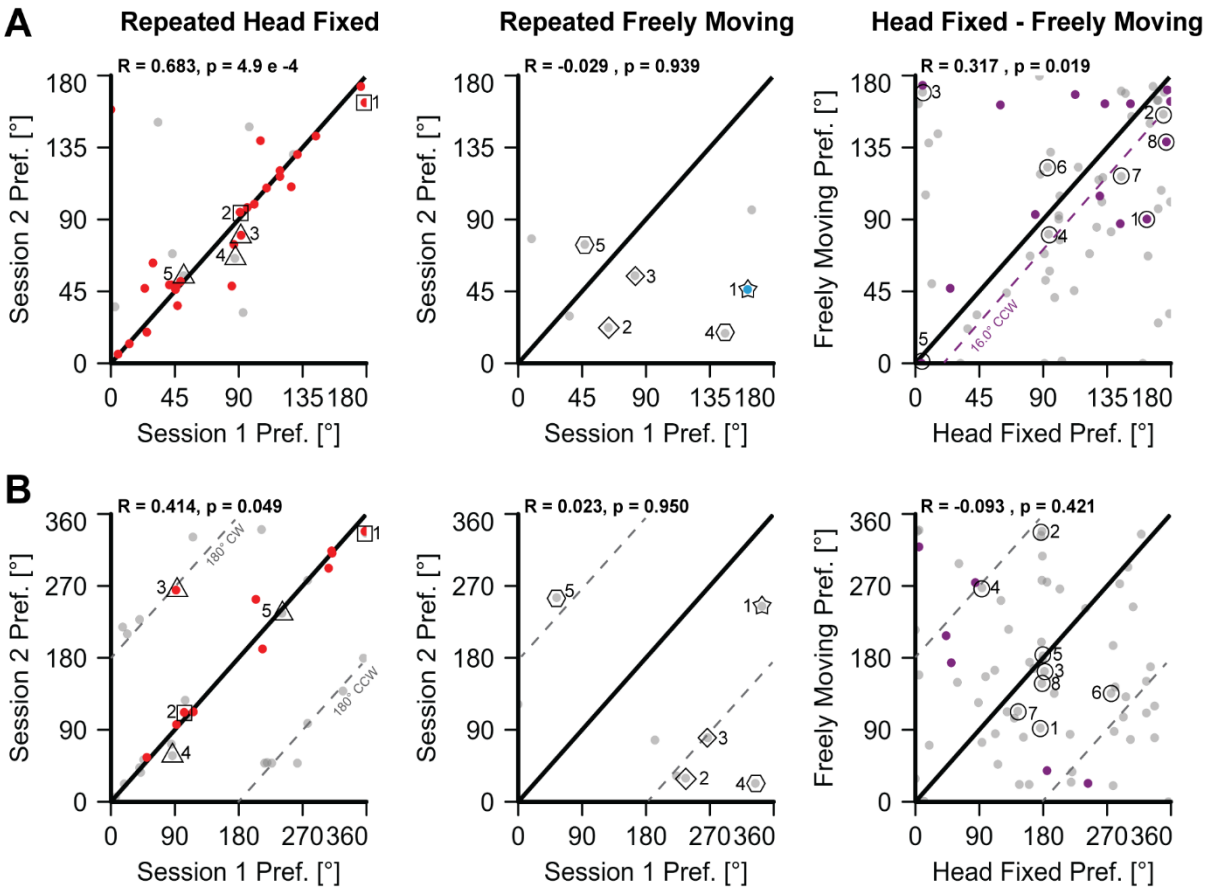

Figure 3.13 Preferred orientation and direction are consistent in repeated head fixed sessions, but not in experiments with free behavior | A. Preferred orientation stability in re-identified cells between repeated head fixed, repeated freely moving, or consecutive head fixed and freely moving experiments. Colored dots are cells that were orientation tuned in both experiments (OSI ≥ 0.5, same as from **Figure 3.12**). Labelled dots correspond to the cells shown in **Figure 3.9**, **Figure 3.10**, and **Figure 3.11** for repeated head fixed, repeated freely moving, and head fixed – freely moving experiments. **B.** Same as **A** for the preferred direction. Dashed lines: ±180°. Repeated head fixed sessions: n = 35 cells from 3 mice. Repeated freely moving sessions: n = 8 cells from 4 mice. Consecutive head fixed – freely moving sessions: n = 67 cells from 6 mice.

3.5 Self-Motion Tuning in V1 Neurons

Activity in sensory cortex is known to be correlated with, and even driven by self-motion and body position (Niell and Stryker, 2010, Keller et al., 2012, Stringer et al. 2019, Mimica et al., 2023). Since the analysis of self-paced, unstructured behavior is inherently difficult given the lack of clear task-oriented objectives, I chose to calculate tuning curves to the self-motion variables measured during head fixed and freely moving experiments according to the method in Stefanini et al. (2020). Briefly, the range of the self-motion trace for a given variable was binned and the mean inferred spike rate for each range bin was used to construct the self-motion tuning curve (**Figure 3.14 A** and **Methods**). Cells exhibited several responsivity characteristics. Some exhibited moderate responsivity to one self-motion variable with weak to moderate responsivity to others (**Figure 3.14 B**, cell 2), while others were moderately responsive to variables recorded during freely moving sessions, but not during head fixed sessions (cell 3). Other cells showed weak responsivity to all kinematic variables (cell 6), while still others were unresponsive to kinematic variables (cell 8). Cells were considered significantly tuned to a self-motion variable if they passed both responsivity and quality tests (see **Methods 2.2.10.6**). Across the population of recorded cells, all self-motion variables were represented (**Figure 3.15**), although not all variables were represented in single cells (**Figure 3.15**). For most variables, approximately 10-20% of cells exhibited significant tuning on average. Data are reported as mean percentage of cells tuned per experiment.

During head fixed sessions, pupil diameter was represented in the V1 population (mean = 21.3 ± 11.0%, **Figure 3.15 A**), in line with previous results linking increases in pupil diameter with increases in arousal and neuronal activity (Joshi et al., 2016; McGinley et al., 2015; Reimer et al., 2014). Running wheel speed during head fixed experiments was only very weakly represented (mean = 4.9 ± 10.3%).

Locomotion speed during freely moving experiments was represented more strongly than running wheel speed during head fixation (mean = 19.5 ± 16.3%). Despite finding that cells rarely exhibited consistent running-evoked responses (**Figure 3.5**), neural activity was modulated by locomotion, and the fraction of modulated cells was similar between head fixed and freely moving experiments (mean = 62.6 ± 29.4% and 70.8 ± 20.3%, respectively).

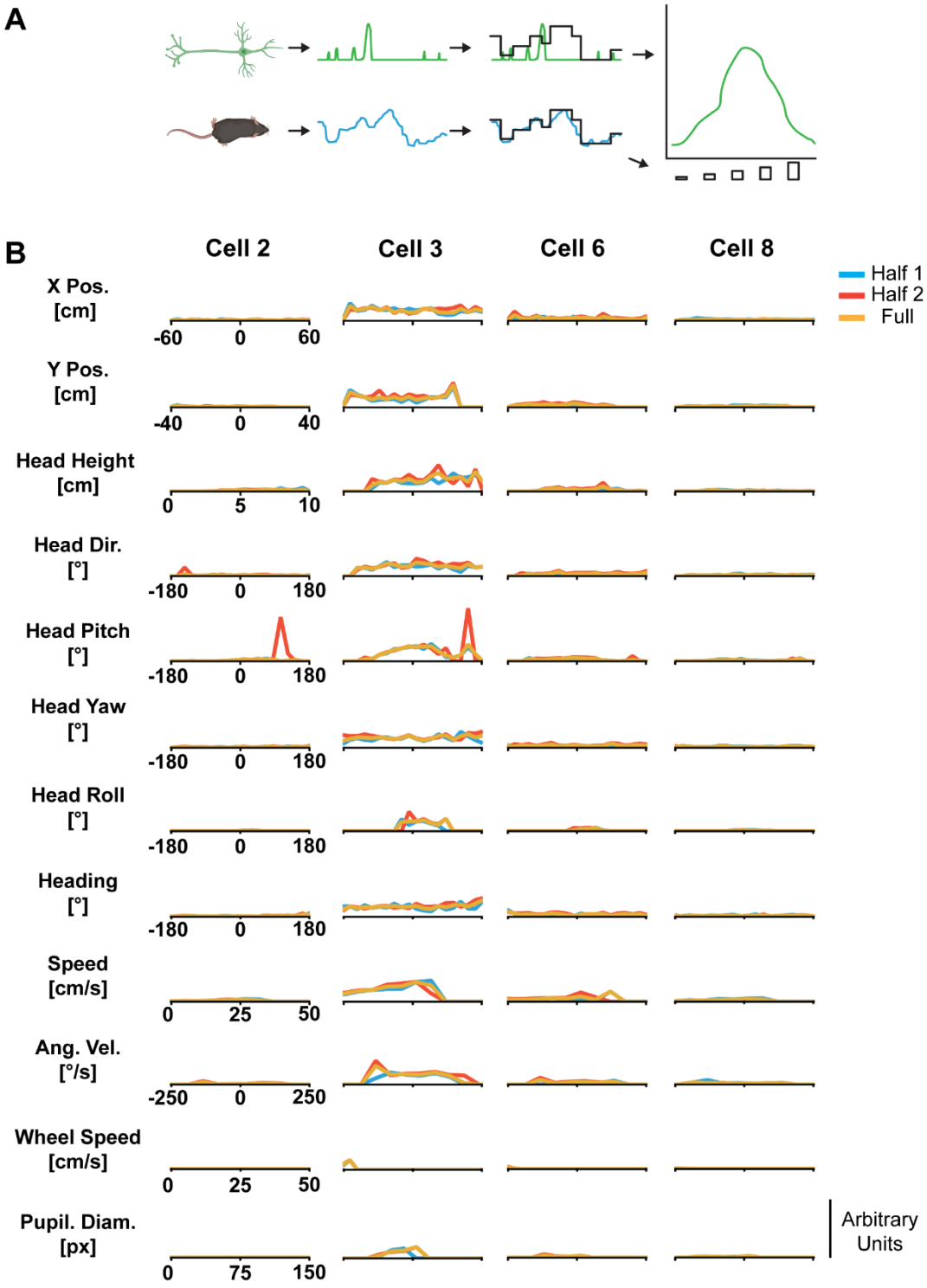

Figure 3.14 Self-motion tuning schematic and example self-motion tuning curves | A. Schematic illustrating the computation of self-motion tuning curves. Self-motion variables are binned according to their range, and the corresponding neural activity is used to construct the tuning curve (see **Methods 2.2.10.6**). Schematic courtesy of Drago Guggiana Nilo. **B.** Self-motion tuning curves from four re-identified cells. Blue and red traces are tuning curves calculated on the first and second half of the experiment, respectively. Yellow traces are tuning curves calculated on the entire experiment.

The 3D position of the mouse head was represented similarly across the three axes (x: 8.2 ± 9.2%, y: 10.1 ± 16.6%, z: 12.2 ± 11.7%), as were rotations of the head about the x and z axes (head roll = 8.5 ± 8.3%, head yaw: 7.8 ± 8.0%). Interestingly, head pitch was more strongly represented (mean = 29.2 ± 18.4%) compared to other head rotations. The angular head speed, head-body angle, and overall mouse heading were all weakly represented (mean = 3.5 ± 4.0%, 4.9 ± 5.7%, and 8.9 ± 13.0%, respectively).

3.5.1 Self-Motion Tuning is Mostly Consistent During Experiments without Visual Stimuli

The fraction of cells tuned to self-motion was generally similar between the head fixed and freely moving experiments and control experiments conducted without visual stimuli (**Figure 3.15** yellow and gray, **Table 2** and **Table 3**).

During head fixed experiments, there was no significant difference in the fraction of cells tuned to wheel speed nor in the fraction of cells modulated by running between experiments with visual stimuli and illuminated or dark controls (**Figure 3.15** and **Table 2**, **Supp. Figure 2**). There was also no significant difference in the fraction of cells tuned to the pupil dimeter between experiments with visual stimuli and control experiments in the illuminated arena; however, a strong difference was observed compared to controls conducted in darkness.

During freely moving experiments, the fraction of self-motion tuned cells was more similar between the main experiment and the darkness control experiment than between the main experiment and the controls conducted in the illuminated arena (**Figure 3.15 B** and **Table 3**), with illuminated control experiments typically showing a slight but significantly greater fraction of cells tuned to self-motion or postural variables.

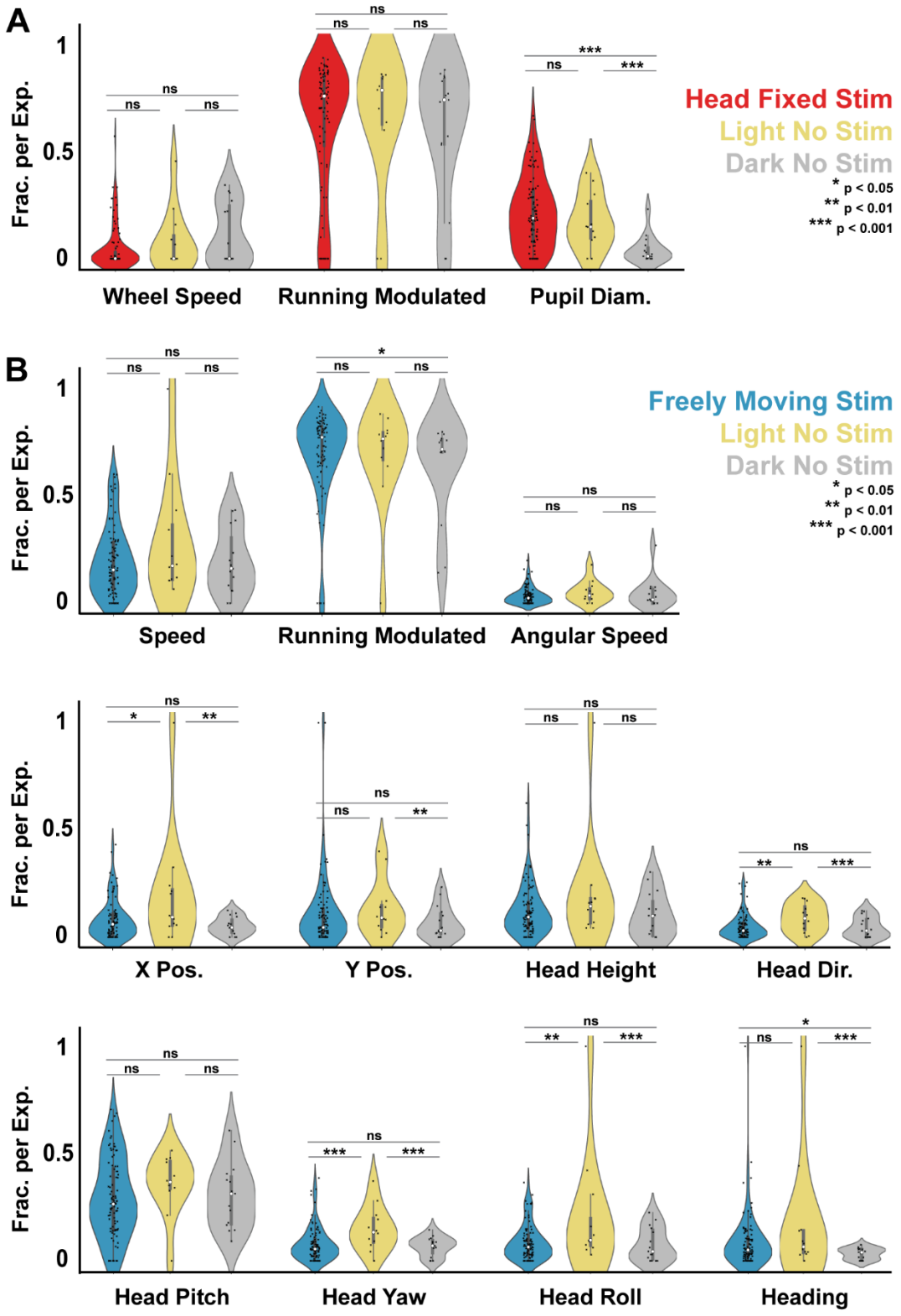

Figure 3.15 All self-motion and postural variables are represented across the V1 population | A. Fraction of cells per experiment significantly tuned to self-motion or postural variables during head fixed (red) experiments compared to controls without visual stimuli conducted either in light (yellow) or darkness (gray). White circles – median, black dots – single experiments. **B.** Same as **A**, but for freely moving experiments (blue). n = 92, 12, and 15 experiments across 8 mice for full experiment, illuminated control, and dark control, respectively.

3.6 Multimodal Representation of Visual and Self-Motion Stimulus Information

Since single V1 cells exhibited tuning to both visual stimuli and self-motion/postural variables as well as activity not directly explained by either variable class, I sought to visualize the co-representation of visual and self-motion tuning across the population of imaged V1 neurons. I created a tuning vector consisting of the tuning index for each self-motion variable and the DSI and OSI for each cell and used the UMAP method to embed the tuning vector in a low-dimensional space (**Figure 3.16**). Cells recorded during head fixed and freely moving sessions were embedded into different UMAP spaces, but with the same parameters. As previously mentioned, longitudinal cell matching within mice was not done, all recordings were treated independently, and the same cells may be repeatedly represented in the dataset. Additionally, it is acknowledged here that all interpretations derived from the UMAP visualization must be confirmed via direct experiments or further analyses.

3.6.1 Visual Stimulus Variables

The population of cells recorded during both head fixed and freely moving experiments (**Figure 3.16 A** and **B**) appeared as banded structures for OSI and DSI in the UMAP space, with bands of moderately to strongly tuned cells grouping together, but separated by a band of weakly-tuned cells. The population did not exhibit a smooth gradient of tuning that spanned the entire UMAP space, suggesting subpopulations of cells that have varying degrees of visual tuning. Interestingly, OSI and DSI groups were visually perpendicular to each other in both experimental types. While a small number of cells with both high OSI and DSI values overlapped (**Figure 3.16 A,** bottom right corners, and **Figure 3.16 B**, upper left corners), there was greater overlap between moderately orientation selective cells and moderately direction selective cells, suggesting that cells are either strictly orientation or direction tuned, or otherwise more generally responsive.

3.6.2 Self-Motion Variables

In the population of cells recorded during head fixed experiments, cells tuned to pupil diameter appeared as two distinct, non-overlapping groups, likely corresponding to states of pupil dilation and constriction. Cells tuned to running wheel speed appeared with a similar structure with two separated, non-overlapping groups (**Figure 3.16 A**). One group of cells was strongly tuned to both pupil size and running wheel speed, potentially representing the known link between running speed and pupil dilation (McGinley et al., 2015; Niell and Stryker, 2010; Reimer et al., 2014).

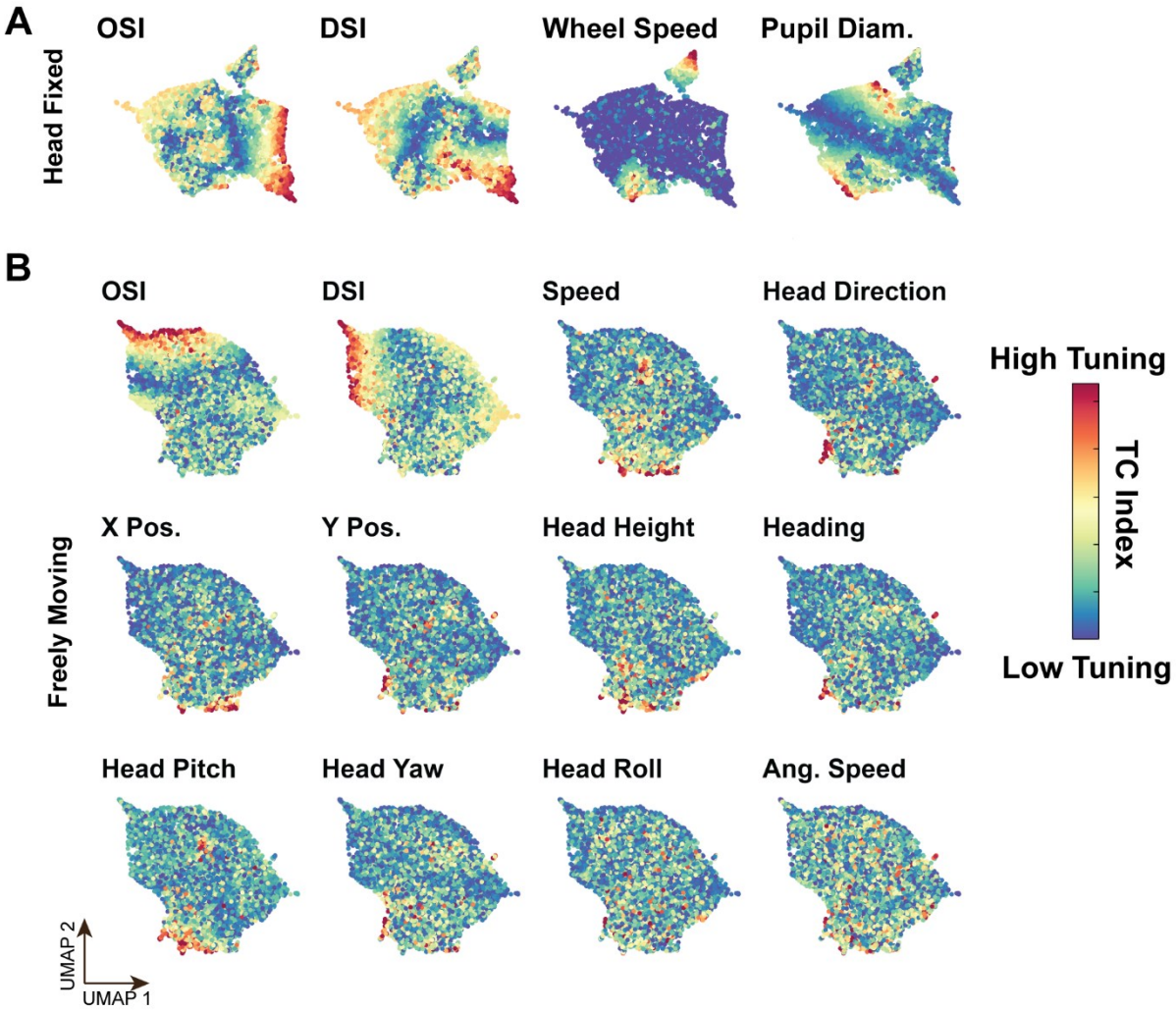

Figure 3.16 Groups of cells with strong visual selectivity do not overlap with strongly self-motion tuned groups | A. UMAP embedding of tuning vectors for all cell observations (n = 5940) recorded across all head fixed experiments. Tuning vectors were constructed from the tuning indices to all self-motion and postural variables and the DSI and OSI for a given cell. The color map refers to tuning strength for the listed variable. **B.** Same as A for all cell observations recorded across 8 mice during all head fixed and freely moving experiments (n = 7438).

In the neuronal population recorded during the freely moving experiments (**Figure 3.16 B**) cells strongly tuned to self-motion and postural variables, particularly the position, rotations (especially head pitch), and direction of the head, as well as locomotion speed, generally appeared nearby or overlapped with each other, with some strongly tuned cells scattered throughout. Cells tuned to head roll and the angular velocity of the mouse did not appear in distinct groups, but rather were more evenly distributed across the UMAP space. Much like the cells tuned to running wheel speed in the head fixed sessions, cells tuned to free locomotion speed appeared in two groups of strong tuning.

Interestingly, groups of cells strongly tuned to self-motion variables appeared to have limited overlap with cells moderately to strongly tuned to visual variables. Rather, clusters with weak to moderate visual tuning tended to overlap more with groups of cells moderately to strongly self-motion tuned.

3.6.3 Multimodal Representations in Re-Identified Cells

To test if the population of cells re-identified between head fixed and freely moving imaging sessions was consistent with the broader population, I embedded just the re-identified cells into UMAP space with a tuning vector consisting of all 16 visual and self-motion variables (**Figure 3.17**).

Given the smaller number of re-identified cells, groupings were less distinct than with the overall population but exhibited similar overlap patterns. During head fixed experiments, cells with a strong OSI or DSI appeared with a banded structure, with overlap in moderately to strongly tuned cells (**Figure 3.17 A** and **B**), like the overall population (**Figure 3.16 A** and **B**). However, during the freely moving experiments, the re-identified cells no longer exhibited the visually perpendicular grouping observed in the entire population embedding. Rather, a structure more like that observed in the head fixed sessions was apparent, with overlap in moderate to strongly tuned cells. Interestingly, several cells that previously displayed low to mid-range OSIs or DSIs during head fixation displayed high OSI and DSI values during free behavior.

Much like the embedding of the entire population, re-identified cells appeared as two distinct running wheel speed groups (**Figure 3.16 A** and **Figure 3.17 A**), and at least one distinct group of cells strongly tuned to pupil diameter, with overlap between the

pupil diameter and one of the running wheel clusters (**Figure 3.17 A**). Cells strongly tuned to head pitch, position and direction, and locomotion speed appeared as groups that were small but distinct and found near one another (**Figure 3.17 B**). Other variables, like the yaw, roll, and angular speed of the head did not display clear organization (**Figure 3.17 B**). As with the entire population, when groups of cells strongly tuned to self-motion or posture were present, they did not overlap with cells showing strong orientation or direction selectivity in either the head fixed or freely moving condition, but rather corresponded to cells with moderate visual tuning.

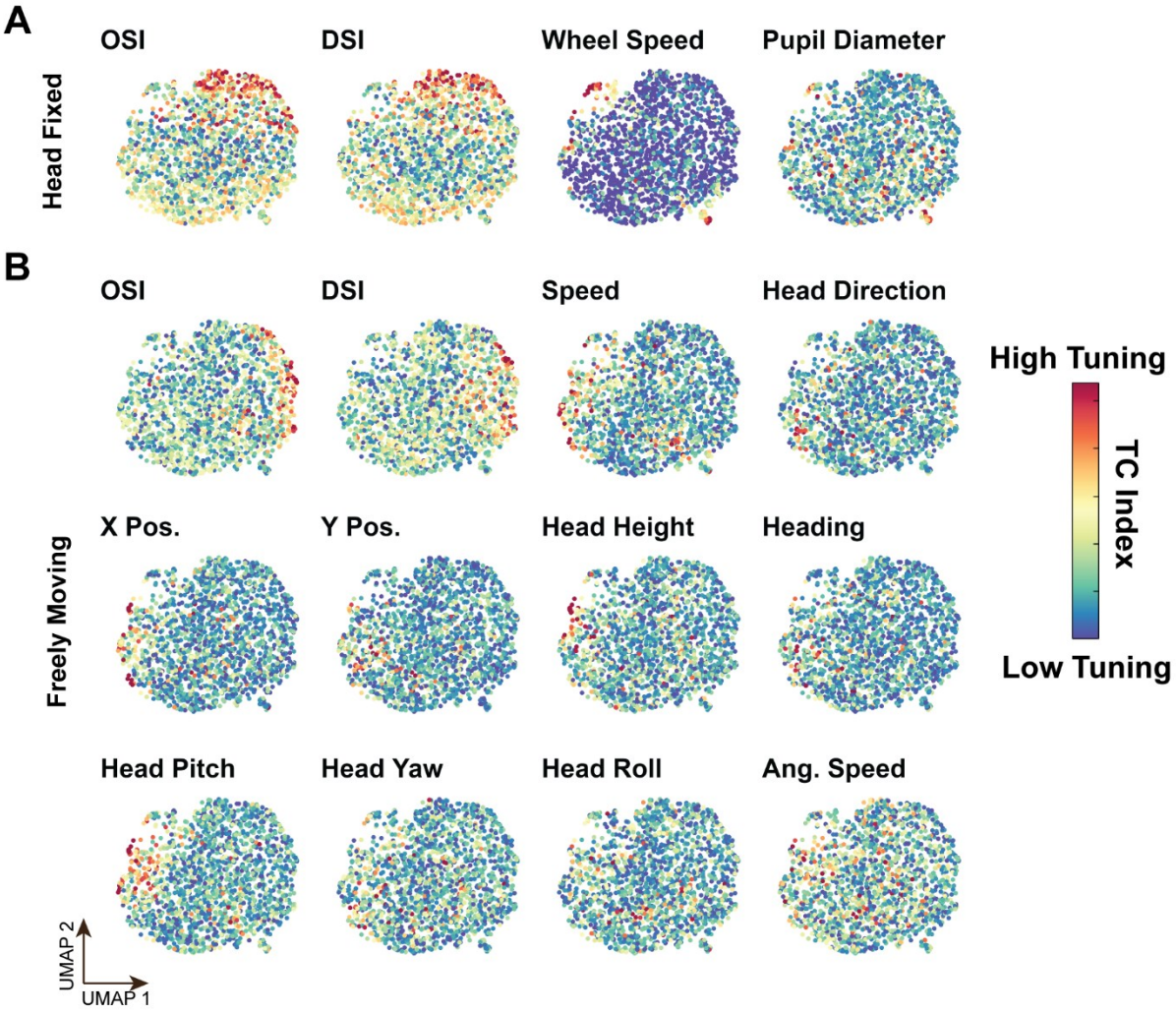

Figure 3.17 Re-identified cells exhibit separation between visual and self-motion, but larger overlap between orientation and direction selective cells | UMAP embedding of tuning vectors as in **Figure 3.16** for all re-identified cell observations across 8 mice during the corresponding (**A**) head fixed and (**B**) freely moving experiments (n = 1747).

4 Discussion

To determine how self-motion is represented and influences orientation and direction tuning in binocular V1 cells, I recorded neural activity with wireless 1P miniscopes as mice moved freely in an immersive VR arena. This study is, at the time of writing, the first description of orientation and direction selectivity in freely moving mice. The main results from this study are: (1) the development of a methodology to study visual tuning properties and multisensory integration in mice during free behavior, (2) that self-motion and posture are widely represented in the V1 population, (3) that orientation and direction selectivity and preference are consistent between repeated head fixed experiments, (4) but that orientation and direction selectivity are not consistent between repeated freely moving or consecutive head fixed and freely moving conditions, although (5) the PO between consecutive head fixed and freely moving experiments is correlated and exhibits a consistent counterclockwise rotation. These findings are likely due to interactions with representations of self-motion and posture.

4.1 Calcium Imaging of V1 Neurons During Visual Stimulation in Freely Moving VR

Immersive VR systems are powerful tools for studying freely moving responses. Systems such as those presented by Stowers et al. (2017) and Del Grosso et al. (2017) are built on open-source software (OSS), custom-written 3D graphics and physics engines. The ratCAVE system from Del Grosso et al. (2017) was modified, replacing the custom Python and OpenGL graphics engine with the commercially available video game development software Unity3D (Guggiana Nilo et al., in preparation). Using the Unity3D backend, a detection-to-projection latency of 18 ms was achieved (Guggiana Nilo et al., in preparation), which was only slightly longer than the 15 ms reported by Del Grosso et al. (2017). However, as mice rarely reached locomotion speeds exceeding 50 cm/s (corresponding to a distance of about 1 cm between detection and projection) during freely moving experiments (**Supp. Figure 2**), consistent with the rat locomotion speeds reported by Del Grosso et al. (2017), it is unlikely that mice experienced any latency-related visual distortions in the VR arena. The VR system allowed for tight spatial and temporal control over the presentation of

visual stimuli to freely moving mice while maintaining flexibility for varied stimulus and experimental design.

To approximate classical visual neuroscience experiments designed to probe orientation and direction tuning, I developed a spherically corrected, sinusoidal drifting grating Gabor stimulus which maintained its position and rotation relative to the mouse's head. Using wirefree miniscopes, I recorded calcium activity from tens to over 100 cells per animal and re-identified the same imaged cells during visual stimulus trials in head fixed and freely moving experiments on the same day. Combining the tracked position and orientation of the mouse head with pose estimation data from recorded videos, I measured a variety of self-motion and posture related variables, which when combined with the miniscope recordings, allowed me to observe both visually driven and self-motion related activity in V1 neurons.

Cells in V1 showed expected, clear responses to visual stimuli during head fixed sessions and during free behavior. The activity of some cells was clearly locked to stimulus onset, while others exhibited more distributed response onsets and non-visually evoked activity. Some cells were more responsive in the freely moving session compared to the head fixed session. The increase in activity was not necessarily visually driven, likely due to overall increases in body movement, although other cells showed more visual responsiveness during free behavior. Stimulus offset responses were also observed in both sessions. These may reflect the tendency of V1 neurons to exhibit off responses in the central binocular visual field (Williams et al., 2021), or may be due to eye movements shifting the stimulus outside of the RF of the cell.

V1 neurons also showed expected locomotion-related activity during head fixed and freely moving sessions. Cells occasionally responded just before locomotion onset, in line with the predictive processing interpretation of visual processing (Keller and Mrsic-Flogel, 2018). Neural activity was generally elevated during locomotion, regardless of if the mouse was head fixed or not, and the vast majority of cells were modulated by running in both conditions, consistent with previous reports (Andermann et al., 2011; Guitchounts et al., 2020; Keller et al., 2012; Niell and Stryker, 2010).

4.1.1 Technical Considerations, Limitations, and Suggested Improvements

The decision to exchange the OSS backend from the ratCAVE system and replace it with a commercial software was made for two reasons – ease of setup and future extensibility. Unity3D is easy to install and supports a range of plugins for rapid graphics development and interfacing, such as official support for the motion tracking system used in this work. Further, it has a rich development community with extensive documentation and is freeware for non-commercial projects. OSS projects often suffer from opaque documentation, a lack of development with software and computing hardware updates, or are abandoned as developers move on to other roles (Nowogrodzki, 2019). By choosing a commercially available game engine as a backend, projects developed using this system are more likely to be compatible with future updates.[1]

In this iteration, the VR system exhibits a few technical limitations. Since all visual stimuli are presented with a projector, the contrast available in the visual scene is less than that of a computer monitor, as parts of the scene rendered in black will receive ambient reflections from the lit portions of the visual scene. For the experiment presently discussed, the contrast was sufficient to drive strong visually evoked responses in V1 but may pose problems when presenting smaller or low contrast visual stimuli. The walls of the arena are also relatively low (50 cm) and there are no means to present stimuli directly above the subject. Since rodents maintain an overhead binocular visual field (Wallace et al., 2013), a portion of their field of view will fall above the projection surface of the arena and will not receive the intended visual stimuli, but instead see elements of the experimental room. To address this concern, I only analyzed trials where at least half of the presented Gabor stimulus was visible on the walls of the arena. For experiments where overhead visual stimuli are needed (e.g. overhead looming stimulus experiments), other arena designs must be developed.

[1] This is not a rebuke of open-source projects in general, as much of the work in this thesis relies on open-source projects such as MiniAn, CaImAn, DeepLabCut, the UCLA miniscope, and utilities from the ratCAVE project. Instead, I wish to point out the reality that maintaining OSS is typically more work than one expects and should not be understated. For example, the OSS NumPy library for array computations in Python (Harris et al., 2020) has 29 active maintainers, staffs a large team overseeing documentation and testing, and is actively funded. At the time of writing, the ratCAVE project is labelled as “abandonware” and is no longer actively developed or supported, while the GitHub repository for the system described in Stowers et al. was last updated in 2022.

The choice of using the wirefree UCLA miniscope V3 was motivated by the desire to (1) avoid excessive cable drag, since a commutator would need to be installed 2 m above the arena floor due to the projector, and (2) avoid distortions of the visual stimulus caused by shadows cast by the cable. The apparatus that the mouse needed to carry (head bar, tracker, and miniscope) weighed a combined 5.8 g, with most of the weight located at the end of the miniscope in the battery. This caused significant torquing forces, and while I chose adult male mice that weighed at least 28 g, they required at least one week of acclimation before experiments were conducted. The reliance on battery power also limited the number of trials that could be shown to a mouse during a given experiment. The 40 mAh battery delivered sufficient current for approximately 25 minutes, enough for 10 repetitions of 12 stimulus directions with one spatial and temporal frequency. Finally, the UCLA V3 miniscope uses a GRIN lens as its image forming lens, with a working distance of 200 µm, limiting the depth of imaging to superficial layer 2/3.

Since experimental work on this project began, several new tools and methods were released that address most of the technical concerns I raised previously. The NINscope, a lighter-weight (1.6 g) version of the UCLA V3 miniscope (de Groot et al., 2020), offers the option to implant more than one miniscope for multi-region imaging with simultaneous optogenetic stimulation while recording. The UCLA version 4 miniscope delivers lighter weight (2.6 g) and a lower profile, a larger FOV (1 x 1 mm), electronic focal adjustment, an integrated inertial measurement unit (IMU), and requires less excitation power. The latter no longer requires imaging through GRIN lenses, but instead can achieve cortical imaging through glass coverslips, as with conventional 2P imaging. Together with newly available, ultra-thin (0.3 mm) power, data, and communications cables, these 1P miniscopes enable longer experiments with more trial repetitions and less load on the mouse, without significant shadows cast by the cable. However, the reliance on cabling for these miniscopes necessitates having a commutator, which still introduces cable drag and stimulus distortion despite the lighter weight of the systems.

Imaging through a cranial window also would allow for collecting 2P imaging stacks of the cells found in the 1P FOV for post-hoc structural registration with a “ground truth” measurement of visual stimulus tuning. Alternatively, using a commercially-available mini-2P (Zong et al., 2022) or newly developed mini-3P (Klioutchnikov et al., 2023;

Zhao et al., 2023) microscopes would allow for cellular and sub-cellular imaging into deeper layers of cortex during free behavior. Both microscopes are of comparable weight to the UCLA V4 miniscope (< 3 g) and have similar FOVs as the UCLA V3 miniscope used in this study (~400 μm x 400 μm). However, both require an external tabletop laser, which adds additional operational and cost constraints, and more intensive cabling, which may interfere with finer visual stimulation.

Utilizing lighter weight optical hardware also introduces the option for adding eye and facial movement tracking during free behavior. The systems introduced by (Meyer et al., 2018; Sattler and Wehr, 2021) weigh just over one gram and can record one or both eyes, as well as the visual environment from the mouse point of view. These can be used to measure receptive fields during free behavior, as in (Parker et al., 2022b), or be used during ethologically relevant behaviors to monitor gaze, arousal states, and whisking behavior.

4.2 Visual Tuning Properties are Measurable in Both Head Fixed and Freely Moving Configurations

Orientation and direction selective cells were observed during both head fixed and freely moving sessions, and the fraction of visually responsive, orientation selective, and direction selective cells found per experiment during either session was significantly greater than during control experiments without visual stimuli, indicating that these responses were indeed driven by the visual stimulus. I observed similar fractions of visually responsive cells between head fixed and freely moving sessions, although there was a significantly greater fraction of orientation or direction tuned cells in head fixed versus freely moving sessions. This could be due to a number of factors. During freely moving sessions, trials were discarded if the head pitch of the mouse rose such that more than half of the Gabor stimulus was outside of the upper edge of the arena. Hence, undersampling of trial responses may be an issue. Another contributing factor may lie in the calculation of the OSI and DSI. During freely moving sessions, cells considered visually responsive also strongly responded to self-motion related variables both outside of and during the visual stimulus periods, and those contributions were largely independent. Thus, although fewer cells could achieve a high enough OSI or DSI to be considered tuned to orientation or direction given the

strong self-motion activity responses during freely moving behavior, the cells considered tuned exhibited clear selectivity and preference.

The fraction of cells found to be orientation selective during head fixed experiments was approximately four to eight times lower than previously reported (10% here vs. 35-45% in (Fahey et al., 2019) and 75% in (Niell and Stryker, 2008)), and only 8% of recorded neurons were direction selective. This may be due to a combination of factors, including imaging depth, recording mixed excitatory and inhibitory populations, and how visual responsivity and selectivity indices were calculated. With the wirefree miniscope, I was able to image superficial layer 2/3 of V1, achieving a maximum imaging depth of 200 μm below the brain surface. V1 is known to have depth-dependent and cell-type specific tuning properties. In upper layer 2/3, approximately 50% of cells are visually responsive (O'Herron et al., 2020; Weiler et al., 2023) and exhibit an average OSI of 0.4 - 0.7 when measured with 2P imaging (O'Herron et al., 2020; Weiler et al., 2023) or 0.9 when measured with silicon probes (Niell and Stryker, 2008). Direction tuning has also been shown to increase with cortical depth (Niell and Stryker, 2008; O'Herron et al., 2020), which may partially explain the low fraction of direction selective cells in my data.

In half of the animals used in this experiment, I expressed GCaMP7 in all cell types, while in the other half GCaMP7 expression was restricted to excitatory cells. Excitatory cells are generally strongly and more sharply tuned, while inhibitory cells are typically more broadly tuned or unresponsive (Niell and Stryker, 2008). Breaking down my results into cohorts with only labelled excitatory cells and pan-neuronal GCaMP expression may reveal a difference in the fraction of cells considered tuned. As the aim of this study was to establish a method by which visual tuning properties could be compared between head fixed and freely moving sessions, these questions were not pursued but should be explored in future work.

Finally, my metric for determining visual responsivity (**Methods 2.2.10.4.1**) required that the activity of visually responsive cells be consistently greater during trials than inter-trial intervals. While this guaranteed that cells considered visually responsive indeed responded primarily to the visual stimulus (**Supp. Figure 1**), it excluded cells that showed both visual responses and off-target activity, for example due to locomotion or head movements.

4.3 Visual Tuning Properties are Less Consistent Between Consecutive Head Fixed and Freely Moving Sessions than in Repeated Head Fixed Sessions

To test the consistency of orientation and direction tuning during both head fixed and freely moving sessions, I re-identified cells found in FOVs collected from consecutive sessions conducted on the same day. ROIs were automatically re-identified in an unsupervised fashion using CaImAn, and a subset of cells manually re-identified for further analysis.

During repeated head fixed sessions, neural responses to visual stimuli and visual tuning curves were very similar, and I observed strong consistency in selectivity indices, PO, and PD. These results are expected as the time between repeated sessions was less than 30 minutes and serve as proof of principle for the VR visual stimulation method. Minor differences between sessions, like small changes in OSI or DSI values, may be explained by changes in locomotion, arousal, or behavioral or attentional state. Mice, like other mammals, display visual selective attention during tasks (Kanamori and Mrsic-Flogel, 2022; Lehnert et al., 2023; Wang and Krauzlis, 2018), and both neural responses in visual cortex and eye movements are modulated by behavioral and attentional state (McAdams and Maunsell, 1999; McGinley et al., 2015; Myers-Joseph et al., 2024; Niell and Stryker, 2010).

During repeated freely moving sessions, I observed large changes in OSI/DSI and PO/PD between sessions, with no clear trend in their magnitude. I also observed large changes in DSI and OSI during consecutive head fixed and freely moving sessions, although selectivity indices were expectedly greater during head fixed sessions than during free behavior. While PD also exhibited large and non-systematic changes between head fixed and freely moving sessions, the PO exhibited a small but consistent counterclockwise rotation during free behavior.

Eye movements and vestibular inputs may also play a role in the observed changes in PO and PD between repeated freely moving or consecutive head fixed and freely moving experiments. As previously mentioned, many theories of visual processing assume invariance in the neural representation of visual stimuli, and one example of this is the reliable perception of the visual scene in world-centric coordinates, with the gravity vector defining the vertical axis. Classical work in anesthetized cats described

over- and undershooting errors (shifts) in the orientation preference of V1 neurons with sustained side-to-side head tilt, showing that vestibular signals can at least partially compensate for head position to maintain an upright representation of the visual scene (Denney and Adorjanti, 1972; Horn and Hill, 1969), with roughly three-quarters of recorded cells exhibiting selectivity closely aligned with the head-tilt axis (Tomko et al., 1981). More recent work in macaques suggests that reflexive ocular torsion movements that compensate for head roll rotate the retina, and shift visual RFs and orientation preference in V1 (Daddaoua et al., 2014), and as previously discussed, eye and head movements in rodents have a number of modulatory effects on V1 activity. Vestibular signals are known to enter the visual system at the level of the thalamus in primates, cats, and rodents (see Keshavarzi et al. (2023) for an overview) and specifically enter rodent V1 via retrosplenial cortex (RSP) inputs to layer 6 cortico-thalamic cells (Rancz et al., 2011; Vélez-Fort et al., 2018, 2014) and via projections form the secondary motor cortex (M2) via the RSP (Guitchounts et al., 2020; Rancz et al., 2015). It is conceivable that the observed changes in orientation and direction selectivity and preference originate from a combination of signals representing gaze-stabilizing compensatory eye movements and saccadic suppression generated through gaze-shifting eye movements (Parker et al., 2023).

These compensatory effects may also explain the observed PO rotation between head fixation and free behavior. Mice have been shown to maintain head pitch parallel to the ground plane or tilted downwards by approximately 4° during normal locomotion and up to 10° while tracking prey (Holmgren et al., 2021; Meyer et al., 2018; Michaiel et al., 2020). While care was taken to maintain neutral head pitch during head fixation and to adjust the rotation of the head tracker to compensate for head bar implantation angle during free behavior, offsets in head pitch during head fixation or changes in the head pitch during free behavior due to the miniscope likely drive torsional eye rotations and eye movements that affected the rotation of the retina relative to the horizontal plane, thus changing the apparent PO.

In addition to the putative biological causes stated above, mismatches during re-identification of ROIs may contribute to the observed changes in selectivity and preference. While care was taken to manually evaluate algorithmic re-identifications, CNMF-based neural activity extraction algorithms require spatiotemporally correlated activity to define a ROI. In the FOVs I recorded with the miniscope, not all cell bodies

were readily identifiable by eye, as the imaging volume collected signals from ~200 µm in cortical depth. While the CNMF method takes temporal activity correlation into account, it is nonetheless possible that cells overlapping in depth but with different temporal activity patterns could be matched together. The CNMF method also occasionally detected blood vessels as cells, split single cells into multiple ROIs, or merged correlated but unique cells into large ROIs. During manual cell re-identification, it is also possible that cells found at different depths, but with overlapping ROIs in the X-Y plane, may be matched. Adopting new imaging methods such as those previously mentioned, together with more optimal calcium data extraction methods for 1P fluorescence data, may improve cell detection and re-identification. Deep-learning based methods optimized for extracting neuronal activity from widefield fluorescence data, such as DeepWonder (Zhang et al., 2023) are promising alternatives that may improve true cell detections while increasing computational efficiency.

4.4 Self-Motion and Postural Variables are Represented Across the V1 Population

My results corroborate previous findings that behavioral state, self-motion, and posture strongly affect activity in the visual cortex and the neocortex in general (Bouvier et al., 2020; Guitchounts et al., 2020; Keller et al., 2012; Meyer et al., 2018; Mimica et al., 2023; Miura and Scanziani, 2022; Musall et al., 2019; Niell and Stryker, 2010; Reimer et al., 2014; Saleem et al., 2013; Salkoff et al., 2020; Stringer et al., 2019; Vélez-Fort et al., 2018; Wang et al., 2023; West et al., 2022; Zagha et al., 2022). Every measured variable, encompassing running state and speed, allocentric position and orientation, and egocentric posture, was represented in the imaged V1 population.

During head fixed sessions, I observed cells with activity modulated by pupil diameter, and locomotion was also found to strongly modulate the activity of V1 neurons, regardless of arena illumination or visual stimulus presence, consistent with established results (Andermann et al., 2011; Keller et al., 2012; Niell and Stryker, 2010). Approximately 20% of V1 cells were found to be sensitive to locomotion speed during freely moving experiments, which matches the fraction of cells sensitive to planar body motion as reported by (Mimica et al., 2023). A much lower fraction (5%) of cells was found to be tuned to running speed on the running wheel during head

fixed experiments. This is unexpected, as V1 neurons recorded in head fixed mice have been previously reported to exhibit speed-dependent activity (Saleem et al., 2013). Mice exhibited a start-stop locomotion speed profile during head fixed experiments, with much of the time spent in stillness followed by bouts of high-speed running, while during freely moving sessions, the locomotion speed profile was unimodal and centered on moderate locomotion speeds (**Supp. Figure 2**). The kinematic tuning curve calculation used in this study binned neural activity based on the range of the observed kinematic variable (**Equation (*2.5*)** and Stefanini et al. (2020)). Since running wheel speeds fell into a multimodal distribution, it is likely that moderate speeds were underrepresented, while slower and higher speeds were overrepresented. A different evaluation of the range bins that ensures even numbers of samples in each bin (as in Saleem et al. (2013)) would potentially be more suitable for evaluating head fixed speed tunings.

V1 cells were tuned to the allocentric position and rotations of the mouse head and angular head velocity, as shown previously (Bouvier et al., 2020; Guitchounts et al., 2020; Meyer et al., 2018; Miura and Scanziani, 2022; Parker et al., 2023, 2022b; Rancz et al., 2015; Vélez-Fort et al., 2018). Head pitch was particularly strongly represented, more so than head roll or yaw, which exhibited similar fractions of tuned cells. This differs from data shown in Mimica et al. (2023), where head yaw was most strongly encoded in visual areas, while head pitch and roll were most strongly represented in auditory areas. One explanation for this may be the additional torque exerted by the wirefree miniscope, which may have exaggerated any up-down head movements while leaving head azimuth and roll relatively the same. Future experiments using newer, lighter miniscopes such as the NINscope or UCLA V4 miniscope (de Groot et al., 2020; Dong et al., 2022) will be better suited to examine the responses to head rotations.

During freely moving experiments, I also observed a greater similarity in the fraction of self-motion tuned cells between the experiments with visual stimuli and controls conducted in darkness than between the experiments with visual stimuli and controls in the illuminated VR arena without visual stimuli. Controls conducted in the light exhibited larger fractions of cells tuned to head position and rotations than did controls conducted in darkness, supporting reports of luminance-dependent enhancement of

neural responses during passive and active head rotations (Bouvier et al., 2020; Guitchounts et al., 2020), where V1 neurons showed increased activity during head rotations in the light, but suppression during head rotations in the dark.

The similarity in tuning to head position and rotation in the presence of drifting gratings and in the dark during freely moving sessions may partially be due to saccadic suppression. Full-field drifting grating stimuli are commonly used to study the optokinetic reflex (OKR), which is defined by biphasic eye movements – a smooth pursuit phase where the eyes track the motion of the drifting grating, and a resetting saccade phase, where rapid eye movements reset the gaze to center the eye (Purves et al., 2001). Freely moving mice exhibit saccade-and-fixate eye movements, which combined with head movements, can be categorized as either gaze-stabilizing or gaze-shifting (Meyer et al., 2018; Michaiel et al., 2020). Parker et al. (2023) demonstrated that V1 neurons preferentially respond to gaze-shifting head-eye movements, characterized by groups of cells with enhancement, suppression, or biphasic responses. Notably, cells suppressed by gaze-stabilizing movements were found in superficial V1. It is possible that during freely moving sessions, the mouse's eyes track the direction of movement of the drifting grating stimulus. Instead of resetting the eyes to the center of the visual FOV, as would be the case during a head fixed experiment, the mouse makes a gaze-shifting movement to center the head and eyes on the center of the drifting grating, resulting in suppression of V1 neurons.

To separate the effects of gaze-shifting behavior during freely-moving drifting grating stimulation from free behavior without visual stimulation, future experiments should examine head and eye movements while simultaneously recording V1 activity, as in Meyer et al. (2018) and Parker et al. (2023, 2022b), and compare activity during visual stimulus trials and the inter-trial intervals. Due to the weight of the wirefree miniscope, head bar, and tracker in my experiments, adding an additional eye tracking apparatus was not feasible.

4.5 Multimodal Representation of Visual Stimulus Features and Self-Motion in V1

To visualize the organization of visual stimulus and self-motion tuning across the V1 population, I embedded tuning vectors from each recorded cell observation into a 2D UMAP space for all cells and for cells re-identified in between consecutive head fixed and freely moving recordings. In the general population embedding, I observed distinct groups of visually tuned and self-motion tuned cells. Cells showing tuning to different self-motion variables were typically found close together in UMAP space. This was especially notable during head fixed sessions, where cells strongly tuned to running wheel speed formed two distinct groups, as did cells tuned to pupil diameter. One group of cells was highly tuned to both running wheel speed and pupil diameter and overlapped with a number of visually tuned cells, potentially reflecting a subpopulation encoding arousal state (McGinley et al., 2015; Niell and Stryker, 2010; Reimer et al., 2014). During freely moving sessions, cells tuned to mouse heading, egocentric head direction, locomotion speed, and allocentric head position and rotation generally overlapped or were found nearby one another in UMAP space, potentially reflecting a subpopulation of V1 cells sensitive to self-motion and posture.

During both head fixation and free behavior, strongly orientation or direction tuned cells formed banded patterns in UMAP space, with bands of strongly selective cells separated by a region of weakly tuned cells. In both head fixed and freely moving configurations, groups of weakly orientation selective cells largely overlapped with groups of weakly direction selective cells; however, strongly selective cells showed lesser overlap, with many strongly orientation selective cells exhibiting low direction selectivity and vice versa.

In re-identified cells, the tuning vector comprising both head fixed and freely moving variables was embedded into the same UMAP space, allowing for comparison of the visual tuning properties of these cells between head fixed and freely moving sessions. For visual variables, the UMAP embedding of re-identified cells exhibited a different grouping pattern from the general population. While the banded structure of OSI and DSI was again observed for both head fixed and freely moving configurations, cells with high OSI or DSI values largely overlapped, perhaps indicating that these were simply the most visually responsive cells, and thus easier to re-identify with CNMF-

based extraction methods. Interestingly, the location in the UMAP embedding of cells with strong OSI and DSI during the head fixed session differed from that of cells with strong OSI and DSI during the freely moving session, with only a small number of re-identified cells exhibiting strong tuning in both sessions. This could be a state-dependent result or arise from eye-movement related artifacts, as previously discussed.

In both the general and re-identified populations, groups of cells strongly tuned to visual variables typically did not overlap with groups of cells exhibiting strong tuning to self-motion or posture, while cells with weak tuning to any variable exhibited more overlap. These results may be explained in the framework of mixed selectivity (Fusi et al., 2016; Tye et al., 2024), which posits that some neurons represent multiple variables simultaneously and in a context dependent manner. This complexity is thought to help the neural population increase the separability of different task-related variables, allowing for greater computation flexibility and power. In the context of the work presented here, this could mean that while some layer 2/3 V1 neurons are exclusively and strongly tuned to visual features or to one self-motion variable, the majority are sensitive to both visual stimulus features and self-motion. This type of signal interaction is reminiscent of predictive coding models of visual processing (Keller and Mrsic-Flogel, 2018), where efference copies of motor commands are used to generate top-down predictions about the effects of self-motion on sensory inputs, and mismatch signals are used for bottom-up comparisons between sensory input and the predicted input. By mixing bottom-up visual inputs with top-down self-motion related signals, V1 could already produce a representational space that provides the visual system with information about the movement of the head and body in relation to a visual stimulus, allowing for better visual processing during bouts of self-motion.

From the data presented here, it is not possible to determine how the mixed selectivity and predictive processing models interact to explain the overlap in visual and self-motion representations. Further work, such as modelling the neural response to the visual stimulus and self-motion, is needed to disentangle how cells are multiplexing visual and self-motion information. In particular, approaches that can separate linear and non-linear contributions of variables in the model, such as the one presented by Costabile et al. (2023), are well suited to model the contributions of different sensory and motion-related variables.

4.6 Conclusions and Future Directions

The work presented in this thesis developed a method to examine the interaction of visual stimulus representation and self-motion in the freely moving mouse and presents the first descriptions of direction and orientation selectivity during free behavior. Two main conclusions were reached:

1. Tuning to self-motion and posture is present across the V1 population, with many cells exhibiting tuning to both visual and self-motion variables, strengthening the view that the neocortex inherently represents multisensory and sensorimotor information.
2. Orientation and direction tuning are measurable during both head fixed and freely moving experiments. Orientation and direction selectivity indices and preferred direction are variable between consecutive head fixed and freely moving sessions, but preferred orientation exhibits correlated counterclockwise offsets.

This thesis corroborates many findings from previous literature, like the representation of signals driven by head and eye movements, locomotion, and posture in V1, and for the first time describes orientation and direction selectivity in the freely moving mouse. However, this work is primarily descriptive and does not causally show how such signals are integrated during free behavior. An improved description of visual stimulus tuning could be achieved by coupling longer recordings (for example with wired miniscopes) with more stimulus presentations and eye tracking, similar to Parker et al. (2022b). By both controlling the visual stimulus and recording eye movements, a full visual scene reconstruction would allow for simultaneous RF mapping and evaluations of orientation or direction preference. The VR system can also be easily extended to test spatial and temporal frequency tuning under the same conditions.

To further disambiguate the contributions of visual stimulus driven activity and self-motion representations in V1, opto- or chemogenetic manipulation studies, like silencing the RSP to V1 layer 6 projection during active viewing of drifting gratings in VR, could decouple how vestibular inputs and eye movements influence V1 activity during free behavior. A more technically involved option would be to utilize all-optical interrogation methods like holography (Emiliani et al., 2015; Russell et al., 2022;

Zhang et al., 2022, 2018), for example by using a mini-2P (Zong et al., 2022) or mini-3P (Klioutchnikov et al., 2023; Zhao et al., 2023) system, to selectively activate or inactivate cells that show tuning to particular self-motion variables and observe the corresponding changes to behavior.

An exciting future direction would be to characterize the tuning properties of V1 cells systematically during head fixed and free behavior and see how those cells later contribute to naturalistic behaviors like prey capture. Work in the mouse SC has shown that wide-field and narrow-field neurons contribute differently to prey capture behavior based on their known visual stimulus preferences (Hoy et al., 2019), and mice have been shown to keep prey in the part of the visual field with the least optic flow (Holmgren et al., 2021). Perhaps V1 neurons tuned to particular spatial or temporal frequencies, or stimulus direction or orientation, differentially contribute to prey localization and capture, or have responses preferentially enhanced during prey capture bouts.

References

1. Ahmadlou M, Heimel JA. 2015. Preference for concentric orientations in the mouse superior colliculus. Nat Commun 6:6773. doi:10.1038/ncomms7773
2. Akerboom J, Chen T-W, Wardill TJ, Tian L, Marvin JS, Mutlu S, Calderón NC, Esposti F, Borghuis BG, Sun XR, Gordus A, Orger MB, Portugues R, Engert F, Macklin JJ, Filosa A, Aggarwal A, Kerr RA, Takagi R, Kracun S, Shigetomi E, Khakh BS, Baier H, Lagnado L, Wang SS-H, Bargmann CI, Kimmel BE, Jayaraman V, Svoboda K, Kim DS, Schreiter ER, Looger LL. 2012. Optimization of a GCaMP Calcium Indicator for Neural Activity Imaging. J Neurosci 32:13819–13840. doi:10.1523/JNEUROSCI.2601-12.2012
3. Akerboom J, Rivera JDV, Guilbe MMR, Malavé ECA, Hernandez HH, Tian L, Hires SA, Marvin JS, Looger LL, Schreiter ER. 2009. Crystal Structures of the GCaMP Calcium Sensor Reveal the Mechanism of Fluorescence Signal Change and Aid Rational Design. J Biol Chem 284:6455–6464. doi:10.1074/jbc.M807657200
4. Andermann ML, Kerlin AM, Roumis DK, Glickfeld LL, Reid RC. 2011. Functional Specialization of Mouse Higher Visual Cortical Areas. Neuron 72:1025–1039. doi:10.1016/j.neuron.2011.11.013
5. Antonini A, Fagiolini M, Stryker MP. 1999. Anatomical Correlates of Functional Plasticity in Mouse Visual Cortex. J Neurosci 19:4388–4406. doi:10.1523/JNEUROSCI.19-11-04388.1999
6. Aoki R, Tsubota T, Goya Y, Benucci A. 2017. An automated platform for high-throughput mouse behavior and physiology with voluntary head-fixation. Nat Commun 8:1196. doi:10.1038/s41467-017-01371-0
7. Ayaz A, Saleem AB, Schölvinck ML, Carandini M. 2013. Locomotion Controls Spatial Integration in Mouse Visual Cortex. Curr Biol 23:890–894. doi:10.1016/j.cub.2013.04.012
8. Aydın Ç, Couto J, Giugliano M, Farrow K, Bonin V. 2018. Locomotion modulates specific functional cell types in the mouse visual thalamus. Nat Commun 9:4882. doi:10.1038/s41467-018-06780-3
9. Barlow HB, Hill RM, Levick WR. 1964. Retinal ganglion cells responding selectively to direction and speed of image motion in the rabbit. J Physiol 173:377–407.
10. Bauer J, Simon Weiler, Weiler S, Martin H. P. Fernholz, Fernholz MHP, David Laubender, Laubender D, Volker Scheuss, Scheuss V, Mark Hübener, Hübener M, Tobias Bonhoeffer, Bonhoeffer T, Tobias Rose, Rose T. 2021. Limited functional convergence of eye-specific inputs in the retinogeniculate pathway of the mouse. Neuron 109. doi:10.1016/j.neuron.2021.05.036
11. Beetz MJ. 2024. A perspective on neuroethology: what the past teaches us about the future of neuroethology. J Comp Physiol A 210:325–346. doi:10.1007/s00359-024-01695-5
12. Benavidez NL, Bienkowski MS, Zhu M, Garcia LH, Fayzullina M, Gao L, Bowman I, Gou L, Khanjani N, Cotter KR, Korobkova L, Becerra M, Cao C, Song MY, Zhang B, Yamashita S, Tugangui AJ, Zingg B, Rose K, Lo D, Foster NN, Boesen T, Mun H-S, Aquino S, Wickersham IR, Ascoli GA, Hintiryan H, Dong H-W. 2021. Organization of the inputs and outputs of the mouse superior colliculus. Nat Commun 12:4004. doi:10.1038/s41467-021-24241-2
13. Berens P. 2009. CircStat: A MATLAB Toolbox for Circular Statistics. J Stat Softw 31. doi:10.18637/jss.v031.i10
14. Blakemore C, Tobin EA. 1972. Lateral inhibition between orientation detectors in the cat's visual cortex. Exp Brain Res 15:439–440. doi:10.1007/BF00234129
15. Blanchard RJ, Hebert MA, Ferrari P, Palanza P, Figueira R, Blanchard DC, Parmigiani S. 1998. Defensive behaviors in wild and laboratory (Swiss) mice: the mouse defense test battery. Physiol Behav 65:201–209. doi:10.1016/S0031-9384(98)00012-2
16. Bleckert A, Schwartz GW, Turner MH, Rieke F, Wong ROL. 2014. Visual Space Is Represented by Nonmatching Topographies of Distinct Mouse Retinal Ganglion Cell Types. Curr Biol 24:310–315. doi:10.1016/j.cub.2013.12.020
17. Bonhoeffer T, Grinvald A. 1991. Iso-orientation domains in cat visual cortex are arranged in pinwheel-like patterns. Nature 353:429–431. doi:10.1038/353429a0
18. Bonhoeffer T, Hübener M. 2016. Intrinsic Optical Imaging of Functional Map Development in Mammalian Visual Cortex. Cold Spring Harb Protoc 2016:pdb.top089383. doi:10.1101/pdb.top089383

19. Boone HC, Samonds JM, Crouse EC, Barr C, Priebe NJ, McGee AW. 2021. Natural binocular depth discrimination behavior in mice explained by visual cortical activity. Curr Biol 31:2191-2198.e3. doi:10.1016/j.cub.2021.02.031
20. Born G, Schneider-Soupiadis FA, Erisken S, Vaiceliunaite A, Lao CL, Mobarhan MH, Spacek MA, Einevoll GT, Busse L. 2021. Corticothalamic feedback sculpts visual spatial integration in mouse thalamus. Nat Neurosci 24:1711–1720. doi:10.1038/s41593-021-00943-0
21. Bouvier G, Senzai Y, Scanziani M. 2020. Head Movements Control the Activity of Primary Visual Cortex in a Luminance-Dependent Manner. Neuron 108:500-511.e5. doi:10.1016/j.neuron.2020.07.004
22. Brainard DH. 1997. The Psychophysics Toolbox. Spat Vis 10:433–436. doi:10.1163/156856897X00357
23. Busse L, Cardin JA, Chiappe ME, Halassa MM, McGinley MJ, Yamashita T, Saleem AB. 2017. Sensation during Active Behaviors. J Neurosci 37:10826–10834. doi:10.1523/JNEUROSCI.1828-17.2017
24. Butts DA, Weng C, Jin J, Yeh C-I, Lesica NA, Alonso J-M, Stanley GB. 2007. Temporal precision in the neural code and the timescales of natural vision. Nature 449:92–95. doi:10.1038/nature06105
25. Campagner D, Vale R, Tan YL, Iordanidou P, Pavón Arocas O, Claudi F, Stempel AV, Keshavarzi S, Petersen RS, Margrie TW, Branco T. 2023. A cortico-collicular circuit for orienting to shelter during escape. Nature 613:111–119. doi:10.1038/s41586-022-05553-9
26. Campbell FW, Green DG. 1965. Monocular versus Binocular Visual Acuity. Nature 208:191–192. doi:10.1038/208191a0
27. Chen Y, Jang H, Spratt PWE, Kosar S, Taylor DE, Essner RA, Bai L, Leib DE, Kuo T-W, Lin Y-C, Patel M, Subkhangulova A, Kato S, Feinberg EH, Bender KJ, Knight ZA, Garrison JL. 2020. Soma-Targeted Imaging of Neural Circuits by Ribosome Tethering. Neuron 107:454-469.e6. doi:10.1016/j.neuron.2020.05.005
28. Cheong SK, Tailby C, Solomon SG, Martin PR. 2013. Cortical-Like Receptive Fields in the Lateral Geniculate Nucleus of Marmoset Monkeys. J Neurosci 33:6864–6876. doi:10.1523/JNEUROSCI.5208-12.2013
29. Clark BJ, Hamilton DA, Whishaw IQ. 2006. Motor activity (exploration) and formation of home bases in mice (C57BL/6) influenced by visual and tactile cues: Modification of movement distribution, distance, location, and speed. Physiol Behav 87:805–816. doi:10.1016/j.physbeh.2006.01.026
30. Costabile JD, Balakrishnan KA, Schwinn S, Haesemeyer M. 2023. Model discovery to link neural activity to behavioral tasks. eLife 12:e83289. doi:https://doi.org/10.7554/eLife.83289
31. Cruz-Martín A, El-Danaf RN, Osakada F, Sriram B, Dhande OS, Nguyen PL, Callaway EM, Ghosh A, Huberman AD. 2014. A dedicated circuit links direction-selective retinal ganglion cells to the primary visual cortex. Nature 507:358–361. doi:10.1038/nature12989
32. Daddaoua N, Dicke PW, Thier P. 2014. Eye position information is used to compensate the consequences of ocular torsion on V1 receptive fields. Nat Commun 5:3047. doi:10.1038/ncomms4047
33. Daniel PM, Whitteridge D. 1961. The representation of the visual field on the cerebral cortex in monkeys. J Physiol 159:203–221.
34. de Groot A, van den Boom BJ, van Genderen RM, Coppens J, van Veldhuijzen J, Bos J, Hoedemaker H, Negrello M, Willuhn I, De Zeeuw CI, Hoogland TM. 2020. NINscope, a versatile miniscope for multi-region circuit investigations. eLife 9:e49987. doi:10.7554/eLife.49987
35. De Franceschi G, Vivattanasarn T, Saleem AB, Solomon SG. 2016. Vision Guides Selection of Freeze or Flight Defense Strategies in Mice. Curr Biol 26:2150–2154. doi:10.1016/j.cub.2016.06.006
36. Del Grosso NA, Graboski JJ, Chen W, Hernández EB, Sirota A. 2017. Virtual Reality system for freely-moving rodents. bioRxiv. doi:10.1101/161232
37. Del Grosso NA, Sirota A. 2019. Ratcave: A 3D graphics python package for cognitive psychology experiments. Behav Res Methods 51:2085–2093. doi:10.3758/s13428-019-01245-x
38. Deneux T, Harrell ER, Kempf A, Ceballo S, Filipchuk A, Bathellier B. 2019. Context-dependent signaling of coincident auditory and visual events in primary visual cortex. eLife 8:e44006. doi:10.7554/eLife.44006
39. Denk W, Strickler JH, Webb WW. 1990. Two-Photon Laser Scanning Fluorescence Microscopy. Science 248:73–76. doi:10.1126/science.2321027

References

40. Denney D, Adorjanti C. 1972. Orientation specificity of visual cortical neurons after head tilt. Exp Brain Res 14:312–317. doi:10.1007/BF00816165
41. Diamanti EM, Reddy CB, Schröder S, Muzzu T, Harris KD, Saleem AB, Carandini M. 2021. Spatial modulation of visual responses arises in cortex with active navigation. eLife 10:e63705. doi:10.7554/eLife.63705
42. DiCarlo JJ, Zoccolan D, Rust NC. 2012. How Does the Brain Solve Visual Object Recognition? Neuron 73:415–434. doi:10.1016/j.neuron.2012.01.010
43. Dimitrov D, He Y, Mutoh H, Baker BJ, Cohen L, Akemann W, Knöpfel T. 2007. Engineering and Characterization of an Enhanced Fluorescent Protein Voltage Sensor. PLOS ONE 2:e440. doi:10.1371/journal.pone.0000440
44. Dinarvand M, Neubert E, Meyer D, Selvaggio G, Mann FA, Erpenbeck L, Kruss S. 2019. Near-Infrared Imaging of Serotonin Release from Cells with Fluorescent Nanosensors. Nano Lett 19:6604–6611. doi:10.1021/acs.nanolett.9b02865
45. Dombeck DA, Harvey CD, Tian L, Looger LL, Tank DW. 2010. Functional imaging of hippocampal place cells at cellular resolution during virtual navigation. Nat Neurosci 13:1433–1440. doi:10.1038/nn.2648
46. Dong Z, Mau W, Feng Y, Pennington ZT, Chen L, Zaki Y, Rajan K, Shuman T, Aharoni D, Cai DJ. 2022. Minian, an open-source miniscope analysis pipeline. eLife 11:e70661. doi:10.7554/eLife.70661
47. Douglas RJ, Martin KA. 1991. A functional microcircuit for cat visual cortex. J Physiol 440:735–769. doi:10.1113/jphysiol.1991.sp018733
48. Douglas RJ, Martin KAC. 2004. Neuronal Circuits of the Neocortex. Annu Rev Neurosci 27:419–451. doi:10.1146/annurev.neuro.27.070203.144152
49. Douglas RJ, Martin KAC, Whitteridge D. 1989. A Canonical Microcircuit for Neocortex. Neural Comput 1:480–488. doi:10.1162/neco.1989.1.4.480
50. Dräger UC. 1978. Observations on monocular deprivation in mice. J Neurophysiol 41:28–42. doi:10.1152/jn.1978.41.1.28
51. Dräger UC. 1975. Receptive fields of single cells and topography in mouse visual cortex. J Comp Neurol 160:269–289. doi:10.1002/cne.901600302
52. Dräger UC, Hubel DH. 1976. Topography of visual and somatosensory projections to mouse superior colliculus. J Neurophysiol 39:91–101. doi:10.1152/jn.1976.39.1.91
53. Dräger UC, Hubel DH. 1975a. Responses to visual stimulation and relationship between visual, auditory, and somatosensory inputs in mouse superior colliculus. J Neurophysiol 38:690–713. doi:10.1152/jn.1975.38.3.690
54. Dräger UC, Hubel DH. 1975b. Physiology of visual cells in mouse superior colliculus and correlation with somatosensory and auditory input. Nature 253:203–204. doi:10.1038/253203a0
55. Dräger UC, Olsen JF. 1981. Ganglion cell distribution in the retina of the mouse. Invest Ophthalmol Vis Sci 20:285–293.
56. Dräger UC, Olsen JF. 1980. Origins of crossed and uncrossed retinal projections in pigmented and albino mice. J Comp Neurol 191:383–412. doi:10.1002/cne.901910306
57. Durand S, Iyer R, Mizuseki K, Vries S de, Mihalas S, Reid RC. 2016. A Comparison of Visual Response Properties in the Lateral Geniculate Nucleus and Primary Visual Cortex of Awake and Anesthetized Mice. J Neurosci 36:12144–12156. doi:10.1523/JNEUROSCI.1741-16.2016
58. Ellis EM, Gauvain G, Sivyer B, Murphy GJ. 2016. Shared and distinct retinal input to the mouse superior colliculus and dorsal lateral geniculate nucleus. J Neurophysiol 116:602–610. doi:10.1152/jn.00227.2016
59. Emiliani V, Cohen AE, Deisseroth K, Häusser M. 2015. All-Optical Interrogation of Neural Circuits. J Neurosci 35:13917–13926. doi:10.1523/JNEUROSCI.2916-15.2015
60. Erisken S, Vaiceliunaite A, Jurjut O, Fiorini M, Katzner S, Busse L. 2014. Effects of Locomotion Extend throughout the Mouse Early Visual System. Curr Biol 24:2899–2907. doi:10.1016/j.cub.2014.10.045
61. Erofeev AI, Vinokurov EK, Vlasova OL, Bezprozvanny IB. 2023. GCaMP, a Family of Single-Fluorophore Genetically Encoded Calcium Indicators. J Evol Biochem Physiol 59:1195–1214. doi:10.1134/S0022093023040142
62. Fahey PG, Muhammad T, Smith C, Froudarakis E, Cobos E, Fu J, Walker EY, Yatsenko D, Sinz FH, Reimer J, Tolias AS. 2019. A global map of orientation tuning in mouse visual cortex. bioRxiv 745323. doi:10.1101/745323
63. Feinberg EH, Meister M. 2015. Orientation columns in the mouse superior colliculus. Nature 519:229–232. doi:10.1038/nature14103

64. Felleman DJ, Van Essen DC. 1991. Distributed Hierarchical Processing in the Primate Cerebral Cortex. Cereb Cortex 1:1–47. doi:10.1093/cercor/1.1.1-a
65. Fink AJ, Axel R, Schoonover CE. 2019. A virtual burrow assay for head–fixed mice measures habituation, discrimination, exploration and avoidance without training. eLife 8:e45658. doi:10.7554/eLife.45658
66. Fiser A, Mahringer D, Oyibo HK, Petersen AV, Leinweber M, Keller GB. 2016. Experience-dependent spatial expectations in mouse visual cortex. Nat Neurosci 19:1658–1664. doi:10.1038/nn.4385
67. Fournier J, Saleem AB, Diamanti EM, Wells MJ, Harris KD, Carandini M. 2020. Mouse Visual Cortex Is Modulated by Distance Traveled and by Theta Oscillations. Curr Biol 30:3811-3817.e6. doi:10.1016/j.cub.2020.07.006
68. Fox MW. 1965. The visual cliff test for the study of visual depth perception in the mouse. Anim Behav 13:232-IN3. doi:10.1016/0003-3472(65)90040-0
69. Froudarakis E, Fahey PG, Reimer J, Smirnakis SM, Tehovnik EJ, Tolias AS. 2019. The Visual Cortex in Context. Annu Rev Vis Sci 5:317–339. doi:10.1146/annurev-vision-091517-034407
70. Fusi S, Miller EK, Rigotti M. 2016. Why neurons mix: high dimensionality for higher cognition. Curr Opin Neurobiol 37:66–74. doi:10.1016/j.conb.2016.01.010
71. Gale SD, Murphy GJ. 2014. Distinct Representation and Distribution of Visual Information by Specific Cell Types in Mouse Superficial Superior Colliculus. J Neurosci 34:13458–13471. doi:10.1523/JNEUROSCI.2768-14.2014
72. Garrett ME, Nauhaus I, Marshel JH, Callaway EM. 2014. Topography and Areal Organization of Mouse Visual Cortex. J Neurosci 34:12587–12600. doi:10.1523/JNEUROSCI.1124-14.2014
73. Ghosh KK, Burns LD, Cocker ED, Nimmerjahn A, Ziv Y, Gamal AE, Schnitzer MJ. 2011. Miniaturized integration of a fluorescence microscope. Nat Methods 8:871–878. doi:10.1038/nmeth.1694
74. Gianfranceschi L, Fiorentini A, Maffei L. 1999. Behavioural visual acuity of wild type and bcl2 transgenic mouse. Vision Res 39:569–574. doi:10.1016/S0042-6989(98)00169-2
75. Gilbert CD, Wiesel TN. 1990. The influence of contextual stimuli on the orientation selectivity of cells in primary visual cortex of the cat. Vision Res, Optics Physiology and Vision 30:1689–1701. doi:10.1016/0042-6989(90)90153-C
76. Giovannucci A, Friedrich J, Gunn P, Kalfon J, Brown BL, Koay SA, Taxidis J, Najafi F, Gauthier JL, Zhou P, Khakh BS, Tank DW, Chklovskii DB, Pnevmatikakis EA. 2019. CaImAn an open source tool for scalable calcium imaging data analysis. eLife 8:e38173. doi:10.7554/eLife.38173
77. Glickfeld Lindsey L, Andermann ML, Bonin V, Reid RC. 2013. Cortico-cortical projections in mouse visual cortex are functionally target specific. Nat Neurosci 16:219–226. doi:10.1038/nn.3300
78. Glickfeld L. L., Histed MH, Maunsell JHR. 2013. Mouse Primary Visual Cortex Is Used to Detect Both Orientation and Contrast Changes. J Neurosci 33:19416–19422. doi:10.1523/JNEUROSCI.3560-13.2013
79. Glickfeld LL, Olsen SR. 2017. Higher-Order Areas of the Mouse Visual Cortex. Annu Rev Vis Sci 3:251–273. doi:10.1146/annurev-vision-102016-061331
80. Goard MJ, Pho GN, Woodson J, Sur M. 2016. Distinct roles of visual, parietal, and frontal motor cortices in memory-guided sensorimotor decisions. eLife 5:e13764. doi:10.7554/eLife.13764
81. Goltstein PM, Reinert S, Bonhoeffer T, Hübener M. 2021. Mouse visual cortex areas represent perceptual and semantic features of learned visual categories. Nat Neurosci 24:1441–1451. doi:10.1038/s41593-021-00914-5
82. Göppert-Mayer M. 1931. Über Elementarakte mit zwei Quantensprüngen. Ann Phys 401:273–294. doi:10.1002/andp.19314010303
83. Gordon JA, Stryker MP. 1996. Experience-Dependent Plasticity of Binocular Responses in the Primary Visual Cortex of the Mouse. J Neurosci 16:3274–3286. doi:10.1523/JNEUROSCI.16-10-03274.1996
84. Granlund GH. 1978. In search of a general picture processing operator. Comput Graph Image Process 8:155–173. doi:10.1016/0146-664X(78)90047-3
85. Greene N. 1986. Environment Mapping and Other Applications of World Projections. IEEE Comput Graph Appl 6:21–29. doi:10.1109/MCG.1986.276658
86. Grienberger C, Konnerth A. 2012. Imaging Calcium in Neurons. Neuron 73:862–885. doi:10.1016/j.neuron.2012.02.011

87. Grubb MS, Thompson ID. 2003. Quantitative Characterization of Visual Response Properties in the Mouse Dorsal Lateral Geniculate Nucleus. J Neurophysiol 90:3594–3607. doi:10.1152/jn.00699.2003
88. Guggiana Nilo D, McCann MK, Bonhoeffer T, Hübener M. in preparation. Nonlinear mixed selectivity contributes to stimulus encoding in V1 during mouse prey capture.
89. Guitchounts G, Masís J, Wolff SBE, Cox D. 2020. Encoding of 3D Head Orienting Movements in the Primary Visual Cortex. Neuron 108:512-525.e4. doi:10.1016/j.neuron.2020.07.014
90. Haggerty DC, Ji D. 2015. Activities of visual cortical and hippocampal neurons co-fluctuate in freely moving rats during spatial behavior. eLife 4:e08902. doi:10.7554/eLife.08902
91. Han W, Tellez LA, Rangel MJ, Motta SC, Zhang X, Perez IO, Canteras NS, Shammah-Lagnado SJ, van den Pol AN, de Araujo IE. 2017. Integrated Control of Predatory Hunting by the Central Nucleus of the Amygdala. Cell 168:311-324.e18. doi:10.1016/j.cell.2016.12.027
92. Harris CR, Millman KJ, van der Walt SJ, Gommers R, Virtanen P, Cournapeau D, Wieser E, Taylor J, Berg S, Smith NJ, Kern R, Picus M, Hoyer S, van Kerkwijk MH, Brett M, Haldane A, del Río JF, Wiebe M, Peterson P, Gérard-Marchant P, Sheppard K, Reddy T, Weckesser W, Abbasi H, Gohlke C, Oliphant TE. 2020. Array programming with NumPy. Nature 585:357–362. doi:10.1038/s41586-020-2649-2
93. Harris KD, Shepherd GMG. 2015. The neocortical circuit: themes and variations. Nat Neurosci 18:170–181. doi:10.1038/nn.3917
94. Hartline HK. 1969. Visual Receptors and Retinal Interaction. Science 164:270–278. doi:10.1126/science.164.3877.270
95. Hartline HK. 1938. The response of single optic nerve fibers of the vertebrate eye to illumination of the retina. Am J Physiol-Leg Content 121:400–415. doi:10.1152/ajplegacy.1938.121.2.400
96. Harvey CD, Collman F, Dombeck DA, Tank DW. 2009. Intracellular dynamics of hippocampal place cells during virtual navigation. Nature 461:941–946. doi:10.1038/nature08499
97. Hassenstein B, Reichardt W. 1956. Systemtheoretische Analyse der Zeit-, Reihenfolgen- und Vorzeichenauswertung bei der Bewegungsperzeption des Rüsselkäfers Chlorophanus. Z Für Naturforschung B 11:513–524. doi:10.1515/znb-1956-9-1004
98. Havenith MN, Zijderveld PM, van Heukelum S, Abghari S, Glennon JC, Tiesinga P. 2018. The Virtual-Environment-Foraging Task enables rapid training and single-trial metrics of attention in head-fixed mice. Sci Rep 8:17371. doi:10.1038/s41598-018-34966-8
99. Hell SW, Bahlmann K, Schrader M, Soini A, Malak HM, Gryczynski I, Lakowicz JR. 1996. Three-photon excitation in fluorescence microscopy. J Biomed Opt 1:71–74. doi:10.1117/12.229062
100. Helmchen F, Fee MS, Tank DW, Denk W. 2001. A Miniature Head-Mounted Two-Photon Microscope: High-Resolution Brain Imaging in Freely Moving Animals. Neuron 31:903–912. doi:10.1016/S0896-6273(01)00421-4
101. Herrington TM, Masse NY, Hachmeh KJ, Smith JET, Assad JA, Cook EP. 2009. The Effect of Microsaccades on the Correlation between Neural Activity and Behavior in Middle Temporal, Ventral Intraparietal, and Lateral Intraparietal Areas. J Neurosci 29:5793–5805. doi:10.1523/JNEUROSCI.4412-08.2009
102. Hires SA, Zhu Y, Tsien RY. 2008. Optical measurement of synaptic glutamate spillover and reuptake by linker optimized glutamate-sensitive fluorescent reporters. Proc Natl Acad Sci 105:4411–4416. doi:10.1073/pnas.0712008105
103. Hoffmann S, Beetz MJ, Stöckl A, Mesce KA. 2023. Editorial: Naturalistic neuroscience — Towards a full cycle from lab to field. Front Neural Circuits 17. doi:10.3389/fncir.2023.1251771
104. Holmgren CD, Stahr P, Wallace DJ, Voit K-M, Matheson EJ, Sawinski J, Bassetto G, Kerr JN. 2021. Visual pursuit behavior in mice maintains the pursued prey on the retinal region with least optic flow. eLife 10:e70838. doi:10.7554/eLife.70838
105. Hölscher C, Schnee A, Dahmen H, Setia L, Mallot HA. 2005. Rats are able to navigate in virtual environments. J Exp Biol 208:561–569. doi:10.1242/jeb.01371
106. Horn G, Hill RM. 1969. Modifications of Receptive Fields of Cells in the Visual Cortex occurring Spontaneously and associated with Bodily Tilt. Nature 221:186–188. doi:10.1038/221186a0
107. Hoy JL, Bishop HI, Niell CM. 2019. Defined Cell Types in Superior Colliculus Make Distinct Contributions to Prey Capture Behavior in the Mouse. Curr Biol 29:4130-4138.e5. doi:10.1016/j.cub.2019.10.017

108. Hoy JL, Yavorska I, Wehr M, Niell CM. 2016. Vision Drives Accurate Approach Behavior during Prey Capture in Laboratory Mice. Curr Biol 26:3046–3052. doi:10.1016/j.cub.2016.09.009
109. Huang K-H, Rupprecht P, Frank T, Kawakami K, Bouwmeester T, Friedrich RW. 2020. A virtual reality system to analyze neural activity and behavior in adult zebrafish. Nat Methods 17:343–351. doi:10.1038/s41592-020-0759-2
110. Hubel DH, Wiesel TN. 1972. Laminar and columnar distribution of geniculo-cortical fibers in the macaque monkey. J Comp Neurol 146:421–450. doi:10.1002/cne.901460402
111. Hubel DH, Wiesel TN. 1968. Receptive fields and functional architecture of monkey striate cortex. J Physiol 195:215–243. doi:10.1113/jphysiol.1968.sp008455
112. Hubel DH, Wiesel TN. 1962. Receptive fields, binocular interaction and functional architecture in the cat's visual cortex. J Physiol 160:106–154. doi:10.1113/jphysiol.1962.sp006837
113. Hubel DH, Wiesel TN. 1959. Receptive fields of single neurones in the cat's striate cortex. J Physiol 148:574–591. doi:10.1113/jphysiol.1959.sp006308
114. Hubel DH, Wiesel TN, Stryker MP. 1977. Orientation columns in macaque monkey visual cortex demonstrated by the 2-deoxyglucose autoradiographic technique. Nature 269:328–330. doi:10.1038/269328a0
115. Hübener M. 2003. Mouse visual cortex. Curr Opin Neurobiol 13:413–420. doi:10.1016/S0959-4388(03)00102-8
116. Huberman AD, Niell CM. 2011. What can mice tell us about how vision works? Trends Neurosci 34:464–473. doi:10.1016/j.tins.2011.07.002
117. Huh CYL, Abdelaal K, Salinas KJ, Gu D, Zeitoun J, Velez DXF, Peach JP, Fowlkes CC, Gandhi SP. 2020. Long-term Monocular Deprivation during Juvenile Critical Period Disrupts Binocular Integration in Mouse Visual Thalamus. J Neurosci 40:585–604. doi:10.1523/JNEUROSCI.1626-19.2019
118. Ibrahim LA, Mesik L, Ji X, Fang Q, Li H, Li Y, Zingg B, Zhang LI, Tao HW. 2016. Cross-Modality Sharpening of Visual Cortical Processing through Layer-1-Mediated Inhibition and Disinhibition. Neuron 89:1031–1045. doi:10.1016/j.neuron.2016.01.027
119. Isaacson M, Chang H, Berkowitz L, Zirkel R, Park Y, Hu D, Ellwood I, Schaffer C. 2023. MouseGoggles: an immersive virtual reality headset for mouse neuroscience and behavior. doi:10.21203/rs.3.rs-3301474/v1
120. Iurilli G, Ghezzi D, Olcese U, Lassi G, Nazzaro C, Tonini R, Tucci V, Benfenati F, Medini P. 2012. Sound-Driven Synaptic Inhibition in Primary Visual Cortex. Neuron 73:814–828. doi:10.1016/j.neuron.2011.12.026
121. Jackman SL, Chen CH, Chettih SN, Neufeld SQ, Drew IR, Agba CK, Flaquer I, Stefano AN, Kennedy TJ, Belinsky JE, Roberston K, Beron CC, Sabatini BL, Harvey CD, Regehr WG. 2018. Silk Fibroin Films Facilitate Single-Step Targeted Expression of Optogenetic Proteins. Cell Rep 22:3351–3361. doi:10.1016/j.celrep.2018.02.081
122. Jaepel J, Hübener M, Bonhoeffer T, Rose T. 2017. Lateral geniculate neurons projecting to primary visual cortex show ocular dominance plasticity in adult mice. Nat Neurosci 20:1708–1714. doi:10.1038/s41593-017-0021-0
123. Ji D, Wilson MA. 2007. Coordinated memory replay in the visual cortex and hippocampus during sleep. Nat Neurosci 10:100–107. doi:10.1038/nn1825
124. Jiang X, Shen S, Cadwell CR, Berens P, Sinz F, Ecker AS, Patel S, Tolias AS. 2015. Principles of connectivity among morphologically defined cell types in adult neocortex. Science 350:aac9462. doi:10.1126/science.aac9462
125. Johnson KP, Fitzpatrick MJ, Zhao L, Wang B, McCracken S, Williams PR, Kerschensteiner D. 2021. Cell-type-specific binocular vision guides predation in mice. Neuron 109:1527-1539.e4. doi:10.1016/j.neuron.2021.03.010
126. Joshi S, Li Y, Kalwani RM, Gold JI. 2016. Relationships between Pupil Diameter and Neuronal Activity in the Locus Coeruleus, Colliculi, and Cingulate Cortex. Neuron 89:221–234. doi:10.1016/j.neuron.2015.11.028
127. Juczewski K, Koussa JA, Kesner AJ, Lee JO, Lovinger DM. 2020. Stress and behavioral correlates in the head-fixed method: stress measurements, habituation dynamics, locomotion, and motor-skill learning in mice. Sci Rep 10:12245. doi:10.1038/s41598-020-69132-6
128. Jun JJ, Steinmetz NA, Siegle JH, Denman DJ, Bauza M, Barbarits B, Lee AK, Anastassiou CA, Andrei A, Aydın Ç, Barbic M, Blanche TJ, Bonin V, Couto J, Dutta B, Gratiy SL, Gutnisky DA, Häusser M, Karsh B, Ledochowitsch P, Lopez CM, Mitelut C, Musa S, Okun M, Pachitariu M, Putzeys J, Rich PD, Rossant C, Sun W, Svoboda K, Carandini M, Harris KD, Koch C,

O'Keefe J, Harris TD. 2017. Fully integrated silicon probes for high-density recording of neural activity. Nature 551:232–236. doi:10.1038/nature24636
129. Kanamori T, Mrsic-Flogel TD. 2022. Independent response modulation of visual cortical neurons by attentional and behavioral states. Neuron 110:3907-3918.e6. doi:10.1016/j.neuron.2022.08.028
130. Kasper EM, Larkman AU, Lübke J, Blakemore C. 1994. Pyramidal neurons in layer 5 of the rat visual cortex. II. Development of electrophysiological properties. J Comp Neurol 339:475–494. doi:10.1002/cne.903390403
131. Keller AJ, Houlton R, Kampa BM, Lesica NA, Mrsic-Flogel TD, Keller GB, Helmchen F. 2017. Stimulus relevance modulates contrast adaptation in visual cortex. eLife 6. doi:10.7554/eLife.21589
132. Keller GB, Bonhoeffer T, Hübener M. 2012. Sensorimotor Mismatch Signals in Primary Visual Cortex of the Behaving Mouse. Neuron 74:809–815. doi:10.1016/j.neuron.2012.03.040
133. Keller GB, Mrsic-Flogel TD. 2018. Predictive Processing: A Canonical Cortical Computation. Neuron 100:424–435. doi:10.1016/j.neuron.2018.10.003
134. Keshavarzi S, Vélez-Fort M, Margrie TW. 2023. Cortical Integration of Vestibular and Visual Cues for Navigation, Visual Processing, and Perception 46:301–320. doi:10.1146/annurev-neuro-120722-100503
135. Kim CK, Miri A, Leung LC, Berndt A, Mourrain P, Tank DW, Burdine RD. 2014. Prolonged, brain-wide expression of nuclear-localized GCaMP3 for functional circuit mapping. Front Neural Circuits 8. doi:10.3389/fncir.2014.00138
136. Kleiner M, Brainard DH, Pelli DG. 2007. What's new in Psychtoolbox-3?Perception 36 ECVP Abstract Supplement. Presented at the Perception 36 ECVP.
137. Klioutchnikov A, Wallace DJ, Sawinski J, Voit K-M, Groemping Y, Kerr JND. 2023. A three-photon head-mounted microscope for imaging all layers of visual cortex in freely moving mice. Nat Methods 20:610–616. doi:10.1038/s41592-022-01688-9
138. Kondo S, Yoshida T, Ohki K. 2016. Mixed functional microarchitectures for orientation selectivity in the mouse primary visual cortex. Nat Commun 7:13210. doi:10.1038/ncomms13210
139. Kuffler SW. 1953. Discharge patterns and functional organization of mammalian retina. J Neurophysiol 16:37–68. doi:10.1152/jn.1953.16.1.37
140. La Chioma A, Bonhoeffer T, Hübener M. 2020. Disparity Sensitivity and Binocular Integration in Mouse Visual Cortex Areas. J Neurosci 40:8883–8899. doi:10.1523/JNEUROSCI.1060-20.2020
141. La Chioma A, Bonhoeffer T, Hübener M. 2019. Area-Specific Mapping of Binocular Disparity across Mouse Visual Cortex. Curr Biol 29:2954-2960.e5. doi:10.1016/j.cub.2019.07.037
142. Larsch J, Baier H. 2018. Biological Motion as an Innate Perceptual Mechanism Driving Social Affiliation. Curr Biol 28:3523-3532.e4. doi:10.1016/j.cub.2018.09.014
143. Lauer J, Zhou M, Ye S, Menegas W, Schneider S, Nath T, Rahman MM, Di Santo V, Soberanes D, Feng G, Murthy VN, Lauder G, Dulac C, Mathis MW, Mathis A. 2022. Multi-animal pose estimation, identification and tracking with DeepLabCut. Nat Methods 19:496–504. doi:10.1038/s41592-022-01443-0
144. Lee AM, Hoy JL, Bonci A, Wilbrecht L, Stryker MP, Niell CM. 2014. Identification of a Brainstem Circuit Regulating Visual Cortical State in Parallel with Locomotion. Neuron 83:455–466. doi:10.1016/j.neuron.2014.06.031
145. Lehnert J, Cha K, Halperin J, Yang K, Zheng DF, Khadra A, Cook EP, Krishnaswamy A. 2023. Visual attention to features and space in mice using reverse correlation. Curr Biol 33:3690-3701.e4. doi:10.1016/j.cub.2023.07.060
146. Lien AD, Scanziani M. 2018. Cortical direction selectivity emerges at convergence of thalamic synapses. Nature 558:80–86. doi:10.1038/s41586-018-0148-5
147. Lin MZ, Schnitzer MJ. 2016. Genetically encoded indicators of neuronal activity. Nat Neurosci 19:1142–1153. doi:10.1038/nn.4359
148. Liu C-H, Coleman JE, Davoudi H, Zhang K, Hussain Shuler MG. 2015. Selective Activation of a Putative Reinforcement Signal Conditions Cued Interval Timing in Primary Visual Cortex. Curr Biol 25:1551–1561. doi:10.1016/j.cub.2015.04.028
149. Liu RC, Tzonev S, Rebrik S, Miller KD. 2001. Variability and Information in a Neural Code of the Cat Lateral Geniculate Nucleus. J Neurophysiol 86:2789–2806. doi:10.1152/jn.2001.86.6.2789

150. Loomis JM, Blascovich JJ, Beall AC. 1999. Immersive virtual environment technology as a basic research tool in psychology. Behav Res Methods Instrum Comput 31:557–564. doi:10.3758/BF03200735
151. Lu J, Li C, Singh-Alvarado J, Zhou ZC, Fröhlich F, Mooney R, Wang F. 2018. MIN1PIPE: A Miniscope 1-Photon-Based Calcium Imaging Signal Extraction Pipeline. Cell Rep 23:3673–3684. doi:10.1016/j.celrep.2018.05.062
152. Mangini NJ, Pearlman AL. 1980. Laminar distribution of receptive field properties in the primary visual cortex of the mouse. J Comp Neurol 193:203–222. doi:10.1002/cne.901930114
153. Marshel JH, Kaye AP, Nauhaus I, Callaway EM. 2012. Anterior-Posterior Direction Opponency in the Superficial Mouse Lateral Geniculate Nucleus. Neuron 76:713–720. doi:10.1016/j.neuron.2012.09.021
154. Martinez-Conde S, Macknik SL, Hubel DH. 2000. Microsaccadic eye movements and firing of single cells in the striate cortex of macaque monkeys. Nat Neurosci 3:251–258. doi:10.1038/72961
155. Masland RH. 2012. The Neuronal Organization of the Retina. Neuron 76:266–280. doi:10.1016/j.neuron.2012.10.002
156. Mathis A, Biasi T, Schneider S, Yuksekgonul M, Rogers B, Bethge M, Mathis MW. 2021. Pretraining boosts out-of-domain robustness for pose estimation2021 IEEE Winter Conference on Applications of Computer Vision (WACV). Presented at the 2021 IEEE Winter Conference on Applications of Computer Vision (WACV). Waikoloa, HI, USA: IEEE. pp. 1858–1867. doi:10.1109/WACV48630.2021.00190
157. Mathis A, Mamidanna P, Cury KM, Abe T, Murthy VN, Mathis MW, Bethge M. 2018. DeepLabCut: markerless pose estimation of user-defined body parts with deep learning. Nat Neurosci 21:1281–1289. doi:10.1038/s41593-018-0209-y
158. McAdams CJ, Maunsell JHR. 1999. Effects of Attention on Orientation-Tuning Functions of Single Neurons in Macaque Cortical Area V4. J Neurosci 19:431–441. doi:10.1523/JNEUROSCI.19-01-00431.1999
159. McGinley MJ, David SV, McCormick DA. 2015. Cortical Membrane Potential Signature of Optimal States for Sensory Signal Detection. Neuron 87:179–192. doi:10.1016/j.neuron.2015.05.038
160. McInnes L, Healy J, Melville J. 2020. UMAP: Uniform Manifold Approximation and Projection for Dimension Reduction. doi:10.48550/arXiv.1802.03426
161. Meijer GT, Montijn JS, Pennartz CMA, Lansink CS. 2017. Audiovisual Modulation in Mouse Primary Visual Cortex Depends on Cross-Modal Stimulus Configuration and Congruency. J Neurosci 37:8783–8796. doi:10.1523/JNEUROSCI.0468-17.2017
162. Métin C, Godement P, Imbert M. 1988. The primary visual cortex in the mouse: Receptive field properties and functional organization. Exp Brain Res 69. doi:10.1007/BF00247312
163. Meyer AF, O'Keefe J, Poort J. 2020. Two Distinct Types of Eye-Head Coupling in Freely Moving Mice. Curr Biol 30:2116-2130.e6. doi:10.1016/j.cub.2020.04.042
164. Meyer AF, Poort J, O'Keefe J, Sahani M, Linden JF. 2018. A Head-Mounted Camera System Integrates Detailed Behavioral Monitoring with Multichannel Electrophysiology in Freely Moving Mice. Neuron 100:46-60.e7. doi:10.1016/j.neuron.2018.09.020
165. Michaiel AM, Abe ET, Niell CM. 2020. Dynamics of gaze control during prey capture in freely moving mice. eLife 9:e57458. doi:10.7554/eLife.57458
166. Miller CT, Gire D, Hoke K, Huk AC, Kelley D, Leopold DA, Smear MC, Theunissen F, Yartsev M, Niell CM. 2022. Natural behavior is the language of the brain. Curr Biol 32:R482–R493. doi:10.1016/j.cub.2022.03.031
167. Miller CT, Hale ME, Okano H, Okabe S, Mitra P. 2019. Comparative Principles for Next-Generation Neuroscience. Front Behav Neurosci 13:12. doi:10.3389/fnbeh.2019.00012
168. Miller KD. 2016. Canonical computations of cerebral cortex. Curr Opin Neurobiol, Neurobiology of cognitive behavior 37:75–84. doi:10.1016/j.conb.2016.01.008
169. Mimica B, Tombaz T, Battistin C, Fuglstad JG, Dunn BA, Whitlock JR. 2023. Behavioral decomposition reveals rich encoding structure employed across neocortex in rats. Nat Commun 14:3947. doi:10.1038/s41467-023-39520-3
170. Minderer M, Harvey CD, Donato F, Moser EI. 2016. Virtual reality explored. Nature 533:324–325. doi:10.1038/nature17899
171. Miura SK, Scanziani M. 2022. Distinguishing externally from saccade-induced motion in visual cortex. Nature 610:135–142. doi:10.1038/s41586-022-05196-w
172. Morimoto MM, Uchishiba E, Saleem AB. 2021. Organization of feedback projections to mouse primary visual cortex. iScience 24. doi:10.1016/j.isci.2021.102450

173. Morin LP, Studholme KM. 2014. Retinofugal projections in the mouse. J Comp Neurol 522:3733–3753. doi:10.1002/cne.23635
174. Movshon JA, Thompson ID, Tolhurst DJ. 1978. Spatial summation in the receptive fields of simple cells in the cat's striate cortex. J Physiol 283:53–77. doi:10.1113/jphysiol.1978.sp012488
175. Musall S, Kaufman MT, Juavinett AL, Gluf S, Churchland AK. 2019. Single-trial neural dynamics are dominated by richly varied movements. Nat Neurosci 22:1677–1686. doi:10.1038/s41593-019-0502-4
176. Muzzu T, Saleem AB. 2021. Feature selectivity can explain mismatch signals in mouse visual cortex. Cell Rep 37. doi:10.1016/j.celrep.2021.109772
177. Myers-Joseph D, Wilmes KA, Fernandez-Otero M, Clopath C, Khan AG. 2024. Disinhibition by VIP interneurons is orthogonal to cross-modal attentional modulation in primary visual cortex. Neuron 112:628-645.e7. doi:10.1016/j.neuron.2023.11.006
178. Nakai J, Ohkura M, Imoto K. 2001. A high signal-to-noise Ca2+ probe composed of a single green fluorescent protein. Nat Biotechnol 19:137–141. doi:10.1038/84397
179. Nath T, Mathis A, Chen AC, Patel A, Bethge M, Mathis MW. 2019. Using DeepLabCut for 3D markerless pose estimation across species and behaviors. Nat Protoc 14:2152–2176. doi:10.1038/s41596-019-0176-0
180. Nevian T, Helmchen F. 2007. Calcium indicator loading of neurons using single-cell electroporation. Pflüg Arch - Eur J Physiol 454:675–688. doi:10.1007/s00424-007-0234-2
181. Niell CM, Scanziani M. 2021. How Cortical Circuits Implement Cortical Computations: Mouse Visual Cortex as a Model. Annu Rev Neurosci 44:517–546. doi:10.1146/annurev-neuro-102320-085825
182. Niell CM, Stryker MP. 2010. Modulation of Visual Responses by Behavioral State in Mouse Visual Cortex. Neuron 65:472–479. doi:10.1016/j.neuron.2010.01.033
183. Niell CM, Stryker MP. 2008. Highly Selective Receptive Fields in Mouse Visual Cortex. J Neurosci 28:7520–7536. doi:10.1523/JNEUROSCI.0623-08.2008
184. Nienborg H, Hasenstaub A, Nauhaus I, Taniguchi H, Huang ZJ, Callaway EM. 2013. Contrast Dependence and Differential Contributions from Somatostatin- and Parvalbumin-Expressing Neurons to Spatial Integration in Mouse V1. J Neurosci 33:11145–11154. doi:10.1523/JNEUROSCI.5320-12.2013
185. Nowogrodzki J. 2019. How to support open-source software and stay sane. Nature 571:133–134. doi:10.1038/d41586-019-02046-0
186. Nvidia Corporation. 1999. Perfect Reflections and Specular Lighting Effects With Cube Environment Mapping. Nvidia Corporation.
187. Oh SW, Harris JA, Ng L, Winslow B, Cain N, Mihalas S, Wang Q, Lau C, Kuan L, Henry AM, Mortrud MT, Ouellette B, Nguyen TN, Sorensen SA, Slaughterbeck CR, Wakeman W, Li Y, Feng D, Ho A, Nicholas E, Hirokawa KE, Bohn P, Joines KM, Peng H, Hawrylycz MJ, Phillips JW, Hohmann JG, Wohnoutka P, Gerfen CR, Koch C, Bernard A, Dang C, Jones AR, Zeng H. 2014. A mesoscale connectome of the mouse brain. Nature 508:207–214. doi:10.1038/nature13186
188. O'Herron P, Levy M, Woodward JJ, Kara P. 2020. An Unexpected Dependence of Cortical Depth in Shaping Neural Responsiveness and Selectivity in Mouse Visual Cortex. eNeuro 7. doi:10.1523/ENEURO.0497-19.2020
189. Ohki K, Chung S, Ch'ng YH, Kara P, Reid RC. 2005. Functional imaging with cellular resolution reveals precise micro-architecture in visual cortex. Nature 433:597–603. doi:10.1038/nature03274
190. Olsen SR, Bortone DS, Adesnik H, Scanziani M. 2012. Gain control by layer six in cortical circuits of vision. Nature 483:47–52. doi:10.1038/nature10835
191. Orlowska-Feuer P, Ebrahimi AS, Zippo AG, Petersen RS, Lucas RJ, Storchi R. 2022. Look-up and look-down neurons in the mouse visual thalamus during freely moving exploration. Curr Biol 32:3987-3999.e4. doi:10.1016/j.cub.2022.07.049
192. Paredes RM, Etzler JC, Watts LT, Zheng W, Lechleiter JD. 2008. Chemical calcium indicators. Methods, Optical Methods in Calcium Signaling 46:143–151. doi:10.1016/j.ymeth.2008.09.025
193. Park S-G, Jeong Y-C, Kim D-G, Lee M-H, Shin A, Park G, Ryoo J, Hong J, Bae S, Kim C-H, Lee P-S, Kim D. 2018. Medial preoptic circuit induces hunting-like actions to target objects and prey. Nat Neurosci 21:364–372. doi:10.1038/s41593-018-0072-x

194. Parker PRL, Abe ET, Beatie NT, Leonard ES, Martins DM, Sharp SL, Wyrick DG, Mazzucato L, Niell CM. 2022a. Distance estimation from monocular cues in an ethological visuomotor task. eLife 11:e74708. doi:10.7554/eLife.74708
195. Parker PRL, Abe ETT, Leonard ESP, Martins DM, Niell CM. 2022b. Joint coding of visual input and eye/head position in V1 of freely moving mice. Neuron 110:3897-3906.e5. doi:10.1016/j.neuron.2022.08.029
196. Parker PRL, Martins DM, Leonard ESP, Casey NM, Sharp SL, Abe ETT, Smear MC, Yates JL, Mitchell JF, Niell CM. 2023. A dynamic sequence of visual processing initiated by gaze shifts. Nat Neurosci 26:2192–2202. doi:10.1038/s41593-023-01481-7
197. Pelli DG. 1997. The VideoToolbox software for visual psychophysics: transforming numbers into movies. Spat Vis 10:437–442. doi:10.1163/156856897X00366
198. Pereira TD, Shaevitz JW, Murthy M. 2020. Quantifying behavior to understand the brain. Nat Neurosci 23:1537–1549. doi:10.1038/s41593-020-00734-z
199. Petros TJ, Rebsam A, Mason CA. 2008. Retinal Axon Growth at the Optic Chiasm: To Cross or Not to Cross. Annu Rev Neurosci 31:295–315. doi:10.1146/annurev.neuro.31.060407.125609
200. Pinke D, Issa JB, Dara GA, Dobos G, Dombeck DA. 2023. Full field-of-view virtual reality goggles for mice. Neuron 111:3941-3952.e6. doi:10.1016/j.neuron.2023.11.019
201. Piscopo DM, El-Danaf RN, Huberman AD, Niell CM. 2013. Diverse Visual Features Encoded in Mouse Lateral Geniculate Nucleus. J Neurosci 33:4642–4656. doi:10.1523/JNEUROSCI.5187-12.2013
202. Pnevmatikakis EA, Soudry D, Gao Y, Machado TA, Merel J, Pfau D, Reardon T, Mu Y, Lacefield C, Yang W, Ahrens M, Bruno R, Jessell TM, Peterka DS, Yuste R, Paninski L. 2016. Simultaneous Denoising, Deconvolution, and Demixing of Calcium Imaging Data. Neuron 89:285–299. doi:10.1016/j.neuron.2015.11.037
203. Priebe NJ, McGee AW. 2014. Mouse vision as a gateway for understanding how experience shapes neural circuits. Front Neural Circuits 8. doi:10.3389/fncir.2014.00123
204. Purves D, Augustine GJ, Fitzpatrick D, Katz LC, LaMantia A-S, McNamara JO, Williams SM. 2001. Types of Eye Movements and Their FunctionsNeuroscience. 2nd Edition. Sinauer Associates.
205. Rancz EA, Franks KM, Schwarz MK, Pichler B, Schaefer AT, Margrie TW. 2011. Transfection via whole-cell recording in vivo: bridging single-cell physiology, genetics and connectomics. Nat Neurosci 14:527–532. doi:10.1038/nn.2765
206. Rancz EA, Moya J, Drawitsch F, Brichta AM, Canals S, Margrie TW. 2015. Widespread Vestibular Activation of the Rodent Cortex. J Neurosci 35:5926–5934. doi:10.1523/JNEUROSCI.1869-14.2015
207. Reid RC, Soodak RE, Shapley RM. 1991. Directional selectivity and spatiotemporal structure of receptive fields of simple cells in cat striate cortex. J Neurophysiol 66:505–529. doi:10.1152/jn.1991.66.2.505
208. Reimer J, Froudarakis E, Cadwell CR, Yatsenko D, Denfield GH, Tolias AS. 2014. Pupil Fluctuations Track Fast Switching of Cortical States during Quiet Wakefulness. Neuron 84:355–362. doi:10.1016/j.neuron.2014.09.033
209. Reinagel P, Reid RC. 2000. Temporal Coding of Visual Information in the Thalamus. J Neurosci 20:5392–5400. doi:10.1523/JNEUROSCI.20-14-05392.2000
210. Rich PD, Thiberge SY, Scott BB, Guo C, Tervo DG, Brody CD, Karpova AY, Daw ND, Tank DW. 2023. Magnetic voluntary head-fixation in transgenic rats enables lifetime imaging of hippocampal neurons. bioRxiv. doi:10.1101/2023.08.17.553594
211. Ringach DL, Mineault PJ, Tring E, Olivas ND, Garcia-Junco-Clemente P, Trachtenberg JT. 2016. Spatial clustering of tuning in mouse primary visual cortex. Nat Commun 7:12270. doi:10.1038/ncomms12270
212. Rose T, Jaepel J, Hübener M, Bonhoeffer T. 2016. Cell-specific restoration of stimulus preference after monocular deprivation in the visual cortex. Science 352:1319–1322. doi:10.1126/science.aad3358
213. Ruiz-Mejias M, Ciria-Suarez L, Mattia M, Sanchez-Vives MV. 2011. Slow and fast rhythms generated in the cerebral cortex of the anesthetized mouse. J Neurophysiol 106:2910–2921. doi:10.1152/jn.00440.2011
214. Russell LE, Dalgleish HWP, Nutbrown R, Gauld OM, Herrmann D, Fişek M, Packer AM, Häusser M. 2022. All-optical interrogation of neural circuits in behaving mice. Nat Protoc 17:1579–1620. doi:10.1038/s41596-022-00691-w

215. Saleem AB. 2020. Two stream hypothesis of visual processing for navigation in mouse. Curr Opin Neurobiol, Systems Neuroscience 64:70–78. doi:10.1016/j.conb.2020.03.009
216. Saleem AB, Ayaz A, Jeffery KJ, Harris KD, Carandini M. 2013. Integration of visual motion and locomotion in mouse visual cortex. Nat Neurosci 16:1864–1869. doi:10.1038/nn.3567
217. Saleem AB, Diamanti EM, Fournier J, Harris KD, Carandini M. 2018. Coherent encoding of subjective spatial position in visual cortex and hippocampus. Nature 562:124–127. doi:10.1038/s41586-018-0516-1
218. Salkoff DB, Zagha E, McCarthy E, McCormick DA. 2020. Movement and Performance Explain Widespread Cortical Activity in a Visual Detection Task. Cereb Cortex 30:421–437. doi:10.1093/cercor/bhz206
219. Samonds JM, Choi V, Priebe NJ. 2019. Mice Discriminate Stereoscopic Surfaces Without Fixating in Depth. J Neurosci 39:8024–8037. doi:10.1523/JNEUROSCI.0895-19.2019
220. Sanes JR, Masland RH. 2015. The Types of Retinal Ganglion Cells: Current Status and Implications for Neuronal Classification. Annu Rev Neurosci 38:221–246. doi:10.1146/annurev-neuro-071714-034120
221. Sattler NJ, Wehr M. 2021. A Head-Mounted Multi-Camera System for Electrophysiology and Behavior in Freely-Moving Mice. Front Neurosci 14. doi:10.3389/fnins.2020.592417
222. Scholl B, Burge J, Priebe NJ. 2013. Binocular integration and disparity selectivity in mouse primary visual cortex. J Neurophysiol 109:3013–3024. doi:10.1152/jn.01021.2012
223. Schumacher JW, McCann MK, Maximov KJ, Fitzpatrick D. 2022. Selective enhancement of neural coding in V1 underlies fine-discrimination learning in tree shrew. Curr Biol 32:3245-3260.e5. doi:10.1016/j.cub.2022.06.009
224. Seabrook TA, Burbridge TJ, Crair MC, Huberman AD. 2017a. Architecture, Function, and Assembly of the Mouse Visual System. Annu Rev Neurosci 40:499–538. doi:10.1146/annurev-neuro-071714-033842
225. Seabrook TA, Dhande OS, Ishiko N, Wooley VP, Nguyen PL, Huberman AD. 2017b. Strict Independence of Parallel and Poly-synaptic Axon-Target Matching during Visual Reflex Circuit Assembly. Cell Rep 21:3049–3064. doi:10.1016/j.celrep.2017.11.044
226. Shadlen MN, Newsome WT. 1998. The Variable Discharge of Cortical Neurons: Implications for Connectivity, Computation, and Information Coding. J Neurosci 18:3870–3896. doi:10.1523/JNEUROSCI.18-10-03870.1998
227. Shamash P, Olesen SF, Iordanidou P, Campagner D, Banerjee N, Branco T. 2021. Mice learn multi-step routes by memorizing subgoal locations. Nat Neurosci 24:1270–1279. doi:10.1038/s41593-021-00884-8
228. Shemesh OA, Linghu C, Piatkevich KD, Goodwin D, Celiker OT, Gritton HJ, Romano MF, Gao R, Yu C-C (Jay), Tseng H-A, Bensussen S, Narayan S, Yang C-T, Freifeld L, Siciliano CA, Gupta I, Wang J, Pak N, Yoon Y-G, Ullmann JFP, Guner-Ataman B, Noamany H, Sheinkopf ZR, Park WM, Asano S, Keating AE, Trimmer JS, Reimer J, Tolias AS, Bear MF, Tye KM, Han X, Ahrens MB, Boyden ES. 2020. Precision Calcium Imaging of Dense Neural Populations via a Cell-Body-Targeted Calcium Indicator. Neuron 107:470-486.e11. doi:10.1016/j.neuron.2020.05.029
229. Shi X, Barchini J, Ledesma HA, Koren D, Jin Y, Liu X, Wei W, Cang J. 2017. Retinal origin of direction selectivity in the superior colliculus. Nat Neurosci 20:550–558. doi:10.1038/nn.4498
230. Shuler MG, Bear MF. 2006. Reward timing in the primary visual cortex. Science 311:1606–1609. doi:10.1126/science.1123513
231. Sieben K, Röder B, Hanganu-Opatz IL. 2013. Oscillatory Entrainment of Primary Somatosensory Cortex Encodes Visual Control of Tactile Processing. J Neurosci 33:5736–5749. doi:10.1523/JNEUROSCI.4432-12.2013
232. Sinex DG, Burdette LJ, Pearlman AL. 1979. A psychophysical investigation of spatial vision in the normal and reeler mutant mouse. Vision Res 19:853–857. doi:10.1016/0042-6989(79)90018-X
233. Slezak M, Kandler S, Van Veldhoven PP, Van den Haute C, Bonin V, Holt MG. 2019. Distinct Mechanisms for Visual and Motor-Related Astrocyte Responses in Mouse Visual Cortex. Curr Biol 29:3120-3127.e5. doi:10.1016/j.cub.2019.07.078
234. Socha KZ, Couto J, Whiteway MR, Hosseinjany S, Butts DA, Bonin V. 2024. Behavioral modulations can alter the visual tuning of neurons in the mouse thalamocortical pathway. Cell Rep 43. doi:10.1016/j.celrep.2024.114947
235. Spacek MA, Crombie D, Bauer Y, Born G, Liu X, Katzner S, Busse L. 2022. Robust effects of corticothalamic feedback and behavioral state on movie responses in mouse dLGN. eLife 11:e70469. doi:10.7554/eLife.70469

236. Stefanini F, Kushnir L, Jimenez JC, Jennings JH, Woods NI, Stuber GD, Kheirbek MA, Hen R, Fusi S. 2020. A Distributed Neural Code in the Dentate Gyrus and in CA1. Neuron 107:703-716.e4. doi:10.1016/j.neuron.2020.05.022
237. Steinmetz NA, Aydin C, Lebedeva A, Okun M, Pachitariu M, Bauza M, Beau M, Bhagat J, Böhm C, Broux M, Chen S, Colonell J, Gardner RJ, Karsh B, Kloosterman F, Kostadinov D, Mora-Lopez C, O'Callaghan J, Park J, Putzeys J, Sauerbrei B, van Daal RJJ, Vollan AZ, Wang S, Welkenhuysen M, Ye Z, Dudman JT, Dutta B, Hantman AW, Harris KD, Lee AK, Moser EI, O'Keefe J, Renart A, Svoboda K, Häusser M, Haesler S, Carandini M, Harris TD. 2021. Neuropixels 2.0: A miniaturized high-density probe for stable, long-term brain recordings. Science 372:eabf4588. doi:10.1126/science.abf4588
238. Štih V, Petrucco L, Kist AM, Portugues R. 2019. Stytra: An open-source, integrated system for stimulation, tracking and closed-loop behavioral experiments. PLOS Comput Biol 15:e1006699. doi:10.1371/journal.pcbi.1006699
239. Stowers JR, Hofbauer M, Bastien R, Griessner J, Higgins P, Farooqui S, Fischer RM, Nowikovsky K, Haubensak W, Couzin ID, Tessmar-Raible K, Straw AD. 2017. Virtual reality for freely moving animals. Nat Methods 14:995–1002. doi:10.1038/nmeth.4399
240. St-Pierre F, Marshall JD, Yang Y, Gong Y, Schnitzer MJ, Lin MZ. 2014. High-fidelity optical reporting of neuronal electrical activity with an ultrafast fluorescent voltage sensor. Nat Neurosci 17:884–889. doi:10.1038/nn.3709
241. Stringer C, Pachitariu M, Steinmetz N, Reddy CB, Carandini M, Harris KD. 2019. Spontaneous Behaviors Drive Multidimensional, Brain-wide Activity. Science 364:255. doi:10.1126/science.aav7893
242. Sun Y, Paşca SP, Portmann T, Goold C, Worringer KA, Guan W, Chan KC, Gai H, Vogt D, Chen Y-JJ. 2016. A deleterious Nav1. 1 mutation selectively impairs telencephalic inhibitory neurons derived from Dravet syndrome patients. Elife 5:e13073.
243. Swadlow HA. 1983. Efferent systems of primary visual cortex: A review of structure and function. Brain Res Rev 6:1–24. doi:10.1016/0165-0173(83)90002-4
244. Thurley K. 2022. Naturalistic neuroscience and virtual reality. Front Syst Neurosci 16. doi:10.3389/fnsys.2022.896251
245. Tian L, Hires SA, Looger LL. 2012. Imaging Neuronal Activity with Genetically Encoded Calcium Indicators. Cold Spring Harb Protoc 2012:647–56. doi:10.1101/pdb.top069609
246. Tian L, Hires SA, Mao T, Huber D, Chiappe ME, Chalasani SH, Petreanu L, Akerboom J, McKinney SA, Schreiter ER, Bargmann CI, Jayaraman V, Svoboda K, Looger LL. 2009. Imaging neural activity in worms, flies and mice with improved GCaMP calcium indicators. Nat Methods 6:875–881. doi:10.1038/nmeth.1398
247. Tomko DL, Barbaro NM, Ali FN. 1981. Effect of body tilt on receptive field orientation of simple visual cortical neurons in unanesthetized cats. Exp Brain Res 43:309–314. doi:10.1007/BF00238372
248. Tremblay R, Lee S, Rudy B. 2016. GABAergic Interneurons in the Neocortex: From Cellular Properties to Circuits. Neuron 91:260–292. doi:10.1016/j.neuron.2016.06.033
249. Tye KM, Miller EK, Taschbach FH, Benna MK, Rigotti M, Fusi S. 2024. Mixed selectivity: Cellular computations for complexity. Neuron 112:2289–2303. doi:10.1016/j.neuron.2024.04.017
250. van Beest EH, Mukherjee S, Kirchberger L, Schnabel UH, van der Togt C, Teeuwen RRM, Barsegyan A, Meyer AF, Poort J, Roelfsema PR, Self MW. 2021. Mouse visual cortex contains a region of enhanced spatial resolution. Nat Commun 12:4029. doi:10.1038/s41467-021-24311-5
251. Van den Bergh G, Zhang B, Arckens L, Chino YM. 2010. Receptive-field properties of V1 and V2 neurons in mice and macaque monkeys. J Comp Neurol 518:2051–2070. doi:10.1002/cne.22321
252. Vasilevskaya A, Widmer FC, Keller GB, Jordan R. 2023. Locomotion-induced gain of visual responses cannot explain visuomotor mismatch responses in layer 2/3 of primary visual cortex. Cell Rep 42. doi:10.1016/j.celrep.2023.112096
253. Vélez-Fort M, Bracey EF, Keshavarzi S, Rousseau CV, Cossell L, Lenzi SC, Strom M, Margrie TW. 2018. A Circuit for Integration of Head- and Visual-Motion Signals in Layer 6 of Mouse Primary Visual Cortex. Neuron 98:179-191.e6. doi:10.1016/j.neuron.2018.02.023
254. Vélez-Fort M, Rousseau CV, Niedworok CJ, Wickersham IR, Rancz EA, Brown APY, Strom M, Margrie TW. 2014. The Stimulus Selectivity and Connectivity of Layer Six Principal Cells Reveals Cortical Microcircuits Underlying Visual Processing. Neuron 83:1431–1443. doi:10.1016/j.neuron.2014.08.001

255. Vinck M, Batista-Brito R, Knoblich U, Cardin JA. 2015. Arousal and Locomotion Make Distinct Contributions to Cortical Activity Patterns and Visual Encoding. Neuron 86:740–754. doi:10.1016/j.neuron.2015.03.028
256. Volland S, Esteve-Rudd J, Hoo J, Yee C, Williams DS. 2015. A Comparison of Some Organizational Characteristics of the Mouse Central Retina and the Human Macula. PLOS ONE 10:e0125631. doi:10.1371/journal.pone.0125631
257. Wallace DJ, Greenberg DS, Sawinski J, Rulla S, Notaro G, Kerr JND. 2013. Rats maintain an overhead binocular field at the expense of constant fusion. Nature 498:65–69. doi:10.1038/nature12153
258. Wang L, Krauzlis RJ. 2018. Visual Selective Attention in Mice. Curr Biol 28:676-685.e4. doi:10.1016/j.cub.2018.01.038
259. Wang Q, Burkhalter A. 2007. Area map of mouse visual cortex. J Comp Neurol 502:339–357. doi:10.1002/cne.21286
260. Wang ZA, Chen S, Liu Y, Liu D, Svoboda K, Li N, Druckmann S. 2023. Not everything, not everywhere, not all at once: a study of brain-wide encoding of movement. doi:10.1101/2023.06.08.544257
261. Weiler S, Guggiana Nilo D, Bonhoeffer T, Hübener M, Rose T, Scheuss V. 2023. Functional and structural features of L2/3 pyramidal cells continuously covary with pial depth in mouse visual cortex. Cereb Cortex 33:3715–3733. doi:10.1093/cercor/bhac303
262. Weiler S, Rahmati V, Isstas M, Wutke J, Stark AW, Franke C, Graf J, Geis C, Witte OW, Hübener M, Bolz J, Margrie TW, Holthoff K, Teichert M. 2024. A primary sensory cortical interareal feedforward inhibitory circuit for tacto-visual integration. Nat Commun 15:3081. doi:10.1038/s41467-024-47459-2
263. West SL, Aronson JD, Popa LS, Feller KD, Carter RE, Chiesl WM, Gerhart ML, Shekhar AC, Ghanbari L, Kodandaramaiah SB, Ebner TJ. 2022. Wide-Field Calcium Imaging of Dynamic Cortical Networks during Locomotion. Cereb Cortex 32:2668–2687. doi:10.1093/cercor/bhab373
264. Wheatcroft T, Saleem AB, Solomon SG. 2022. Functional Organisation of the Mouse Superior Colliculus. Front Neural Circuits 16. doi:10.3389/fncir.2022.792959
265. Williams B, Del Rosario J, Muzzu T, Peelman K, Coletta S, Bichler EK, Speed A, Meyer-Baese L, Saleem AB, Haider B. 2021. Spatial modulation of dark versus bright stimulus responses in the mouse visual system. Curr Biol 31:4172-4179.e6. doi:10.1016/j.cub.2021.06.094
266. Wörgötter F, Eysel UTh. 1987. Quantitative determination of orientational and directional components in the response of visual cortical cells to moving stimuli. Biol Cybern 57:349–355. doi:10.1007/BF00354980
267. Yilmaz M, Meister M. 2013. Rapid Innate Defensive Responses of Mice to Looming Visual Stimuli. Curr Biol 23:2011–2015. doi:10.1016/j.cub.2013.08.015
268. Zagha E, Erlich JC, Lee S, Lur G, O'Connor DH, Steinmetz NA, Stringer C, Yang H. 2022. The Importance of Accounting for Movement When Relating Neuronal Activity to Sensory and Cognitive Processes. J Neurosci 42:1375–1382. doi:10.1523/JNEUROSCI.1919-21.2021
269. Zeng H, Chen S, Fink GR, Weidner R. 2023. Information Exchange between Cortical Areas: The Visual System as a Model. The Neuroscientist 29:370–384. doi:10.1177/10738584211069061
270. Zeng H, Sanes JR. 2017. Neuronal cell-type classification: challenges, opportunities and the path forward. Nat Rev Neurosci 18:530–546. doi:10.1038/nrn.2017.85
271. Zhang J, Hughes RN, Kim N, Fallon IP, Bakhurin K, Kim J, Severino FPU, Yin HH. 2022. All-optical imaging and patterned stimulation with a one-photon endoscope. doi:10.1101/2021.12.19.473349
272. Zhang Yan, Rózsa M, Liang Y, Bushey D, Wei Z, Zheng J, Reep D, Broussard GJ, Tsang A, Tsegaye G, Narayan S, Obara CJ, Lim J-X, Patel R, Zhang R, Ahrens MB, Turner GC, Wang SS-H, Korff WL, Schreiter ER, Svoboda K, Hasseman JP, Kolb I, Looger LL. 2023. Fast and sensitive GCaMP calcium indicators for imaging neural populations. Nature 615:884–891. doi:10.1038/s41586-023-05828-9
273. Zhang Yuanlong, Zhang G, Han X, Wu J, Li Z, Li X, Xiao G, Xie H, Fang L, Dai Q. 2023. Rapid detection of neurons in widefield calcium imaging datasets after training with synthetic data. Nat Methods 20:747–754. doi:10.1038/s41592-023-01838-7
274. Zhang Z, Russell LE, Packer AM, Gauld OM, Häusser M. 2018. Closed-loop all-optical interrogation of neural circuits in vivo. Nat Methods 15:1037–1040. doi:10.1038/s41592-018-0183-z

275. Zhao C, Chen S, Zhang L, Zhang D, Wu R, Hu Y, Zeng F, Li Y, Wu D, Yu F, Zhang Y, Zhang J, Chen L, Wang A, Cheng H. 2023. Miniature three-photon microscopy maximized for scattered fluorescence collection. Nat Methods 20:617–622. doi:10.1038/s41592-023-01777-3
276. Zhao X, Chen H, Liu X, Cang J. 2013. Orientation-selective Responses in the Mouse Lateral Geniculate Nucleus. J Neurosci 33:12751–12763. doi:10.1523/JNEUROSCI.0095-13.2013
277. Zhao X, Liu M, Cang J. 2014. Visual Cortex Modulates the Magnitude but Not the Selectivity of Looming-Evoked Responses in the Superior Colliculus of Awake Mice. Neuron 84:202–213. doi:10.1016/j.neuron.2014.08.037
278. Zhen D. 2017. Identifying the neural mechanisms of approach behavior: studying the role of superior colliculus during prey-capture behavior in the mouse. University of Oregon.
279. Zong W, Obenhaus HA, Skytøen ER, Eneqvist H, de Jong NL, Vale R, Jorge MR, Moser M-B, Moser EI. 2022. Large-scale two-photon calcium imaging in freely moving mice. Cell 185:1240-1256.e30. doi:10.1016/j.cell.2022.02.017

Appendix A: Supplementary Figures

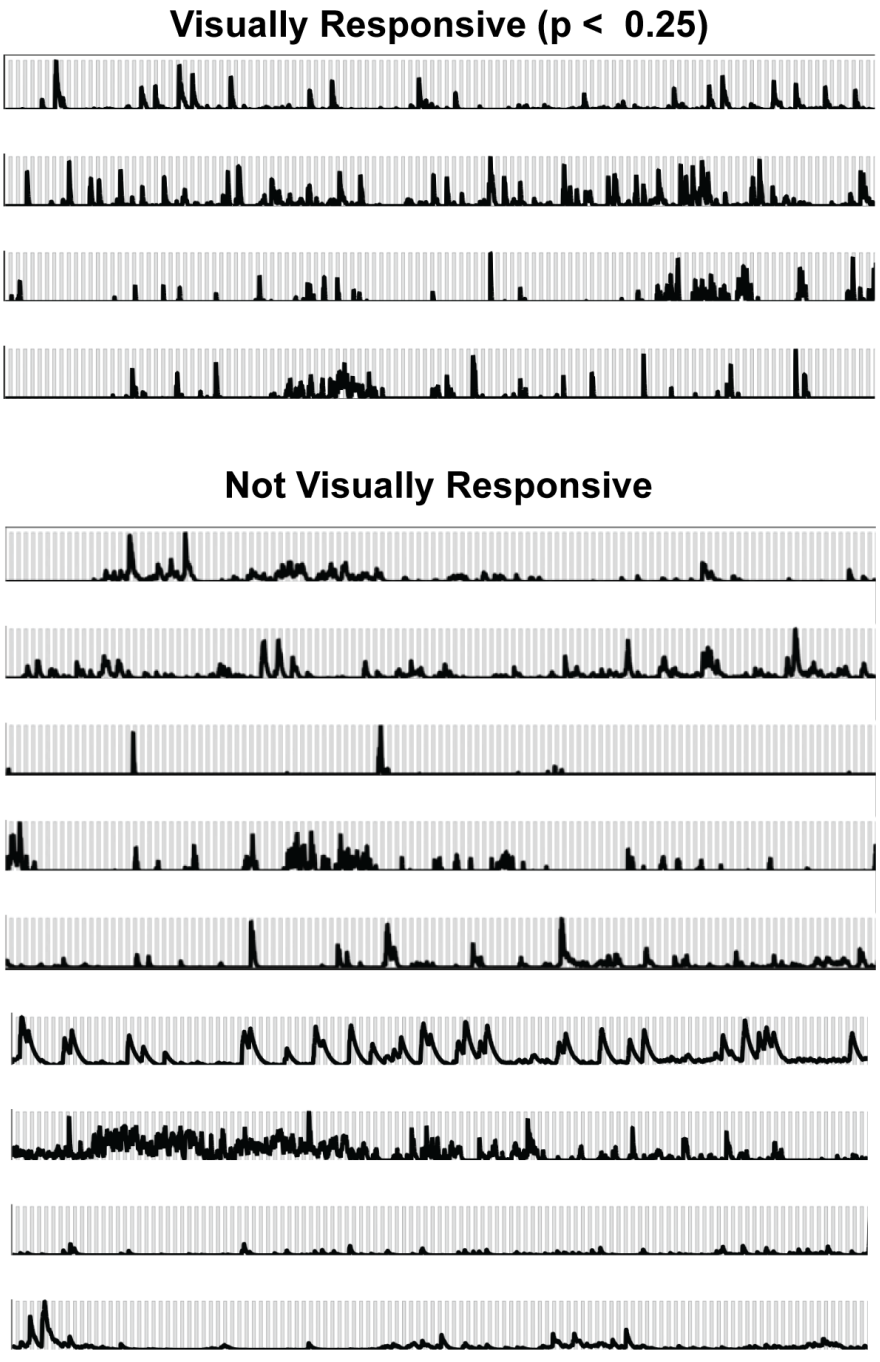

Supp. Figure 1 Examples of cells filtered by distribution-based visual responsivity metric | Deconvolved fluorescence traces for cells considered visually responsive during a head fixed experiment. Gray boxes – visual stimulus trials. Cells were considered visually responsive if the AUC of the deconvolved fluorescence trace during visual trials was greater than the preceding 5 seconds of inter-trial interval (Mann-Whitney U test, $p < 0.25$). The threshold of 0.25 was determined by visual inspection of the deconvolved fluorescence traces.

Appendix A: Supplementary Figures

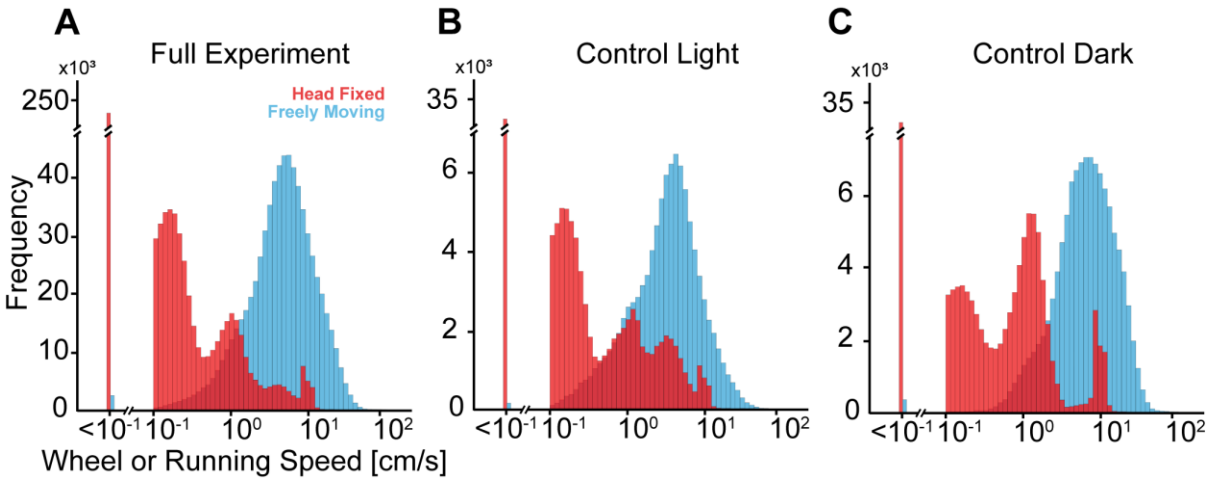

Supp. Figure 2 Distributions of running wheel and locomotion speeds | A. Distributions of running wheel or locomotion speeds during head fixed or freely moving experiments. Speed traces were averaged in 200 ms bins. Histograms use 50 evenly logarithmically spaced bins. **B and C.** Same as A, but for control experiments without visual stimuli conducted in the light or dark, respectively.

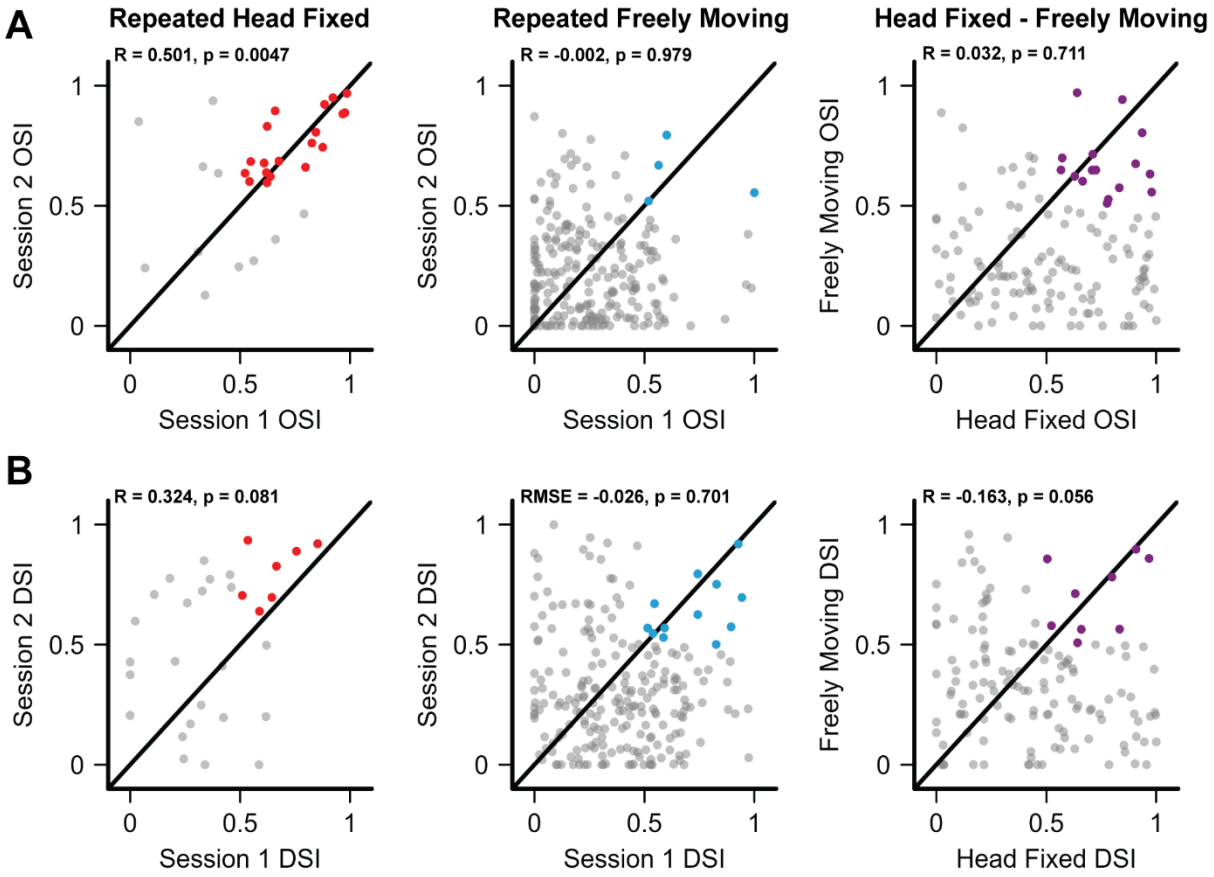

Supp. Figure 3 Orientation and direction selectivity indices for visually responsive, automatically re-identified cells | Same as **Figure 3.12**, but for automatically re-identified cells that were classified as visually responsive during both sessions. Repeated head fixed sessions: n = 30 cells from 3 mice. Repeated freely moving sessions: n = 224 cells from 5 mice. Consecutive head fixed – freely moving sessions: n = 136 cells from 6 mice.

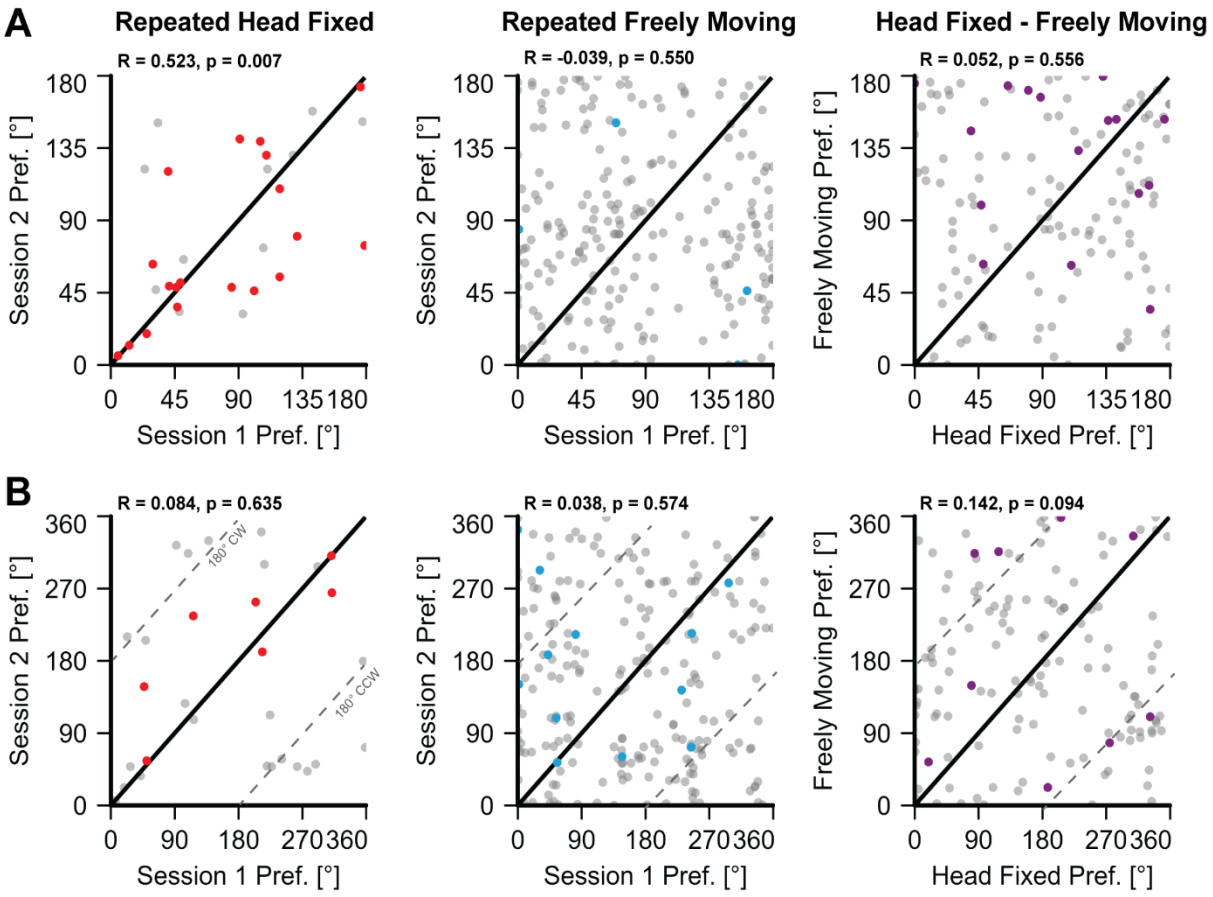

Supp. Figure 4 Preferred orientation and direction for visually responsive, automatically re-identified cells | Same as **Figure 3.13**, but for automatically re-identified cells that were classified as visually responsive during both sessions. Repeated head fixed sessions: n = 30 cells from 3 mice. Repeated freely moving sessions: n = 224 cells from 5 mice. Consecutive head fixed – freely moving sessions: n = 136 cells from 6 mice.

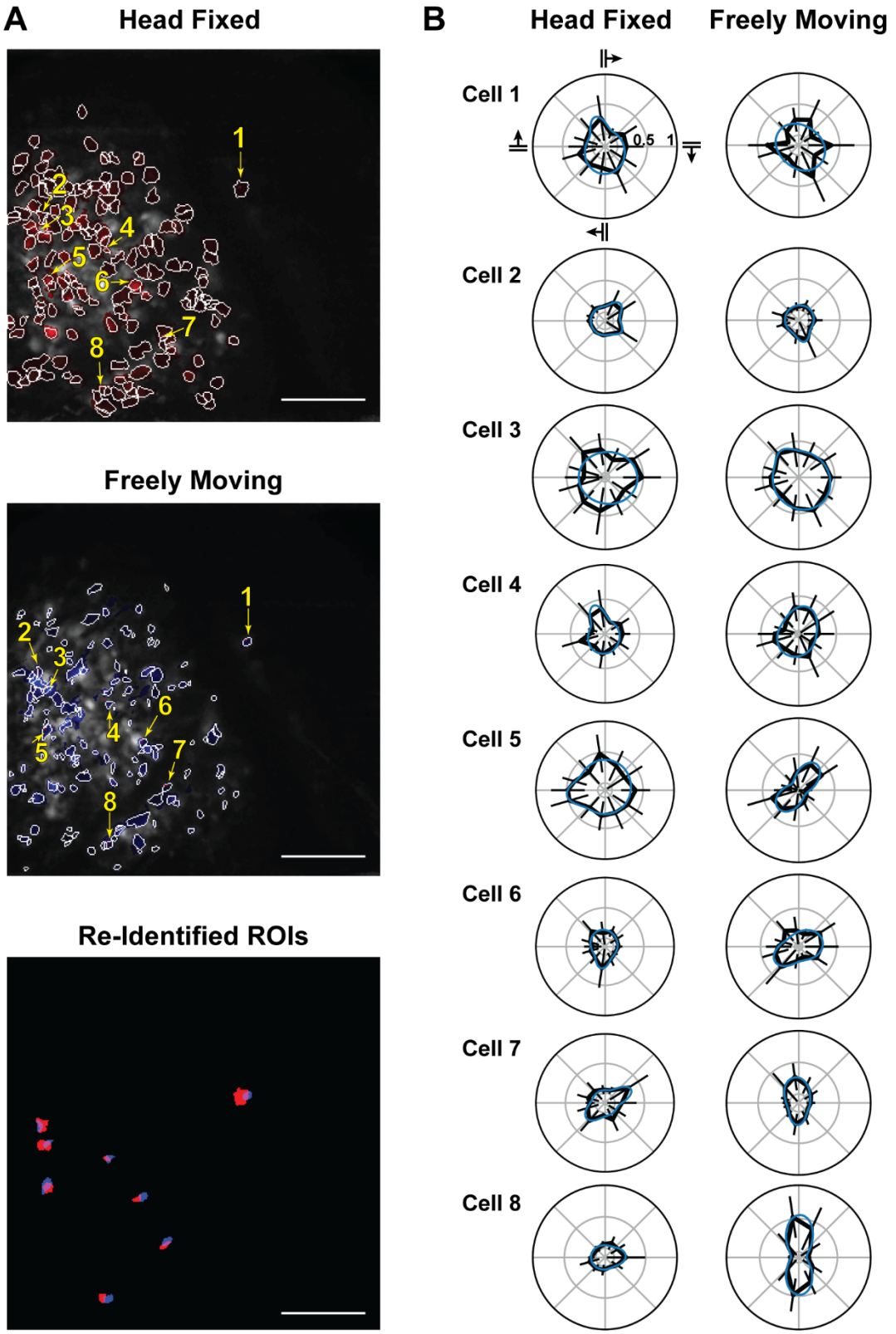

Supp. Figure 5 Tuning curves of example, hand-picked re-identified neurons change between head fixation and free behavior | A. Fields of view from example head fixed and freely moving experiments. Scale bars = 100 μm. **B.** Polar direction tuning curves for the cells re-identified in **A**. Black line – mean trial AUC ± std, blue line – double Von Mises function fit to the mean.

Appendix B: Statistics

Fraction Visually Responsive

	Head Fixed	Head Fixed Ctrl. Light	Freely Moving	Freely Moving Ctrl. Light	Freely Moving Ctrl. Dark
Head Fixed					
Head Fixed Ctrl. Light	**3.23 e -7**				
Head Fixed Ctrl. Dark	**1.03 e -9**	0.421			
Freely Moving	0.449				
Freely Moving Ctrl. Light			**1.24 e -6**		
Freely Moving Ctrl. Dark			**1.32 e -7**	0.535	

Fraction Orientation Tuned

	Head Fixed	Head Fixed Ctrl. Light	Freely Moving	Freely Moving Ctrl. Light	Freely Moving Ctrl. Dark
Head Fixed					
Head Fixed Ctrl. Light	**2.64 e -19**				
Head Fixed Ctrl. Dark	**3.91 e -16**	0.553			
Freely Moving	**6.88 e -7**				
Freely Moving Ctrl. Light			**3.20 e -3**		
Freely Moving Ctrl. Dark			**5.61 e -7**	**0.005**	

Fraction Direction Tuned

	Head Fixed	Head Fixed Ctrl. Light	Freely Moving	Freely Moving Ctrl. Light	Freely Moving Ctrl. Dark
Head Fixed					
Head Fixed Ctrl. Light	**1.38 e -10**				
Head Fixed Ctrl. Dark	**1.45 e -6**	0.213			
Freely Moving	0.104				
Freely Moving Ctrl. Light			**1.48 e -3**		
Freely Moving Ctrl. Dark			**8.28 e -9**	**0.03**	

Table 1: P-values corresponding to Figure 3.8. Values are the result of a Kruskal-Wallis test followed by a Dunn post-hoc test with Bonferroni correction for multiple comparisons. For comparisons between distributions with different sample sizes (i.e. between the main experiment and controls), distributions were bootstrapped with 1000 repetitions, and the reported p-value is the upper bound of the 95% confidence interval of the distribution of post-hoc corrected, bootstrapped p-values.

Appendix B: Statistics

Running Wheel Speed

	Head Fixed	Head Fixed Ctrl. Light	Head Fixed Ctrl. Dark
Head Fixed			
Head Fixed Ctrl. Light	0.247		
Head Fixed Ctrl. Dark	0.065	0.315	

Running Modulated

	Head Fixed	Head Fixed Ctrl. Light	Head Fixed Ctrl. Dark
Head Fixed			
Head Fixed Ctrl. Light	0.665		
Head Fixed Ctrl. Dark	0.693	0.603	

Pupil Diameter

	Head Fixed	Head Fixed Ctrl. Light	Head Fixed Ctrl. Dark
Head Fixed			
Head Fixed Ctrl. Light	0.397		
Head Fixed Ctrl. Dark	**5.62 e -8**	**4.76 e -7**	

Table 2: P-values corresponding to Figure 3.15 A. Statistics calculated identically to Table 1**.**

Locomotion Speed

	Freely Moving	Freely Moving Ctrl. Light	Freely Moving Ctrl. Dark
Freely Moving			
Freely Moving Ctrl. Light	0.211		
Freely Moving Ctrl. Dark	0.572	0.222	

Angular Speed

	Freely Moving	Freely Moving Ctrl. Light	Freely Moving Ctrl. Dark
Freely Moving			
Freely Moving Ctrl. Light	0.070		
Freely Moving Ctrl. Dark	0.522	0.1	

Running Modulated

	Freely Moving	Freely Moving Ctrl. Light	Freely Moving Ctrl. Dark
Freely Moving			
Freely Moving Ctrl. Light	0.438		
Freely Moving Ctrl. Dark	**0.048**	0.113	

Mouse X Position

	Freely Moving	Freely Moving Ctrl. Light	Freely Moving Ctrl. Dark
Freely Moving			
Freely Moving Ctrl. Light	**0.029**		
Freely Moving Ctrl. Dark	0.274	**3.30 e -3**	

Mouse Y Position

	Freely Moving	Freely Moving Ctrl. Light	Freely Moving Ctrl. Dark
Freely Moving			
Freely Moving Ctrl. Light	0.069		
Freely Moving Ctrl. Dark	0.302	**9.09 e -3**	

continued...

Appendix B: Statistics

Head Height

	Freely Moving	Freely Moving Ctrl. Light	Freely Moving Ctrl. Dark
Freely Moving			
Freely Moving Ctrl. Light	0.067		
Freely Moving Ctrl. Dark	0.409	0.217	

Head Direction

	Freely Moving	Freely Moving Ctrl. Light	Freely Moving Ctrl. Dark
Freely Moving			
Freely Moving Ctrl. Light	**1.63 e -3**		
Freely Moving Ctrl. Dark	0.515	**6.94 e -4**	

Head Pitch

	Freely Moving	Freely Moving Ctrl. Light	Freely Moving Ctrl. Dark
Freely Moving			
Freely Moving Ctrl. Light	0.054		
Freely Moving Ctrl. Dark	0.505	0.070	

Head Yaw

	Freely Moving	Freely Moving Ctrl. Light	Freely Moving Ctrl. Dark
Freely Moving			
Freely Moving Ctrl. Light	**5.84 e -5**		
Freely Moving Ctrl. Dark	0.546	**1.43 e -5**	

Head Roll

	Freely Moving	Freely Moving Ctrl. Light	Freely Moving Ctrl. Dark
Freely Moving			
Freely Moving Ctrl. Light	**2.24 e -3**		
Freely Moving Ctrl. Dark	0.413	**3.90 e -4**	

continued...

Appendix B: Statistics

Heading	Freely Moving	Freely Moving Ctrl. Light	Freely Moving Ctrl. Dark
Freely Moving			
Freely Moving Ctrl. Light	0.147		
Freely Moving Ctrl. Dark	**0.021**	**3.68 e -4**	

Table 3: P-values corresponding to Figure 3.15 B. Statistics calculated identically to Table 1.

List of Publications

Schumacher JW, **McCann MK**, Maximov KJ, Fitzpatrick D. Selective enhancement of neural coding in V1 underlies fine-discrimination learning in tree shrew. Curr Biol. 2022 Aug 8;32(15):3245-3260.e5. doi: 10.1016/j.cub.2022.06.009. Epub 2022 Jun 28. PMID: 35767997; PMCID: PMC9378627.